Estimating the Uncertainty of Areal Precipitation using Data Assimilation

Dissertation

zur Erlangung des Doktorgrades der Naturwissenschaften
im Fachbereich Geowissenschaften
der Universität Hamburg

vorgelegt von

Claire Merker

Hamburg, 2017

Als Dissertation angenommen
vom Fachbereich Geowissenschaften der Universität Hamburg

auf Grund der Gutachten von
Prof. Dr. Felix Ament
und
Dr. Marco Clemens

Hamburg, den 20. Oktober 2017

Prof. Dr. Jürgen Böhner
Leiter des Fachbereichs Geowissenschaften

Abstract

This thesis presents a method to estimate spatially and temporally variable uncertainty of an areal precipitation product. The aim of the method is to merge measurements from different sources into a combined precipitation product and to provide an associated dynamic uncertainty estimate. Requirements for this estimate are an accurate representation of the actual uncertainty of the product, an adjustment to additional observations merged into the product through data assimilation, and flow dependency. Such detailed uncertainty description is important in order to assess the reliability of the precipitation product. It is especially important for areal precipitation information as it is needed, for example, to generate precipitation ensembles for probabilistic hydrological modelling, or to specify accurate error covariance when using precipitation observation for data assimilation into numerical weather prediction models.

The presented method uses data assimilation as a tool to merge precipitation observation. The Local Ensemble Transform Kalman Filter (LETKF) is coupled to an ensemble nowcasting model providing information about the precipitation displacement over time. A continuous nowcasting of a precipitation field and repeated assimilation of additional observations is performed. By this means, the precipitation product and its uncertainty estimate obtained from the nowcasting ensemble evolve consistently in time and become flow-dependent. An ensemble data assimilation framework is implemented and tested in order to perform a proof of concept study of the presented method. Two scores are defined to test the performance of the uncertainty estimation method. The evaluation of both considered scores demonstrates that the provided areal uncertainty estimate outperforms constant benchmark uncertainty values. It enables a more accurate spatial and temporal distribution of uncertainty, increasing the uncertainty estimate for regions where the precipitation product exhibits large errors, and decreasing it where the product has smaller errors. The proof of concept study elaborated in this thesis shows good results and establishes the groundwork for further studies and possible applications.

Zusammenfassung

Diese Arbeit stellt eine Methode zur Schätzung der räumlich und zeitlich variablen Unsicherheiten eines flächendeckenden Niederschlagsprodukts vor. Das Ziel der Methode ist es, Beobachtungen aus verschiedenen Quellen zu einem kombinierten Produkt zusammenzufügen und eine dazugehörige, dynamische Unsicherheitsschätzung zu liefern. Anforderungen an diese Schätzung sind eine präzise Darstellung der tatsächlichen Unsicherheit des Produkts, eine Anpassung an zusätzliche, durch Datenassimilation hinzugefügte Beobachtungen und Strömungsabhängigkeit. Solch eine genaue Unsicherheitsschätzung ist wichtig um die Zuverlässigkeit des Niederschlagsprodukts beurteilen zu können. Sie ist besonders wichtig für flächendeckende Niederschlagsinformation, um zum Beispiel Niederschlagsensemble für probabilistische hydrologische Modellierung zu generieren oder um präzise Fehlerkovarianzmatrizen für die Assimilation von Niederschlagsbeobachtungen in nummerische Wettervorhersagemodelle bereitzustellen.

Die vorgestellte Methode verwendet Datenassimilation als ein Werkzeug um Niederschlagsbeobachtungen zu kombinieren. Der Local Ensemble Transform Kalman Filter (LETKF) ist an ein Ensemble-Nowcasting-Modell gekoppelt welches Information über die zeitliche Verlagerung des Niederschlags liefert. Ein kontinuierliches Niederschlagsnowcasting mit wiederholter Datenassimilation zusätzlicher Beobachtungen wird durchgeführt. Dadurch entwickeln sich das Niederschlagsprodukt und dessen Unsicherheitsschätzung, die aus dem Nowcasting-Ensemble abgeleitet wird, zeitlich konsistent und werden strömungsabhängig. Um eine Machbarkeitsstudie der dargestellten Methode durchzuführen wird ein Ensemble-Datenassimilationssystem implementiert und getestet. Zwei Bewertungskennzahlen werden definiert um die Güte der Methode zur Unsicherheitsschätzung zu untersuchen. Die Auswertung beider Kennzahlen zeigt, dass die erzeugte flächendeckende Unsicherheitsschätzung besser als konstante Richtwerte für die Unsicherheit ist. Die neue Unsicherheitsschätzung erlaubt eine präzisere räumliche und zeitliche Verteilung der Unsicherheit. Die Unsicherheitsschätzung wird dort erhöht wo das Niederschlagsprodukt große Fehler aufweist, und dort verringert wo das Produkt kleinere Fehler aufweist. Die erarbeitete Machbarkeitsstudie zeigt gute Ergebnisse und schafft die Grundlage für weiterführende Studien und mögliche Anwendungen.

Contents

1 Introduction

To correctly assess the reliability of any observation, it is crucial to know the uncertainty associated with it. For precipitation observations, accurate measurements as well as a good uncertainty estimation are an ongoing topic of research. Observations from weather radars are of particular interest because they provide valuable areal precipitation information with a high spatial and temporal resolution, in contrast to in situ observations. However, radar measurements are also affected by numerous sources of errors that diminish the accuracy of the provided precipitation quantification, e.g. calibration errors, noise, interferences, clutter, and attenuation. Despite correction algorithms and filters applied to radar measurements, residual error remains inherent to the data. Additionally, the estimation of rainfall intensity from radar data implies a relation between measured reflectivity and rain rate which is empirical and uncertain. Therefore, accurate precipitation quantification is not possible with radar measurements only.

Improvement of the precipitation estimate is achieved by combining measurements from different sources, e.g. radar and rain gauge data, to take advantage of as much information as possible. Since no observation is error free, they must be weighted with their respective uncertainty in order to obtain a statistically sound combined precipitation product.

Many studies investigate the statistical combination of precipitation data. They all rely on computing the optimal estimate of precipitation by minimising its error variance. The majority of the applied techniques focus on a static, i.e. time independent, merging approach. Precipitation measurements are combined for every available time step, independently. Most merging approaches use kriging or cokriging schemes to spatially merge radar and rain gauge data (e.g. Krajewski, 1987; Creutin et al., 1988; Haberlandt, 2007; Berndt et al., 2014). Kriging methods acknowledge the fact that precipitation observations are spatially correlated by the specification of variograms. These variograms are modelled by mathematical functions based on theoretical considerations, and do not consider the temporal structure of the errors. A few observation merging methods using variational data assimilation methods can also be found. These describe the correlation between ob-

servation errors through covariance matrices. They can easily be extended to include further observations. Bianchi et al. (2013), for example, use a variational approach to estimate precipitation from radar, gauge, and microwave link data.

Furthermore, some studies additionally take into account the temporal correlation of precipitation measurements while merging radar and gauge data. The temporal structure of the errors can be considered either by modelling spatiotemporal variograms in the kriging approach (e.g. Sideris et al., 2014; Pulkkinen et al., 2016) or by using Kalman filtering that combines knowledge on error variances from previous time steps for current weighting of observations (e.g. Smith and Krajewski, 1991; Chumchean et al., 2006). The latter approach is also used by Grum et al. (2005) with the addition of microwave link data. Even though these methods consider temporal error structure in the merging process, the continuous evolution of the system is not represented.

Very few studies include a state evolution model to take advantage of previous knowledge of the system. The coupling of an evolution model can be done using Kalman filtering or variational data assimilation methods. In addition to the merging of observations, the evolution component allows for the extrapolation of information to data-void regions. Advection is commonly used as an approximation for the evolution of the system. Zinevich et al. (2009) and Mercier et al. (2015) present frameworks to estimate areal precipitation from microwave and television satellite links, respectively. Fielding et al. (2014) retrieve three-dimensional cloud properties from cloud radar and radiance observations.

The three studies presented above integrate the temporal evolution into the statistical merging of observations. The focus is on retrieving the optimal combined estimate of the system's state. However, they do not focus on an assessment of the uncertainty associated with the precipitation field. Considering radar precipitation data, this uncertainty estimation is extensively studied outside the context of combined precipitation products.

Numerous studies address the quantification of precipitation measurement uncertainty to overcome the deterministic view on radar precipitation measurements. The basis for the description of areal precipitation measurement error mostly is an empirical, statistical study of radar and reference surface measurements. Some methods only provide static information (Krajewski and Ciach, 2006), other, more recent approaches also allow for the description of the spatial and temporal structure of the errors through the description of the error covariance (e.g. Ciach et al., 2007; Germann et al., 2009; Villarini and Krajewski, 2009; Dai et al., 2014). Spatial uncertainty description allows for a probabilistic assessment of precipitation information suitable for applications. However, the resulting error description is not dynamical and flow-dependent.

Precipitation information with an accurate uncertainty estimate is highly relevant for research areas with special interest in areal precipitation information. The uncertainty information is needed for example to generate precipitation ensembles as input for probabilistic hydrological modelling (e.g. Krajewski and Ciach, 2006; Germann et al., 2009; Rico-Ramirez et al., 2015; Park et al., 2016) or nowcasting (e.g. Dai et al., 2015; Atencia and Zawadzki, 2015). Furthermore, precipitation observations are a valuable source of information for data assimilation in numerical weather prediction (e.g. Dowell et al., 2011; Chang et al., 2014; Bick et al., 2016). Recent studies stress the importance of correctly specifying errors in this context (e.g. Waller et al., 2016, 2017).

The work of this thesis connects the advantages of both aspects presented above: precipitation data merging and probabilistic assessment. It presents a method combining different precipitation observations considering their respective errors and takes advantage of the additional information provided by the evolution of the system. At the same time, the method yields an areal uncertainty estimate for the precipitation product. Because of the included temporal evolution, the uncertainty estimate is variable both in space and time and contains flow-dependency. Thus, this method aims at providing both an accurate precipitation product and an improved areal and dynamical uncertainty estimate.

The presented method uses data assimilation as a tool to merge precipitation observation. Data assimilation techniques, like the Local Ensemble Transform Kalman Filter (LETKF) used here, allow for statically combining information considering respective uncertainty within a temporal evolution (forecast) model. The LETKF additionally works in an ensemble context. The ensemble allows for providing an uncertainty assessment through the different ensemble members, i.e. yields probabilistic information. The data assimilation scheme is coupled to an ensemble nowcasting model providing information about the precipitation displacement over time. Through the continuous nowcasting of a precipitation field and repeated assimilation of additional observations, the precipitation product and its uncertainty estimates obtained from the nowcasting ensemble evolve consistently in time and become flow-dependent.

Testing the presented method required the development and implementation of an ensemble data assimilation framework (Chapter 3). This framework is implemented using object-oriented programming and is designed for flexibility in order to be easily extendable to other observations, forecast models and ensemble data assimilation schemes in the future. The ensemble nowcasting model is implemented based on a advection nowcasting scheme from van Horne (2003). The data assimilation cycle is initialised using high-resolution radar reflectivity data from a research network installed in northern Germany (Chapter 2).

The added value of the presented method is demonstrated by performing a proof

of concept study on an exemplary experiment. After confirming the functioning of the assimilation framework, the experiment results are analysed to demonstrate their validity for further study (Chapter 4). The uncertainty estimate provided with the combined precipitation product is found to improve the spatial and temporal structure of the uncertainty description compared to a benchmark (Chapter 5).

2 Precipitation Monitoring Network and Data

This thesis focuses on the study of a method providing an areal precipitation product combining multiple observation sources together with an associated uncertainty information. The presented method is demonstrated and tested using measurements from a research network installed north-west of Hamburg near the municipality of Itzehoe, Germany. It was set up for the PATTERN (Precipitation and Attenuation Estimates from a High Resolution Weather Radar Network) project in 2012 and ran until the end of 2016. Core of the network designed to monitor precipitation with high spatial and temporal resolution are four X-band weather radars and seven profiling K-band micro rain radars (MRR, METEK Meteorologische Messtechnik GmbH). Additionally, reference rain gauges are available for calibration. Figure 2.1 depicts the location of the X-band radars and MRRs installed in the network domain. The X-band radar locations are named after their installation sites: HWT (Hungriger Wolf Airport), BKM (township Bekmünde), MOD (Moordorf in the township Westermoor), QNS (township Quarnstedt). MRRs situated between LAWR sites are named WST, MST, and OST from west to east, respectively. The X-band radars have a maximum range of 20 km and the centre of the network shows a large area with multiple radar coverage. MRRs are located within the domain of high multiple coverage to have good possibilities both for calibration and data intercomparison. All in all, the network covers a domain of approximately $80\,\mathrm{km} \times 60\,\mathrm{km}$.

The following section presents the X-band radar measuring principle, sources of errors affecting the measurements and the precipitation products used as data basis in this thesis. MRRs, which are needed for the network calibration as well as for X-band radar error assessment, are also introduced. The last section of the chapter presents the statistical analysis performed to get the X-band radar measurement error needed in the course of the study for data assimilation.

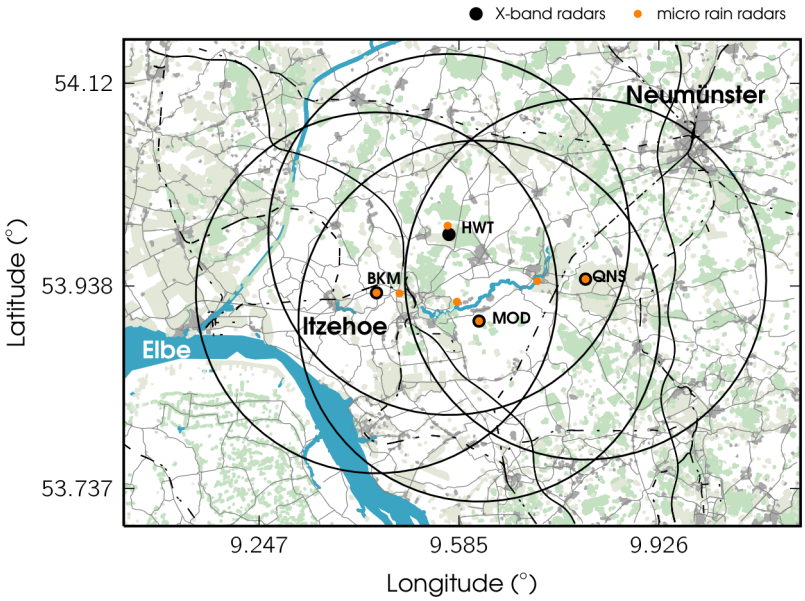

Figure 2.1: Precipitation monitoring network map. X-band radar locations and maximum range in black, MRR locations in orange. X-band radars and associated MRRs are installed at BKM, HWT, MOD and QNS sites. Three MRRs are installed between X-band radars at sites WST, MST, and OST, from west to east respectively, together with reference rain gauges.

2.1 Network Radar Data

Two radar types are used in the network outlined above: single polarisation X-band weather radars (local area weather radar, LAWR) and micro rain radars (MRR). X-band radar data constitute the basis to test the method presented in this thesis. Network composite data is needed for the precipitation nowcasting and single radar data is used for the generation of synthetic data for assimilation as well as for nowcasting verification. MRR data is considered as reference for calibration and X-band radar measurement error assessment. Although the underlying radar technique is the same, both devices have significant differences in measuring principles and scanning strategy. They operate at different wavelengths but are both designed to monitor precipitation. This section describes both instruments and available data, and shortly outlines the calibration method used within the network for data consistency.

2.1.1 X-band Weather Radar Data

The main precipitation data used in this study comes from weather radar measurements. The great advantage of weather radars is the areal precipitation information provided with good spatial and temporal resolution. Weather radars scan the at-

mosphere on a conical surface with defined elevation angle. Typically, radars in large national networks provide measurements every five minutes with 1° azimuthal sampling and 1 km range resolution. Newer devices can resolve precipitation with 250 m range resolution (see for example the C-band radar network of the German Meteorological Service, DWD). The X-band radars presented here (LAWR) deliver valuable high resolution data, with 1° and 60 m spatial resolution and measurements available every 30 seconds. Unlike most radar devices used nowadays, they provide reflectivity measurements without dual-polarisation and Doppler information. LAWRs were built for research purpose in a cooperation between the meteorological department of the University of Hamburg and the Max Planck Institute for Meteorology (MPI-M).

The LAWRs are built on the basis of simple ship navigation radars originally manufactured by the company GEM elettronica. The main modification is the replacement of the original slot antenna with a parabolic antenna, as seen in Figure 2.2. LAWRs operate at 9.41 GHz, i.e. within X-band frequency range, and scan the atmosphere with 800 pulses per seconds while rotating continuously. Pulses are then sampled over 1° segments and allocated to 333 range bins of 60 m length each, defining a total of 119 880 pixels per 30 second measurement time step. Technical LAWR specifications are gathered in Table 2.1. Within the network, LAWRs are installed on masts at 14 m (BKM, MOD, QNS) and 20 m (HWT) height in order to surpass surrounding trees and buildings. Their elevation is constant and set to 2°, resulting in a maximum height above ground of approx. 1000 m at final range. The measurements are mapped to the ground using a 4/3 Earth radius approximation to account for beam bending due to atmospheric refraction. LAWR measuring principle follows basic radar theory as outlined below.

Two essential quantities are needed to monitor precipitation (or any target) with a radar: the received power to compute reflectivity and the time elapsed between sending and receiving signal for range allocation. The transmitted power P_t (in W) is partly backscattered by targets in the atmosphere. The power $P_\mathrm{r}(r)$ received from a distance r (in m) is measured and related to the distance dependent radar reflectivity η (in $\mathrm{mm^2 m^{-3}}$) according to the radar range equation (e.g. Probert-Jones, 1962; Raghavan, 2003; Rinehart, 2010):

$$P_\mathrm{r}(r) = \frac{P_\mathrm{t} G^2 \theta^2 l \lambda^2}{1024 \ln(2) \pi^2 r^2} \eta(r). \tag{2.1}$$

The relation between received and transmitted power depends on device constants like the radar wavelength λ (in m), the beam width θ (in radians), and the antenna gain G. The antenna gain quantifies the efficiency of the antenna in focusing emitted power into the radar beam and the sensitivity to the direction of returning signal. The received power $P_\mathrm{r}(r)$ also depends on the pulse length l (in m) which is the distance travelled by the emitted signal during the pulse width (in m). The radar

Figure 2.2: LAWR device without radome (left) showing the parabolic antenna and as installed at QNS site (right). It is mounted on a 11 m mast fixed on a 3 m high container.

reflectivity η is defined as the sum of single backscattering cross sections σ (in mm^2) of all targets in a unit volume:

$$\eta = \sum_{vol} \sigma_i. \tag{2.2}$$

Under the assumption of spherical targets with small diameter compared to the wavelength (commonly about 1/10) the Rayleigh approximation dictates a simple relation between backscattering cross section and drop diameter D (in mm):

$$\sigma = \frac{\pi^5 |K|^2 D^6}{\lambda^4}.$$

The dielectric factor $|K|^2$ is a natural constant, $|K|^2 = 0.92\,\mathrm{m}^{-1}$ for water. Therefore, a new reflectivity parameter proportional to η can be introduced under Rayleigh approximation. The radar reflectivity factor Z (in $\mathrm{mm}^6\mathrm{m}^{-3}$) is defined as the sum of drop diameters in a unit volume:

$$Z = \sum_{vol} D_i^6.$$

Unlike the radar reflectivity η, the radar reflectivity factor Z is independent of radar wavelength. This is a great advantage because it enables the comparison between reflectivity measurements from different devices. Using the Rayleigh approximation and inserting the radar reflectivity factor into (2.1) yield another form of the radar equation which allows for computing $Z(r)$ from the received power signal:

$$P_\mathrm{r}(r) = \frac{P_\mathrm{r} G^2 \theta^2 l \pi^3 |K|^2}{1024 \ln(2) \lambda^2 r^2} \cdot Z(r). \tag{2.3}$$

Table 2.1: Technical LAWR specifications.

Azimuthal sampling resolution	1°
Range resolution	60 m
Time resolution	30 s
Maximum range along beam	20 km
Elevation	2°
Frequency (Wavelength)	9.41 GHz (3.2 cm)
Beam width	2.8°
Transmit power	25 kW
Pulse width	0.4 µs
Pulse repetition rate	800 Hz
Antenna diameter	850 mm
Rotation	24 revs/min

To be precise, the received power $P_\mathrm{r}(r)$ in the radar equation is always an averaged value over multiple pulses. Single pulse values underlie large variance because of the great variability of drops within precipitation and averaging guarantees stable received power. LAWRs average pulses over the azimuthal sampling resolution as well as over multiple rotations since the radar constantly rotates during the 30 seconds measurement interval. This results in approximately 65 pulses averaged per issued value.

As stated above, (2.3) is only valid when the Rayleigh approximation holds. If this is not the case, the radar reflectivity factor must be expressed by a slightly different term: the equivalent reflectivity factor Z_e, which again depends on the radar wavelength and accounts for scattering targets that do not follow the Rayleigh approximation. For LAWRs used in this thesis, the Rayleigh approximation is a valid assumption and radar reflectivity factor Z will be used throughout. For simplicity, Z will be called reflectivity from here. In addition, Z will be given in its logarithmic form $\mathrm{dB}Z = 10\log_{10}(Z)$, essentially to get a value distribution close to a Gaussian one.

Practically, radar reflectivity obtained from (2.3) is never intrinsic reflectivity because the signal is altered along the path. There are numerous causes of errors affecting radar measurements. Principle sources of spurious signals are listed below, along with a short indication of data processing methods used on LAWR data for this thesis. Refer to Lengfeld et al. (2014) for more details about data processing as well as additional information on the LAWR network within the framework of the PATTERN project.

Noise: Noise is an unavoidable artefact created by compounds within the radar's electronic. It is superimposed to measurements and especially masks weak signal at far range. The received power $P_\mathrm{r}(r)$ by definition decreases with r^2, as apparent in (2.3). In contrast, noise created within the radar itself affects

measurements at all ranges with constant intensity. Therefore, noise shows a characteristic increase with distance in Z values, which are corrected with regard to r^2. The LAWR noise filter detects the noise level by computing the 10th percentile of reflectivity values in fields with at least 10 % precipitation free areas. The noise level is subtracted from the reflectivity data for subsequent data analysis.

Attenuation: The radar signal loses power by travailing through any medium. In the case of weather radars, the signal attenuating mediums to consider are air and water. Attenuation by air (mostly oxygen and water vapour) is small at X-band frequency range and dampens reflectivity by about 0.1 dB at the maximum range of 20 km (Rinehart, 2010, p. 153). It is therefore neglected. Attenuation by water is much higher, especially at X-band frequency. For example, measurements at 20 km from the radar would be dampened by about 6.5 dB by a constant precipitation field of 10 mm h^{-1}, or roughly 40 dBZ (Doviak and Zrnić, 2014, p. 42). Attenuation by rain at X-band frequency can be strong enough to fully suppress precipitation signal behind strong cells. In this case it is not possible to correct for the attenuation effect because all signal is lost. Lower attenuation can be corrected using theoretical knowledge on the relation between precipitation intensity and attenuation. LAWR data is corrected using a scheme based on Hitschfeld and Bordan (1954). Reflectivity values are iterated along the beam path and increased by a theoretically computed attenuation value. This approach tends to be conservative and does not fully account for attenuation intensity.

Static clutter: The term clutter is used in radar meteorology to describe non-meteorological echoes, usually characterised by high signal intensity. Static clutter describes constant echoes in the data. These echoes are due to fix obstacles like trees or buildings and are usually most frequent in the near field, where the beam is low. Pixels showing reflectivity values above 7 dBZ over 95 % of the time are identified as static clutter and removed.

Dynamic clutter: Radar data is usually affected by a number of non-static, erroneous signals. Those signals can originate for example from birds, insects, or signal interferences at similar wavelengths. Two detection algorithms are used here to eliminate areas with strong inhomogeneity in adjacent pixels. The TDBZ (Texture of the dBZ field) filter makes use of the reflectivity field texture and computes the mean squared reflectivity differences between pixels in a defined area. The SPIN filter counts the number of changes in the sign of reflectivity gradients. Both filters are presented in Hubbert et al. (2009). In addition, reflectivity measurements are tested for temporal consistency, making use of the high temporal resolution of LAWRs. At a resolution of 30 s, precipitation signal location is assumed to be stationary in consecutive time

steps. If a signal is present in one time step but not in the two preceding time steps, it is identified as clutter. All dynamic clutter is removed from the data.

Spike and ring clutter: Interferences by other X-band emitting devices (for example from radars on ships or in the harbour along Elbe river) cause erroneous high intensity signals in LAWR data. These signals often have the shape of spikes in narrow azimuthal ranges or ring segments along few radial bins. Spikes and rings belong to the dynamic clutter because they are variable in time and space. But they often remain undetected by dynamic clutter filter since they affect larger areas of adjacent pixels and have uniform values. Spikes and rings are identified in the data by opposed gradients in reflectivity along azimuth or range gates stretching over at least five bins.

Miscalibration: LAWRs need to be calibrated using reference measurements. In the network environment available for this study, reference measurements are provided by MRRs. They are introduced in Section 2.1.2 and the calibration procedure for both instruments is described thereafter in Section 2.1.3.

Note that most state of the art radar post-processing algorithms used to remove clutter are based on polarimetric or Doppler quantities. They generally perform better than filters relying only on simple reflectivity fields, but cannot be implemented for LAWR data due to missing polarimetric and Doppler information.

Two radar reflectivity products are available from the LAWR network: single radar reflectivity fields and composite reflectivity fields. Single radar reflectivity is provided on polar coordinates (360 azimuth and 333 range gates) and every 30 seconds for each of the four considered LAWRs, separately. The composite product is a merged reflectivity field combining measurements from all four network LAWRs. It is computed on a quasi Cartesian coordinate system with approximately $250\,\mathrm{m} \times 250\,\mathrm{m}$ resolution, resulting in a field with 297×213 pixels. The projection used to compute the common grid is a rotated coordinate system that shifts the Earth equator to the middle of the LAWR network in order to get nearly orthogonal meridians and parallels. The position of the North Pole in rotated coordinates is set to 36.0625 °E, 170.415 °S. LAWR measurements are allocated to pixels of the regular grid and overlapping reflectivity values are averaged to get the composite reflectivity field. In the remainder of this thesis, data is depicted in the rotated coordinate system for simplicity, since only relative locations are of interest. Reflectivity data in single and composite products is thresholded to $5\,\mathrm{dB}Z$, approximately $0.07\,\mathrm{mm\,h^{-1}}$. This is especially important when using the X-band radar data for data assimilation. Values referring to no-precipitation signal reach down to approximately $-30\,\mathrm{dB}Z$ in weather radar measurements. This can yield large reflectivity difference between model forecast value and observations even though both indicate no precipitation. To avoid this effect, a threshold below which reflectivity values are not considered to be caused by precipitation is defined and applied. The threshold

value used here is common and also used in e.g. Aksoy et al. (2009); Bick et al. (2016).

Figure 2.3 demonstrates the different LAWR single data processing levels using the X-band radar MOD. The 17$^{\text{th}}$ August 2013 at 04:00:00 UTC is chosen exemplary. Figure 2.3a is the raw reflectivity field before noise and clutter removal and attenuation correction. The whole area captured by the radar is covered by reflectivity signal. Values do not fall below 15 dBZ, which is due to the superimposition of noise still present in the data. Nevertheless, precipitation structure is discernible because the precipitation signal is above noise level. In Figure 2.3b, after noise removal, overall reflectivity intensity is lower. Some areas of the field dropped below the defined no-precipitation threshold. Pixels marked in orange have been detected as clutter and values removed. These pixels are interpolated in the next processing step before attenuation correction is applied. Final data is shown in Figure 2.3c. Attenuation is highest in regions with stronger precipitation, along the axis of the precipitating band, where an increase in reflectivity compared to Figure 2.3b is visible. Measurements of all four LAWR merged onto the regular grid is presented in Figure 2.4, for the same time step as above. The composite product makes use of the network advantages and provides reflectivity on an area larger than a single radar. The precipitation structure apparent in Figure 2.3 is still present and extended by measurements of the additional three X-band radars.

2.1.2 Micro Rain Radar Data

The micro rain radar (MRR) is a reflectivity profiler manufactured by METEK Meteorologische Messtechnik GmbH. It retrieves drop size distribution (DSD), and consequently reflectivity (Z) and rain rate (R), for multiple height levels. As opposed to other precipitation monitoring instruments like rain gauges, the MRR provides data directly at X-band radar beam height. Collocated radar measurements reduce the discrepancy caused by measurement distance and point-to-area problems. Furthermore, the MRR yields reflectivity as well as rain rate values directly. No conversion between rain rate and reflectivity, which is a substantial uncertainty source when comparing rain gauge and radar data, is necessary. Therefore, MRR data is suitable for comparison with radar data in beam height as well as rain gauge data at the surface. This study makes use of MRR data as a connection between gauge and radar data to calibrate the X-band radar network. In addition, MRRs are used as a reference to compute X-band measurement errors in Section 2.2. In total, seven MRRs are installed within the radar network depicted in Figure 2.1. Figure 2.5 shows a MRR and its installation at QNS site as an example.

The MRR is a frequency-modulated continuous wave (FM-CW) radar with parabolic antenna emitting at a base frequency of 24.23 GHz and with a fix vertical beam

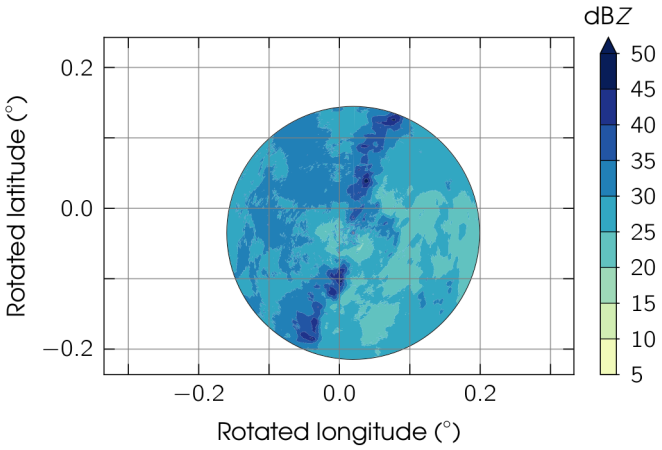

(a) Raw data

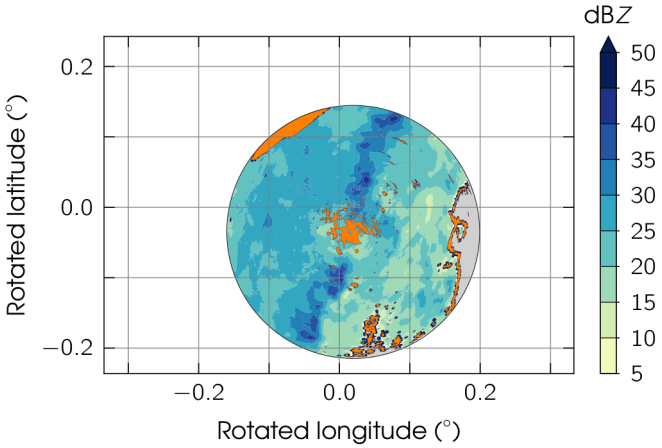

(b) After noise and clutter removal

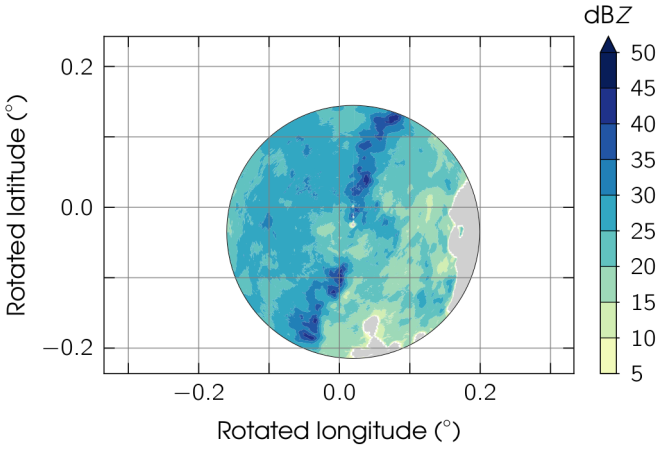

(c) Interpolated and attenuation corrected

Figure 2.3: Polar data from X-band radar MOD in three different processing steps, at 04:00:00 UTC on the 17$^{\text{th}}$ August 2013. **(a)** is the raw reflectivity data, **(b)** the data after noise and clutter removal (clutter pixels in orange) and **(c)** the final single radar data product, after interpolation and attenuation correction.

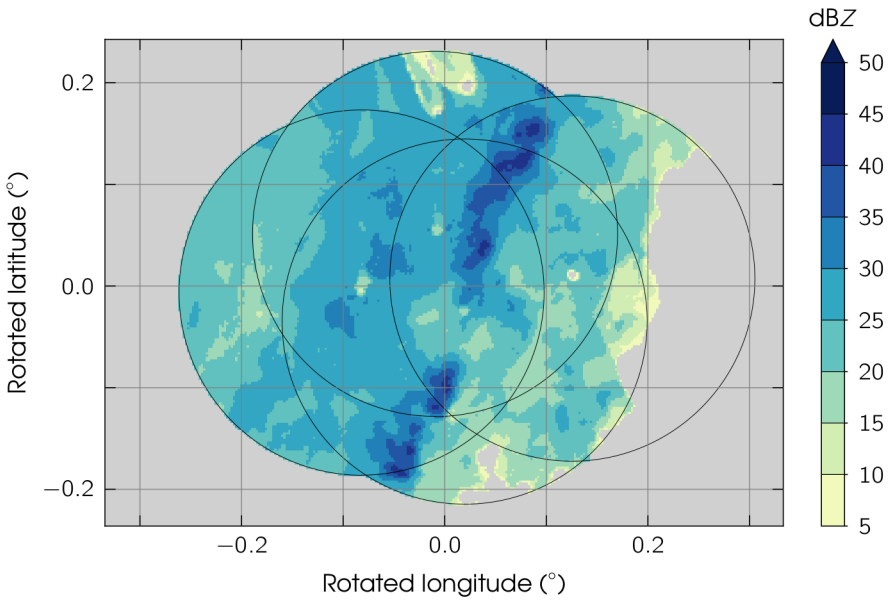

Figure 2.4: Composite LAWR reflectivity data merging reflectivity values from BKM, HWT, MOD, and QNS radars on a regular grid with 250 m × 250 m resolution, at 04:00:00 UTC on the 17$^{\text{th}}$ August 2013. Pixels outside network reach or below the no-precipitation threshold of 5 dBZ are displayed in grey.

orientation. The MRR enables to resolve spectral radar reflectivity for 64 drop diameter classes using the Doppler effect in the frequency shift between transmitted and received signal. It has a high temporal resolution of 10 seconds and a range resolution of 35 m along 31 height levels. Further technical details are listed in Table 2.2. Spectral data is not relevant for this thesis, which only makes use of total reflectivity integrated over all drop diameters. But since the MRR operates at a frequency at which Rayleigh approximation is no longer valid, spectral reflectivity and resulting DSD are needed to calculate the radar reflectivity factor Z allowing for comparison with LAWR data. Therefore, MRR measuring principle and spectral quantities are shortly outlined in the following. More details are given in the user's manual METEK GmbH (2009).

The frequency shift Δf_{total} recorded by the MRR is a superposition of the Doppler shift $\Delta f_{\text{Doppler}}$ caused by moving drops and the shift Δf_{height} originating from the modulated transmitted signal. In the simple case of drops with same terminal velocity v_t (in m s^{-1}) and same height h (in m), Δf_{total} can be expressed as:

$$\Delta f_{\text{total}} = \underbrace{\frac{2}{\lambda} v_t}_{\Delta f_{\text{Doppler}}} + \underbrace{B \frac{2h}{cT}}_{\Delta f_{\text{height}}} . \tag{2.4}$$

The frequency shift Δf_{height} directly relates to drop height and enables height level allocation. The bandwidth B, i.e. the amplitude, of the transmitted signal around

Figure 2.5: MRR device from METEK showing the parabolic antenna for vertical orientation of the beam (left) and an installation at QNS site (right). It is mounted on a 3 m high container.

Table 2.2: Technical MRR specifications (valid for the data set used in this thesis).

Time resolution	10 s
Range resolution	35 m
Maximum height	1085 m
Number of height levels	31
Number of Doppler spectrum lines	64
Orientation	vertical
Base frequency (Wavelength)	24.23 GHz (1.24 cm)
Bandwidth	1.55 MHz
Sampling rate	125 kHz
Beam width	1.5°
Antenna diameter	600 mm

the base frequency f_0 defines the range resolution of the measurements because it sets a maximum captured target height. During one frequency sweep, the signal starts at $f_0 + B/2$ and decreases linearly towards $f_0 - B/2$, as shown schematically in Figure 2.6. Due to this modulation and the resulting frequency shift between transmitted and received signal, it is possible to obtain the distance travelled by the signal. The frequency shift $\Delta f_{\text{Doppler}}$ is caused by the vertical movement of drops relative to the MRR. Drops backscatter the received signal with a frequency shift proportional to their terminal fall velocity. Discrimination of both frequency shifts and allocation of reflectivity to height and terminal velocity of drops is done through Fourier analysis of the received signal. Spectral reflectivity $\eta(n, i)$ (in mm^2m^{-3}), associated to velocity level n and height level i, can be calculated from the spectral power density obtained from the Fourier analysis using a form of the radar equation valid for the MRR (METEK GmbH, 2009, p. 11). Spectral reflectivity $\eta(n, i)$ can be converted to $\eta(D, i)$ (in mm^1m^{-3}) using empirical knowledge about the relation between drop diameter D (in mm) and terminal velocity. Spectral DSD $N(D, i)$ (in $\text{mm}^{-1}\text{m}^{-3}$) can then be computed by dividing the reflectivity received in one drop size class $\eta(D, i)$ by the single particle backscattering cross section of that drop size

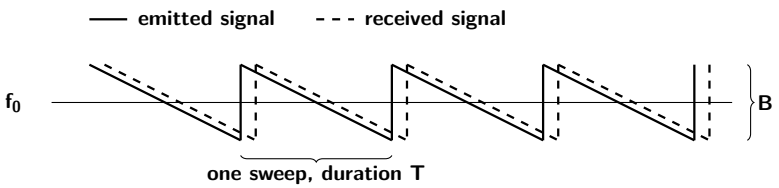

Figure 2.6: Schematic MRR signal modulation of bandwidth B around base frequency f_0. Each sweep has the duration T. Emitted signal is solid, received signal backscattered from an immovable target at height h is dashed. Frequency shift Δf_{height} between both signals is caused by target height.

class $\sigma(D)$ (in mm^2):

$$N(D,i) = \frac{\eta(D,i)}{\sigma(D)}.$$

$N(D,i)$ gives the number of drops in each resolved diameter class D and height level i. From this DSD information, rain rate $R(i)$ and $Z(i)$ for each height level can be computed according to

$$\begin{aligned} Z(i) &= \int_D N(D,i) D^6 dD, \\ R(i) &= \frac{\pi}{6} \int_D N(D,i) D^3 v_t(D,i) dD, \end{aligned} \tag{2.5}$$

with $Z(i)$ in mm^6m^{-3} and $R(i)$ in $\text{mm}\,\text{h}^{-1}$.

In this thesis MRR data is thresholded to 5 dBZ, as introduced for LAWR data in Section 2.1.1. Figure 2.7 shows a time series of MRR reflectivity profiles at the HWT site. It presents the same precipitation event as in Figure 2.3 and 2.4 and shows measurements between 03:00:00 UTC and 05:00:00 UTC. The two lowest height levels are ignored because of data quality issues in the MRR near field. The advantage of high-resolution profile data is apparent in the visible small-scale variability of precipitation, e.g. single fall streaks. The reflectivity shows an intensification around 03:40:00 UTC. Precipitation stops around 04:50:00 where reflectivity drops below the no-precipitation threshold of 5 dBZ.

2.1.3 Radar Data Calibration

Precipitation data from LAWRs and MRRs need to be calibrated for consistency within the network and accuracy of measurements. The calibration procedure makes use of the measuring properties of MRRs that allow for retrieving reflectivity Z as well as rain rate R without an empirical Z–R relationship (see (2.5)). In addition, it exploits the fact that MRR data can be compared to rain gauge and X-band radar data at similar height due to the profile information. The presented calibration is

performed on network data for the period between April and October 2013, using three-hour averages of the data.

The main steps of the network calibration are shown in Figure 2.8. Within the research network presented in Figure 2.1, MRRs at WST, MST and OST sites are installed in combination with reference rain gauges (G). Those MRRs are calibrated by comparing the third height level of the MRR rain rate R_{MRR} to the rain gauge rain rate R_{G} (Figure 2.8, step 1). The calibration coefficient is computed as the mean difference of logarithmic rain rates for all available data pairs

$$C_{\mathrm{MRR,dB}} = \frac{1}{N}\sum_{N}(\mathrm{dB}R_{\mathrm{MRR}} - \mathrm{dB}R_{\mathrm{G}}),$$

with $\mathrm{dB}R = 10\log_{10}(R)$. Rain gauge rain rates R_{G} are previously corrected according to Rubel and Hantel (1999) to compensate for wind-induced losses in rain intensity. The calibration constant $C_{\mathrm{MRR,dB}}$ is additive for logarithmic $\mathrm{dB}R$. In order to apply it to linear R or Z values, it has to be converted to $C_{\mathrm{MRR}} = 10^{0.1 \cdot C_{\mathrm{MRR,dB}}}$. R and Z take the same calibration coefficient since both are directly proportional to DSD, which is the actually calibrated quantity (see (2.5)). Knowing C_{MRR}, reflectivity profiles of MRRs at WST, MST, and OST can be corrected and are then used to compare to LAWR reflectivity. This comparison is done at LAWR beam height, using the range gate corresponding to the MRR location (Figure 2.8, step 2). MRR height levels are averaged over the vertical extent of the LAWR beam using linear weighting depending on distance to the LAWR beam centre, since LAWR measurements are most sensitive to the signal in the centre of the beam. Up to 25 MRR height levels are considered depending on the network site and the distance between both devices since beam width increases with range. The LAWR calibration constant is determined as follows

$$C_{\mathrm{LAWR,dB}} = \frac{1}{N}\sum_{N}(\mathrm{dB}Z_{\mathrm{LAWR}} - \mathrm{dB}Z_{\mathrm{MRR}}),$$
$$C_{\mathrm{LAWR}} = 10^{0.1 \cdot C_{\mathrm{LAWR,dB}}},$$

where $C_{\mathrm{LAWR,dB}}$ is the mean logarithmic reflectivity deviation considering the whole calibration period and all reference MRRs within LAWR reach. The last network calibration step is the calibration of remaining MRRs at BKM, HWT, MOD, and QNS sites (Figure 2.8, step 3). These MRRs have to be calibrated using LAWR data because no reference rain gauges are available at those sites. This calibration step is performed in analogy with LAWR calibration described above. Further information on this network calibration procedure and results for the time period investigated here are presented in Lengfeld et al. (2014).

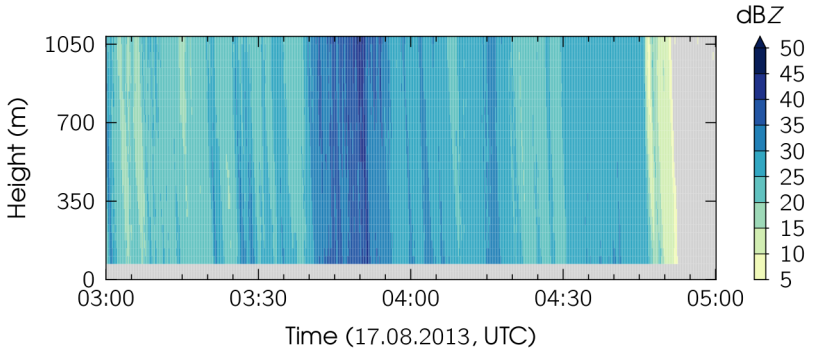

Figure 2.7: Time series of MRR reflectivity factor profiles at HWT site between 03:00:00 UTC and 05:00:00 UTC on the 17$^{\text{th}}$ August 2013. No-precipitation threshold is 5 dBZ.

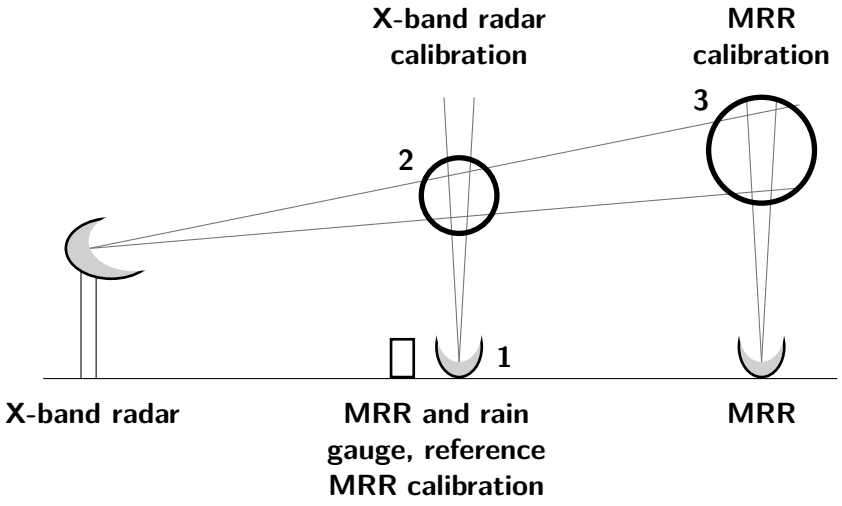

Figure 2.8: Schematic illustration of the network calibration procedure for X-band radar and MRR calibration. Reference MRRs are calibrated using rain gauges (step 1), X-band radars are calibrated using calibrated reference MRRs (step 2) and remaining MRRs are calibrated by comparison with previously calibrated X-band radars (step 3).

2.2 Network Specific Radar Error Statistics

Network radar data is used to assess the X-band radar measurement error. This error information, more precisely information about the random part of the error, is crucial to be able to use the measurements for data assimilation in this study. Radar measurements are affected by numerous sources of errors, as listed in Section 2.1.1. Some errors, like attenuation or calibration errors, are systematic and can be corrected using mentioned methods. Clutter and interferences appear randomly and can only be detected with filters and removed. Nevertheless, it is not possible to perfectly correct radar data. Especially random error, e.g. remaining noise, is

always present in the data. MRR reflectivity data is used as reference to assess the X-band radar measurement uncertainty specific to the network presented in Section 2.1. MRR reflectivity data at X-band radar beam height is used for comparison of collocated measurements. As for the calibration procedure in Section 2.1.3, MRR data is averaged over height levels falling within the X-band radar beam width. Additionally, MRR data, which has a temporal resolution of 10 seconds, is averaged to match the 30 seconds time step of the X-band radar data.

X-band measurement errors are computed as the difference between X-band reflectivity and MRR reflectivity, both in dBZ and for each available 30 seconds time step. Within the network depicted in Figure 2.1, four X-band radars and seven MRRs are available to analyse X-band measurement errors. Due to the different possible combinations between devices, X-band measurement errors at different distances from the radar centre, different beam heights and different devices are taken into account. In order to avoid using data in the X-band radar near range, which is prone to large measurement uncertainty and hence affected by data filtering, LAWR-MRR pairs at the same site are excluded from the analysis. Some LAWR-MRR pairs have to be excluded because the MRR site is not within reach of the LAWR measurement. Table 2.3 shows the 20 valid LAWR-MRR pairs. The time period analysed for the measurement error assessment goes from 1$^{\text{st}}$ May to 30$^{\text{th}}$ September 2013. This summer period is chosen to avoid the occurrence of snow, which falsify measurements. Figure 2.9 gives an overview of daily precipitation sums during this period. Especially May, June and September had frequent rainfall, which lead to a large available data set. Comparison between X-band and MRR measurements is only performed on data points where both devices recorded at least 5 dBZ. Considering all valid LAWR-MRR combinations and all valid data pairs, the data set comprises 440 324 data points and is therefore appropriate for statistical study.

A bias between X-band radar and MRR measurements can be computed from the data set described above. It shows that X-band radar reflectivity is in average 0.50 dB higher than MRR reflectivity. This bias is most probably due to remaining miscalibration or noise level. In order to use X-band radar data for data assimilation, the random part of the error must be defined. The standard deviation of the X-band measurement errors is computed and amouts to 3.36 dB, i.e. a variance of 11.32 dB^2. This variance is used in this study to specify the uncertainty of X-band radar measurements for data assimilation.

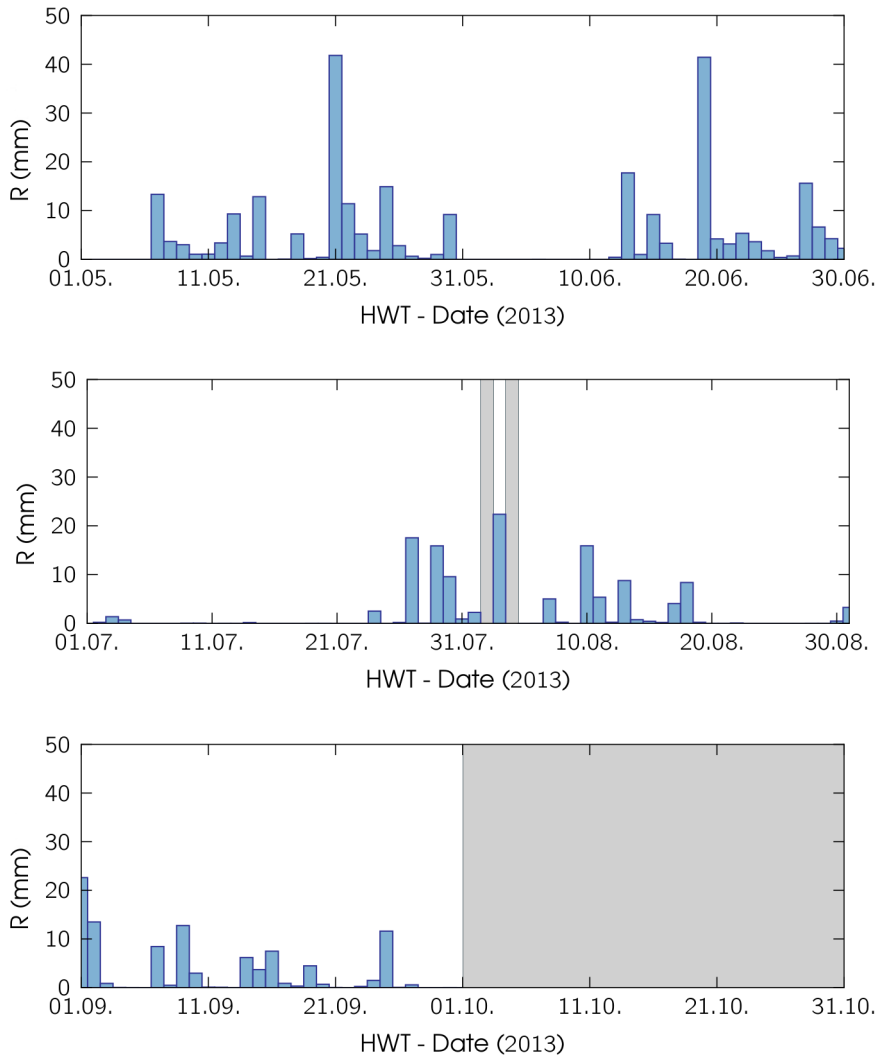

Figure 2.9: Daily precipitation sums obtained from the MRR at HWT site between May and September 2013. Missing days are greyed out.

Table 2.3: Possible LAWR-MRR combinations for data comparison.

		MRR						
		BKM	HWT	MOD	MST	OST	QNS	WST
LAWR	BKM		✓	✓	✓	✓		
	HWT	✓		✓	✓	✓	✓	✓
	MOD	✓	✓		✓	✓	✓	✓
	QNS		✓	✓	✓	✓		

3 Framework for Ensemble Data Assimilation in Precipitation Nowcasting

A data assimilation framework coupling a simple probabilistic radar nowcasting scheme to precipitation measurements is needed to investigate the topic of this thesis. Since such a framework, satisfying the requirements of the study, was not available at the beginning of the work, the framework was built up during the work of this thesis. It consists of an ensemble data assimilation core part to which forecast models, e.g. nowcasting, can be coupled. The data assimilation system is implemented in collaboration with Dr. Gernot Geppert. The framework is written in Python and principal components are implemented using object-oriented programming. Therefore, it is flexible and easily expandable. It is designed to allow the coupling to various forecast models and observation types, and the implementation of different ensemble data assimilation methods. This chapter first gives a complete derivation of the Local Ensemble Transform Kalman Filter data assimilation method chosen for the study. It then presents the used ensemble nowcasting scheme, which is a strongly adapted version of a precipitation extrapolator described in the work of van Horne (2003). The last part of the chapter addresses the design and implementation of the data assimilation framework.

3.1 The Local Ensemble Transform Kalman Filter for Data Assimilation

Data assimilation is used in this thesis as a tool to statistically merge precipitation data from different sources. Data assimilation aims at combining different sources of information about an observed system, weighted by their respective uncertainty, in order to get the best possible estimate of the system's true state. The main application of data assimilation in atmospheric sciences is in numerical weather prediction, where data assimilation is used to estimate the initial state for a forecast. This initial state is approximated in the best possible way by combining the last

available forecast of the atmospheric state with a large amount of observational data. In the case of this thesis, the system to be described is areal precipitation, the forecast model used to predict areal precipitation is the ensemble nowcasting scheme introduced in Section 3.2, and the observations are radar measurements presented in Section 2.1.

There are a number of different data assimilation schemes, grouped into three main categories: variational methods, Kalman filters, and particles filters. An overview of these methods can be found in, e.g. following works: Lorenc (1986) for variational methods, Kalnay et al. (2007) for variational methods and Kalman filters, Arulampalam et al. (2002) and Vetra-Carvalho et al. (2017) for Kalman filters and particle filters, and Tippett et al. (2003) and Houtekamer and Zhang (2016) for Kalman filters. As mentioned above, the forecast model used in this thesis provides an ensemble forecast and therefore requires an ensemble data assimilation scheme. The data assimilation method used in this thesis is the Local Ensemble Transform Kalman Filter (LETKF), first introduced by Hunt et al. (2007). It allows to work with an ensemble of moderate size through a localisation approach. This section provides a self-contained derivation of the LETKF, building on the introduction of the Kalman Filter (KF) equations as a solution to a linear least-squares estimation problem. Since the KF is not suitable for application in non-linear systems the ensemble component is introduced, leading to the Ensemble Kalman Filter (EnKF) and specifically to the Ensemble Transform Kalman Filter (ETKF). Finally, domain localisation is included, yielding the LETKF. Used equations in their final form can be found in (3.17).

3.1.1 The Kalman Filter

The Kalman Filter (KF, Kalman (1960); Kalman and Bucy (1961)) is used to find the best estimate of the true state $\boldsymbol{x^t}$ of a system based on all available information $\boldsymbol{z}$. The best, or optimal estimate is called the analysis $\boldsymbol{x^a}$. Talagrand (1997) provides a derivation of the expression for $\boldsymbol{x^a}$ using the Best Linear Unbiased Estimator (BLUE), which is presented in the following.

First, we define $\boldsymbol{x^t}$ and $\boldsymbol{x^a}$ as one-dimensional column vectors containing the whole model state. This means all model variables at every model location are reshaped and appended to one another. By analogy, $\boldsymbol{z}$ gathers all available information into a one-dimensional column vector, defined as

$$\boldsymbol{z} = \boldsymbol{\Gamma x^t} + \boldsymbol{\xi}, \tag{3.1}$$

where $\boldsymbol{\Gamma}$ is a matrix relating true state space to information space and $\boldsymbol{\xi}$ is the information error. The information error $\boldsymbol{\xi}$ is assumed to be unbiased, i.e. the expected value of $\boldsymbol{\xi}$ is $\mathbb{E}[\boldsymbol{\xi}] = 0$, and has covariance $\boldsymbol{\Sigma}$. By definition, the analysis $\boldsymbol{x^a}$ is found

as a linear combination of all information in $\boldsymbol{z}$, which can be written as

$$\boldsymbol{x^a} = \boldsymbol{\Omega z}. \tag{3.2}$$

The matrix $\boldsymbol{\Omega}$ represents the weights attributed to the different information contained in $\boldsymbol{z}$ and maps the dimension of $\boldsymbol{z}$ to the dimension of $\boldsymbol{x^a}$. The information weighting is dependent on its statistical certainty, described by the error covariance $\boldsymbol{\Sigma}$. The weights $\boldsymbol{\Omega}$ must be determined in order to obtain the optimal estimate $\boldsymbol{x^a}$. To be able to do so, $\boldsymbol{x^a}$ is required to be statistically unbiased with regard to the true state $\boldsymbol{x^t}$, i.e. $\mathbb{E}[\boldsymbol{x^a}] \stackrel{!}{=} \boldsymbol{x^t}$. From this we can derive the following constraint

$$\begin{aligned} 0 &= \mathbb{E}[\boldsymbol{x^a}] - \boldsymbol{x^t} = \mathbb{E}[\boldsymbol{\Omega\Gamma x^t} + \boldsymbol{\Omega\xi}] - \boldsymbol{x^t} \\ &= \boldsymbol{\Omega\Gamma x^t} + \boldsymbol{\Omega}\underbrace{\mathbb{E}[\boldsymbol{\xi}]}_{=0} - \boldsymbol{x^t} \\ &= [\boldsymbol{\Omega\Gamma} - \boldsymbol{I}] \cdot \boldsymbol{x^t} \\ \Rightarrow \boldsymbol{\Omega\Gamma} &= \boldsymbol{I}, \end{aligned} \tag{3.3}$$

where $\boldsymbol{I}$ is the identity matrix. The BLUE defines the optimal estimate of the true state as the estimate with minimum error covariance. It therefore needs an analytic expression for the error covariance of $\boldsymbol{x^a}$, such that the covariance can be minimised in a next step. The error covariance matrix $\boldsymbol{P^a}$ of the analysis $\boldsymbol{x^a}$ is given by

$$\begin{aligned} \boldsymbol{P^a} &= \mathbb{E}[(\boldsymbol{x^a} - \boldsymbol{x^t})(\boldsymbol{x^a} - \boldsymbol{x^t})^T] \\ &= \mathrm{cov}(\boldsymbol{x^a} - \boldsymbol{x^t}) \\ &= \mathrm{cov}(\boldsymbol{\Omega z} - \boldsymbol{x^t}) \\ &= \mathrm{cov}(\boldsymbol{\Omega\Gamma x^t} + \boldsymbol{\Omega\xi} - \boldsymbol{x^t}) \\ &= \mathrm{cov}([\boldsymbol{\Omega\Gamma} - \boldsymbol{I}]\boldsymbol{x^t}) + \mathrm{cov}(\boldsymbol{\Omega\xi}) = \mathrm{cov}(\boldsymbol{\Omega\xi}). \end{aligned}$$

Using $\mathrm{cov}(\boldsymbol{Ax}) = \boldsymbol{A}\mathrm{cov}(\boldsymbol{x})\boldsymbol{A}^T$ and the constraint developed in (3.3), the analysis error covariance $\boldsymbol{P^a}$ can be written as

$$\boldsymbol{P^a} = \boldsymbol{\Omega\Sigma\Omega}^T, \tag{3.4}$$

where $\boldsymbol{\Sigma}$ denotes $\mathrm{cov}(\boldsymbol{\xi})$. Now, minimising the variance of the analysis error is equivalent to minimising the trace $\mathrm{tr}(\boldsymbol{P^a})$ of $\boldsymbol{P^a}$, since the trace is defined as the sum of elements on the main diagonal of a matrix. The method of Lagrange multipliers is used to find local extremes of $\mathrm{tr}(\boldsymbol{P^a})$, subject to the constraint in (3.3). For (3.4), the Lagrange function results in

$$\mathcal{L}(\boldsymbol{\Omega}, \boldsymbol{\Lambda}) = \mathrm{tr}(\boldsymbol{\Omega\Sigma\Omega}^T) - \mathrm{tr}(\boldsymbol{\Lambda}^T[\boldsymbol{\Omega\Gamma} - \boldsymbol{I}]),$$

where $\boldsymbol{\Lambda}$ is the matrix containing the Lagrange multipliers. The constraint that

must be fulfilled by the minimisation result is apparent in the right part of the Lagrange function. Now, the Lagrange function is minimised by finding an $\boldsymbol{\Omega}$ that solves $\nabla_{\boldsymbol{\Omega}}\mathcal{L}(\boldsymbol{\Omega}, \boldsymbol{\Lambda}) = 0$. Using the identities

$$\frac{\partial}{\partial \boldsymbol{X}}\mathrm{tr}(\boldsymbol{X}\boldsymbol{B}\boldsymbol{X}^T) = \boldsymbol{B}^T\boldsymbol{X}^T + \boldsymbol{B}\boldsymbol{X}^T,$$
$$\frac{\partial}{\partial \boldsymbol{X}}\mathrm{tr}(\boldsymbol{A}\boldsymbol{X}\boldsymbol{B}) = \boldsymbol{B}\boldsymbol{A},$$

the gradient of the Lagrange function becomes

$$\begin{aligned}\nabla_{\boldsymbol{\Omega}} L(\boldsymbol{\Omega}, \boldsymbol{\Lambda}) &= \frac{\partial}{\partial \boldsymbol{\Omega}}\mathrm{tr}(\boldsymbol{\Omega}\boldsymbol{\Sigma}\boldsymbol{\Omega}^T - \boldsymbol{\Lambda}^T[\boldsymbol{\Omega}\boldsymbol{\Gamma} - \boldsymbol{I}]) \\ &= \boldsymbol{\Sigma}^T\boldsymbol{\Omega}^T + \boldsymbol{\Sigma}\boldsymbol{\Omega}^T - \boldsymbol{\Gamma}\boldsymbol{\Lambda}^T \stackrel{!}{=} 0.\end{aligned}$$

All terms in this equation are now transposed, which is possible because the entire equation sums up to zero. From this, one can deduce an expression for the weighting function $\boldsymbol{\Omega}$ that minimises the variance of the analysis $\boldsymbol{x^a}$:

$$\begin{aligned}\nabla_{\boldsymbol{\Omega}} L(\boldsymbol{\Omega}, \boldsymbol{\Lambda}) &= \boldsymbol{\Omega}\boldsymbol{\Sigma} + \boldsymbol{\Omega}\boldsymbol{\Sigma}^T - \boldsymbol{\Lambda}\boldsymbol{\Gamma}^T \\ &= 2\boldsymbol{\Omega}\boldsymbol{\Sigma} - \boldsymbol{\Lambda}\boldsymbol{\Gamma}^T \stackrel{!}{=} 0 \\ \Rightarrow \boldsymbol{\Omega} &= \frac{1}{2}\boldsymbol{\Lambda}\boldsymbol{\Gamma}^T\boldsymbol{\Sigma}^{-1}.\end{aligned} \tag{3.5}$$

Using (3.3), one can rearrange (3.5) to

$$\begin{aligned}\boldsymbol{I} &= \frac{1}{2}\boldsymbol{\Lambda}\boldsymbol{\Gamma}^T\boldsymbol{\Sigma}^{-1}\boldsymbol{\Gamma}, \\ \boldsymbol{\Lambda} &= 2\left[\boldsymbol{\Gamma}^T\boldsymbol{\Sigma}^{-1}\boldsymbol{\Gamma}\right]^{-1}, \\ \Rightarrow \boldsymbol{\Omega} &= \left[\boldsymbol{\Gamma}^T\boldsymbol{\Sigma}^{-1}\boldsymbol{\Gamma}\right]^{-1}\boldsymbol{\Gamma}^T\boldsymbol{\Sigma}^{-1}.\end{aligned}$$

Combining the latter with (3.2) finally yields the analytic solution for the analysis $\boldsymbol{x^a}$ given by

$$\boldsymbol{x^a} = \left[\boldsymbol{\Gamma}^T\boldsymbol{\Sigma}^{-1}\boldsymbol{\Gamma}\right]^{-1}\boldsymbol{\Gamma}^T\boldsymbol{\Sigma}^{-1}\boldsymbol{z}.$$

The optimal estimate of the true state $\boldsymbol{x^t}$ is obtained by linearly weighting information $\boldsymbol{z}$, and weights only depends on the uncertainty of information, given by $\boldsymbol{\Sigma}$, and the operator $\boldsymbol{\Gamma}$ mapping true state to information space. Further, an expression for the analysis error covariance $\boldsymbol{P^a}$ stating the accuracy of the estimate $\boldsymbol{x^a}$ can also be derived. In a first step, an expression for $\boldsymbol{x^a} - \boldsymbol{x^t}$ is found:

$$\begin{aligned}\boldsymbol{x^a} - \boldsymbol{x^t} &= \left[\boldsymbol{\Gamma}^T\boldsymbol{\Sigma}^{-1}\boldsymbol{\Gamma}\right]^{-1}\boldsymbol{\Gamma}^T\boldsymbol{\Sigma}^{-1}\boldsymbol{z} - \boldsymbol{x^t} \\ &= \left[\boldsymbol{\Gamma}^T\boldsymbol{\Sigma}^{-1}\boldsymbol{\Gamma}\right]^{-1}\boldsymbol{\Gamma}^T\boldsymbol{\Sigma}^{-1}\left[\boldsymbol{\Gamma}\boldsymbol{x^t} + \boldsymbol{\xi}\right] - \boldsymbol{x^t} \\ &= \underbrace{\left[\boldsymbol{\Gamma}^T\boldsymbol{\Sigma}^{-1}\boldsymbol{\Gamma}\right]^{-1}\boldsymbol{\Gamma}^T\boldsymbol{\Sigma}^{-1}\boldsymbol{\Gamma}}_{=1}\boldsymbol{x^t} + \left[\boldsymbol{\Gamma}^T\boldsymbol{\Sigma}^{-1}\boldsymbol{\Gamma}\right]^{-1}\boldsymbol{\Gamma}^T\boldsymbol{\Sigma}^{-1}\boldsymbol{\xi} - \boldsymbol{x^t} \\ &= \left[\boldsymbol{\Gamma}^T\boldsymbol{\Sigma}^{-1}\boldsymbol{\Gamma}\right]^{-1}\boldsymbol{\Gamma}^T\boldsymbol{\Sigma}^{-1}\boldsymbol{\xi}.\end{aligned}$$

The analysis error covariance is then computed according to its definition:

$$\begin{aligned}
\boldsymbol{P^a} &= \mathbb{E}\big[(\boldsymbol{x^a} - \boldsymbol{x^t})(\boldsymbol{x^a} - \boldsymbol{x^t})^T\big] \\
&= \mathbb{E}\left[\Big(\big[\boldsymbol{\Gamma}^T\boldsymbol{\Sigma}^{-1}\boldsymbol{\Gamma}\big]^{-1}\boldsymbol{\Gamma}^T\boldsymbol{\Sigma}^{-1}\boldsymbol{\xi}\Big)\Big(\big[\boldsymbol{\Gamma}^T\boldsymbol{\Sigma}^{-1}\boldsymbol{\Gamma}\big]^{-1}\boldsymbol{\Gamma}^T\boldsymbol{\Sigma}^{-1}\boldsymbol{\xi}\Big)^T\right] \\
&= \underbrace{\big[\boldsymbol{\Gamma}^T\boldsymbol{\Sigma}^{-1}\boldsymbol{\Gamma}\big]^{-1}\boldsymbol{\Gamma}^T\boldsymbol{\Sigma}^{-1}\ \underbrace{\mathbb{E}[\boldsymbol{\xi}\boldsymbol{\xi}^T]}_{\boldsymbol{\Sigma}}\ \boldsymbol{\Sigma}^{-1}\boldsymbol{\Gamma}\big[\boldsymbol{\Gamma}^T\boldsymbol{\Sigma}^{-1}\boldsymbol{\Gamma}\big]^{-1}}_{=1} \\
&= \big[\boldsymbol{\Gamma}^T\boldsymbol{\Sigma}^{-1}\boldsymbol{\Gamma}\big]^{-1}.
\end{aligned}$$

The above derivation yields the KF equations for the analysis $\boldsymbol{x^a}$ and its error covariance $\boldsymbol{P^a}$ in a very general form. They are bundled again here:

$$\boldsymbol{x^a} = \boldsymbol{P^a}\boldsymbol{\Gamma}^T\boldsymbol{\Sigma}^{-1}\boldsymbol{z} \qquad , \qquad \boldsymbol{P^a} = \big[\boldsymbol{\Gamma}^T\boldsymbol{\Sigma}^{-1}\boldsymbol{\Gamma}\big]^{-1}. \tag{3.6}$$

It is important to note that the optimal estimate $\boldsymbol{x^a}$ of the true state computed by the BLUE only corresponds to the most probable state when the information error $\boldsymbol{\xi}$ follows a Gaussian distribution.

In order to obtain the KF equations common to atmospheric data assimilation, information contained in $\boldsymbol{z}$ has to be specified. Information $\boldsymbol{z}$ about the true state of the system can be divided into two categories. First, there is the last available model forecast (e.g. from numerical weather prediction) called background or prior estimate $\boldsymbol{x^b}$. Second, there is additional information gathered from multiple observations $\boldsymbol{y^o}$. Therefore, $\boldsymbol{z}$ can be rewritten in a more specific way:

$$\boldsymbol{z} = \Big(\boldsymbol{x^{b}}^T, \boldsymbol{y^{o}}^T\Big)^T. \tag{3.7}$$

Model state vectors $\boldsymbol{x^t}$, $\boldsymbol{x^a}$, and $\boldsymbol{x^b}$ have dimension n, the observation set $\boldsymbol{y^o}$ has dimension p. Generally, p is much smaller than n because the number of atmospheric observations is small compared to the amount of variables and grid points considered in numerical weather prediction nowadays. Total dimension of $\boldsymbol{z}$ sums up to $m = n + p$. Analogous to (3.1), background and observations can be expressed by

$$\boldsymbol{x^b} = \boldsymbol{x^t} + \boldsymbol{\xi^b} \qquad \text{and} \qquad \boldsymbol{y^o} = \boldsymbol{H}\boldsymbol{x^t} + \boldsymbol{\varepsilon}.$$

The $p \times n$ matrix $\boldsymbol{H}$ is called observation operator and maps model space to observation space. The mapped model state $\boldsymbol{H}\boldsymbol{x^t}$ is therefore called the observation equivalent. Model states $\boldsymbol{x^t}$ and $\boldsymbol{x^b}$ are in the same space, therefore no transformation in needed. Thus, the operator $\boldsymbol{\Gamma}$ linking model space to information space has dimension $m \times n$ and can be decomposed according to (3.7):

$$\boldsymbol{\Gamma} = \Big(\boldsymbol{I}_n, \boldsymbol{H}^T\Big)^T. \tag{3.8}$$

The observation operator $\boldsymbol{H}$ is assumed to be linear in this derivation. Following the concept above, the $m \times m$ information error covariance matrix is divided into four sub-matrices:

$$\boldsymbol{\Sigma} = \mathbb{E}[\boldsymbol{\xi}\boldsymbol{\xi}^T] = \begin{bmatrix} \mathbb{E}[\boldsymbol{\xi}^{\boldsymbol{b}}\boldsymbol{\xi}^{\boldsymbol{b}T}] & \mathbb{E}[\boldsymbol{\xi}^{\boldsymbol{b}}\boldsymbol{\varepsilon}^T] \\ \mathbb{E}[\boldsymbol{\varepsilon}\boldsymbol{\xi}^{\boldsymbol{b}T}] & \mathbb{E}[\boldsymbol{\varepsilon}\boldsymbol{\varepsilon}^T] \end{bmatrix}.$$

It is legitimate to assume $\boldsymbol{\xi}^{\boldsymbol{b}}$ and $\boldsymbol{\varepsilon}$ to be statistically uncorrelated because observations and background model state originate from different, unrelated sources. From this and introducing new notations for background and observation error covariances separately, $\boldsymbol{\Sigma}$ simplifies to

$$\boldsymbol{\Sigma} = \begin{bmatrix} \boldsymbol{P}^{\boldsymbol{b}} & 0 \\ 0 & \boldsymbol{R} \end{bmatrix}, \tag{3.9}$$

where $\boldsymbol{P}^{\boldsymbol{b}}$ is the $n \times n$ background error covariance and $\boldsymbol{R}$ the $p \times p$ observation error covariance.

The distinction between observations and background state as two different types of information gathered about the true state $\boldsymbol{x}^{\boldsymbol{t}}$ allows for deriving a more comprehensive form of KF equations presented in (3.6). Inserting (3.7), (3.8) and (3.9) into the analysis expression from (3.6) yields an explicit solution for $\boldsymbol{x}^{\boldsymbol{a}}$ as a function of background state vector $\boldsymbol{x}^{\boldsymbol{b}}$ and observations $\boldsymbol{y}^{\boldsymbol{o}}$. The main steps of the derivation are presented below, showing one intermediate step to demonstrate the computation principle:

$$\begin{aligned} \boldsymbol{x}^{\boldsymbol{a}} &= \underbrace{\left[\boldsymbol{\Gamma}^T\boldsymbol{\Sigma}^{-1}\boldsymbol{\Gamma}\right]^{-1}}_{\boldsymbol{P}^{\boldsymbol{a}}}\boldsymbol{\Gamma}^T\boldsymbol{\Sigma}^{-1}\boldsymbol{z} \\ &= \left[\left(\boldsymbol{I}_n, \boldsymbol{H}^T\right)\begin{bmatrix} \boldsymbol{P}^{\boldsymbol{b}} & 0 \\ 0 & \boldsymbol{R} \end{bmatrix}^{-1}\left(\boldsymbol{I}_n, \boldsymbol{H}^T\right)^T\right]^{-1}\left(\boldsymbol{I}_n, \boldsymbol{H}^T\right)\begin{bmatrix} \boldsymbol{P}^{\boldsymbol{b}} & 0 \\ 0 & \boldsymbol{R} \end{bmatrix}^{-1}\left(\boldsymbol{x}^{\boldsymbol{b}T}, \boldsymbol{y}^{\boldsymbol{o}T}\right)^T \end{aligned}$$

intermediate step reforming $\left(\boldsymbol{I}_n, \boldsymbol{H}^T\right)\begin{bmatrix} \boldsymbol{P}^{\boldsymbol{b}} & 0 \\ 0 & \boldsymbol{R} \end{bmatrix}^{-1}$:

$$\left(\boldsymbol{I}_n, \boldsymbol{H}^T\right)\begin{bmatrix} \boldsymbol{P}^{\boldsymbol{b}} & 0 \\ 0 & \boldsymbol{R} \end{bmatrix}^{-1} \widehat{=} \begin{matrix} n \\ \\ \\ \end{matrix}\overset{\begin{matrix} n & p \end{matrix}}{\begin{bmatrix} \boldsymbol{I}_n & \boldsymbol{H}^T \end{bmatrix}} \cdot \overset{\begin{matrix} n & p \end{matrix}}{\begin{bmatrix} (\boldsymbol{P}^{\boldsymbol{b}})^{-1} & 0 \\ 0 & \boldsymbol{R}^{-1} \end{bmatrix}} \begin{matrix} n \\ p \end{matrix}$$

$$= \begin{matrix} n \\ \\ \\ \end{matrix}\overset{\begin{matrix} n & p \end{matrix}}{\begin{bmatrix} \boldsymbol{I}_n(\boldsymbol{P}^{\boldsymbol{b}})^{-1} & \boldsymbol{H}^T\boldsymbol{R}^{-1} \end{bmatrix}} = \left(\boldsymbol{I}_n(\boldsymbol{P}^{\boldsymbol{b}})^{-1}, \boldsymbol{H}^T\boldsymbol{R}^{-1}\right)$$

$$
\begin{aligned}
\boldsymbol{x^a} =& \left[\Big(\boldsymbol{I}_n(\boldsymbol{P^b})^{-1}, \boldsymbol{H}^T\boldsymbol{R}^{-1}\Big)\Big(\boldsymbol{I}_n, \boldsymbol{H}^T\Big)^T\right]^{-1} \Big(\boldsymbol{I}_n(\boldsymbol{P^b})^{-1}, \boldsymbol{H}^T\boldsymbol{R}^{-1}\Big)\Big(\boldsymbol{x}^{\boldsymbol{b}T}, \boldsymbol{y}^{\boldsymbol{o}T}\Big)^T \\
=& \big[\boldsymbol{I}_n(\boldsymbol{P^b})^{-1}\boldsymbol{I}_n + \boldsymbol{H}^T\boldsymbol{R}^{-1}\boldsymbol{H}\big]^{-1}\Big(\boldsymbol{I}_n(\boldsymbol{P^b})^{-1}, \boldsymbol{H}^T\boldsymbol{R}^{-1}\Big)\Big(\boldsymbol{x}^{\boldsymbol{b}T}, \boldsymbol{y}^{\boldsymbol{o}T}\Big)^T \\
=& \underbrace{\big[(\boldsymbol{P^b})^{-1} + \boldsymbol{H}^T\boldsymbol{R}^{-1}\boldsymbol{H}\big]^{-1}}_{\boldsymbol{P^a}} \big[(\boldsymbol{P^b})^{-1}\boldsymbol{x^b} + \boldsymbol{H}^T\boldsymbol{R}^{-1}\boldsymbol{y^o}\big].
\end{aligned}
\tag{3.10}
$$

The first part in the last line of (3.10) is equal to $\boldsymbol{P^a}$. This expression is further transformed by multiplication with $\big[\boldsymbol{I}_n + \boldsymbol{H}^T\boldsymbol{R}^{-1}\boldsymbol{H}\boldsymbol{P^b} - \boldsymbol{H}^T\boldsymbol{R}^{-1}\boldsymbol{H}\boldsymbol{P^b}\big] = \boldsymbol{I}_n$ and rearranging terms:

$$
\begin{aligned}
\boldsymbol{P^a} &= \big[(\boldsymbol{P^b})^{-1} + \boldsymbol{H}^T\boldsymbol{R}^{-1}\boldsymbol{H}\big]^{-1} \\
&= \big[(\boldsymbol{P^b})^{-1} + \boldsymbol{H}^T\boldsymbol{R}^{-1}\boldsymbol{H}\big]^{-1}\big[\boldsymbol{I}_n + \boldsymbol{H}^T\boldsymbol{R}^{-1}\boldsymbol{H}\boldsymbol{P^b} - \boldsymbol{H}^T\boldsymbol{R}^{-1}\boldsymbol{H}\boldsymbol{P^b}\big] \\
&= \Big[(\boldsymbol{P^b})^{-1} + \boldsymbol{H}^T\boldsymbol{R}^{-1}\boldsymbol{H}\Big]^{-1}\Big[\big[(\boldsymbol{P^b})^{-1} + \boldsymbol{H}^T\boldsymbol{R}^{-1}\boldsymbol{H}\big]\boldsymbol{P^b} - \boldsymbol{H}^T\boldsymbol{R}^{-1}\boldsymbol{H}\boldsymbol{P^b}\Big] \\
&= \boldsymbol{P^a}\big[(\boldsymbol{P^a})^{-1}\boldsymbol{P^b} - \boldsymbol{H}^T\boldsymbol{R}^{-1}\boldsymbol{H}\boldsymbol{P^b}\big] \\
&= \big[\boldsymbol{I}_n - \boldsymbol{P^a}\boldsymbol{H}^T\boldsymbol{R}^{-1}\boldsymbol{H}\big]\boldsymbol{P^b} \\
&\quad \left|\begin{aligned}
\boldsymbol{P^a}\boldsymbol{H}^T\boldsymbol{R}^{-1} &= \boldsymbol{P^a}\boldsymbol{H}^T\boldsymbol{R}^{-1}\big[\boldsymbol{H}\boldsymbol{P^b}\boldsymbol{H}^T + \boldsymbol{R}\big]\big[\boldsymbol{H}\boldsymbol{P^b}\boldsymbol{H}^T + \boldsymbol{R}\big]^{-1} \\
&= \boldsymbol{P^a}\big[\boldsymbol{H}^T\boldsymbol{R}^{-1}\boldsymbol{H}\boldsymbol{P^b}\boldsymbol{H}^T + \boldsymbol{H}^T\big]\big[\boldsymbol{H}\boldsymbol{P^b}\boldsymbol{H}^T + \boldsymbol{R}\big]^{-1} \\
&= \boldsymbol{P^a}\underbrace{\big[\boldsymbol{H}^T\boldsymbol{R}^{-1}\boldsymbol{H} + (\boldsymbol{P^b})^{-1}\big]}_{(\boldsymbol{P^a})^{-1}}\boldsymbol{P^b}\boldsymbol{H}^T\big[\boldsymbol{H}\boldsymbol{P^b}\boldsymbol{H}^T + \boldsymbol{R}\big]^{-1} \\
&= \boldsymbol{P^b}\boldsymbol{H}^T\big[\boldsymbol{H}\boldsymbol{P^b}\boldsymbol{H}^T + \boldsymbol{R}\big]^{-1}
\end{aligned}\right. \\
&= \boldsymbol{P^b} - \boldsymbol{P^b}\boldsymbol{H}^T\big[\boldsymbol{H}\boldsymbol{P^b}\boldsymbol{H}^T + \boldsymbol{R}\big]^{-1}\boldsymbol{H}\boldsymbol{P^b}.
\end{aligned}
\tag{3.11}
$$

With this expression for $\boldsymbol{P^a}$, (3.10) can be developed further:

$$
\begin{aligned}
\boldsymbol{x^a} &= \Big[\boldsymbol{P^b} - \boldsymbol{P^b}\boldsymbol{H}^T\big[\boldsymbol{H}\boldsymbol{P^b}\boldsymbol{H}^T + \boldsymbol{R}\big]^{-1}\boldsymbol{H}\boldsymbol{P^b}\Big]\Big[(\boldsymbol{P^b})^{-1}\boldsymbol{x^b} + \boldsymbol{H}^T\boldsymbol{R}^{-1}\boldsymbol{y^o}\Big] \\
&= \boldsymbol{x^b} + \boldsymbol{P^b}\boldsymbol{H}^T\Big[\boldsymbol{R}^{-1}\boldsymbol{y^o} - \big[\boldsymbol{H}\boldsymbol{P^b}\boldsymbol{H}^T + \boldsymbol{R}\big]^{-1}\boldsymbol{H}\boldsymbol{x^b} \\
&\qquad - \big[\boldsymbol{H}\boldsymbol{P^b}\boldsymbol{H}^T + \boldsymbol{R}\big]^{-1}\boldsymbol{H}\boldsymbol{P^b}\boldsymbol{H}^T\boldsymbol{R}^{-1}\boldsymbol{y^o}\Big] \\
&= \boldsymbol{x^b} + \boldsymbol{P^b}\boldsymbol{H}^T\Big[\Big[\boldsymbol{I}_n - \big[\boldsymbol{H}\boldsymbol{P^b}\boldsymbol{H}^T + \boldsymbol{R}\big]^{-1}\boldsymbol{H}\boldsymbol{P^b}\boldsymbol{H}^T\Big]\boldsymbol{R}^{-1}\boldsymbol{y^o} \\
&\qquad - \big[\boldsymbol{H}\boldsymbol{P^b}\boldsymbol{H}^T + \boldsymbol{R}\big]^{-1}\boldsymbol{H}\boldsymbol{x^b}\Big] \\
&\quad \left|\begin{aligned}
\boldsymbol{I}_n - \big[\boldsymbol{H}\boldsymbol{P^b}\boldsymbol{H}^T + \boldsymbol{R}\big]^{-1}\boldsymbol{H}\boldsymbol{P^b}\boldsymbol{H}^T &= \Big[\big[\boldsymbol{H}\boldsymbol{P^b}\boldsymbol{H}^T + \boldsymbol{R}\big] - \boldsymbol{H}\boldsymbol{P^b}\boldsymbol{H}^T\Big]\Big[\boldsymbol{H}\boldsymbol{P^b}\boldsymbol{H}^T + \boldsymbol{R}\Big]^{-1} \\
&= \big[\boldsymbol{H}\boldsymbol{P^b}\boldsymbol{H}^T + \boldsymbol{R}\big]^{-1}\boldsymbol{R}
\end{aligned}\right.
\end{aligned}
$$

$$\begin{aligned}\boldsymbol{x^a} &= \boldsymbol{x^b} + \boldsymbol{P^b H}^T \left[\left[\boldsymbol{H P^b H}^T + \boldsymbol{R} \right]^{-1} \boldsymbol{y^o} - \left[\boldsymbol{H P^b H}^T + \boldsymbol{R} \right]^{-1} \boldsymbol{H x^b} \right] \\ &= \boldsymbol{x^b} + \boldsymbol{P^b H}^T \left[\boldsymbol{H P^b H}^T + \boldsymbol{R} \right]^{-1} \left[\boldsymbol{y^o} - \boldsymbol{H x^b} \right].\end{aligned}$$

The final form of $\boldsymbol{x^a}$ allows for a comprehensive interpretation of the analysis state obtained after data assimilation using the KF. It reflects the basic functioning of data assimilation, where the best estimate $\boldsymbol{x^a}$ of the true state $\boldsymbol{x^t}$ is obtained from using background information $\boldsymbol{x^b}$ provided by the model and correcting it with a term that contains additional information from observations. This behaviour becomes obvious when looking at the expression for the analysis:

$$\boldsymbol{x^a} = \boldsymbol{x^b} + \overbrace{\underbrace{\boldsymbol{P^b H}^T \left[\boldsymbol{H P^b H}^T + \boldsymbol{R} \right]^{-1}}_{=\boldsymbol{K}} \underbrace{\left[\boldsymbol{y^o} - \boldsymbol{H x^b} \right]}_{\text{innovation vector}}}^{\text{correction term} \propto \boldsymbol{y^o} - \boldsymbol{H x^b}}.$$

$\boldsymbol{K}$: gain matrix

The correction term consists of a weighting term $\boldsymbol{K}$ and a so called innovation vector. The innovation vector contains the difference between model state vector $\boldsymbol{x^b}$ and observations $\boldsymbol{y^o}$. The observation operator $\boldsymbol{H}$ transforms model results into observed variables to be able to make the comparison. Therefore, the innovation vector has dimension p. The Kalman gain matrix $\boldsymbol{K}$ weights the information contained in the innovation vector. These weights depend on the accuracy of both background and observations, represented by $\boldsymbol{P^b}$ and $\boldsymbol{R}$ respectively. An accurate description of the uncertainty of both information sources is therefore crucial to get reliable results from the KF. The term correcting the background $\boldsymbol{x^b}$ must be in model space, therefore the Kalman gain matrix ensures the correct mapping of the innovations $\left[\boldsymbol{y^o} - \boldsymbol{H x^b} \right]$. It also describes links between different variables through covariances in order to apply corrections to all correlated quantities. The expression for the analysis error covariance, (3.11), illustrates a key property of the analysis, since it shows that $\boldsymbol{P^a}$ will always be smaller than $\boldsymbol{P^b}$ (all equation terms are positive definite matrices). This means that by assimilating any observation, independently of its uncertainty, the estimate will always be improved. This holds provided that the observation error covariance is well known. The second term in (3.11) provides the accuracy gain in the analysis compared to the background state before assimilation.

In order to fully describe the KF data assimilation cycle, the temporal aspect must be introduced for forecasting. The transition matrix $\boldsymbol{M}$, which represents the forecast model, evolves the state of the system at time step k to the state at time step $k+1$:

$$\boldsymbol{x}_{k+1}^{\boldsymbol{t}} = \boldsymbol{M x}_k^{\boldsymbol{t}} + \boldsymbol{\eta}_k.$$

Here, $\boldsymbol{M}$ is a matrix and can therefore only describe linear evolution processes. The model error $\boldsymbol{\eta}_k$ is assumed to be unbiased. Furthermore, $\boldsymbol{\eta}_k$ and observation errors $\boldsymbol{\varepsilon}_k$ are uncorrelated, which is not a strong assumption since their sources are different. Introducing the temporal dimension implies knowledge on temporal behaviour of

both observation and model errors. Both are assumed to be uncorrelated in time. The forecast-analysis cycle is closed by defining the new background state at $k+1$ as the evolution of the analysis state obtained at k. By analogy, the background error covariance for $k+1$ is also predicted from the analysis error covariance following

$$\begin{aligned} \boldsymbol{x}_{k+1}^{\boldsymbol{b}} &= \boldsymbol{M}\boldsymbol{x}_k^{\boldsymbol{a}}, \\ \boldsymbol{P}_{k+1}^{\boldsymbol{b}} &= \boldsymbol{M}\boldsymbol{P}_k^{\boldsymbol{a}}\boldsymbol{M}^T + \boldsymbol{Q}, \end{aligned}$$

where $\boldsymbol{Q} = \mathrm{cov}(\boldsymbol{\eta})$ is model error covariance. Using this together with the equations derived above yields the complete set of KF equations with state evolution and analysis:

$$\begin{aligned} \textbf{Analysis:} \quad \boldsymbol{x}_k^{\boldsymbol{a}} &= \boldsymbol{x}_k^{\boldsymbol{b}} + \boldsymbol{K}_k\big[\boldsymbol{y}_k^{\boldsymbol{o}} - \boldsymbol{H}_k\boldsymbol{x}_k^{\boldsymbol{b}}\big], \\ \boldsymbol{P}_k^{\boldsymbol{a}} &= \Big[\boldsymbol{I}_n - \boldsymbol{K}_k\boldsymbol{H}_k\Big]\boldsymbol{P}_k^{\boldsymbol{b}}, \\ \textbf{Forecast:} \quad \boldsymbol{x}_{k+1}^{\boldsymbol{b}} &= \boldsymbol{M}\boldsymbol{x}_k^{\boldsymbol{a}}, \\ \boldsymbol{P}_{k+1}^{\boldsymbol{b}} &= \boldsymbol{M}\boldsymbol{P}_k^{\boldsymbol{a}}\boldsymbol{M}^T + Q, \\ \text{with} \quad \boldsymbol{K}_k &= \boldsymbol{P}_k^{\boldsymbol{b}}\boldsymbol{H}_k^T\big[\boldsymbol{H}_k\boldsymbol{P}_k^{\boldsymbol{b}}\boldsymbol{H}_k^T + \boldsymbol{R}_k\big]^{-1}. \end{aligned} \tag{3.12}$$

A schematic visualisation of the KF cycle is given in Figure 3.1. The above equations can be applied either using the full observation set $\boldsymbol{y}^{\boldsymbol{o}}$ or considering only small batches at a time. Assimilating single observations of $\boldsymbol{y}^{\boldsymbol{o}}$ one after another is referred to as serial data assimilation. It requires the observation errors to be independent.

The presented derivation of the KF can also be considered from another perspective. A derivation of the KF by estimating the conditional mean for a linear filtering problem with Gaussian distributed errors using Bayes' theorem can be found in, e.g. van Leeuwen and Evensen (1996) and Cohn (1997).

The next section introduces the ensemble representation of the error covariance matrices to allow for the evolution of the system by non-linear processes and for reducing memory and computational costs.

3.1.2 The Ensemble Transform Kalman Filter

The formulation of the KF in (3.12) has two major disadvantages when it comes to data assimilation in atmospheric sciences. The first one is the strong non-linearity of processes that cannot be described by a linear operator $\boldsymbol{M}$. The second disadvantage are the associated high computational costs and memory requirements that would arise from storing forecast and analysis background error covariance matrices and analytically solving and evolving the analysis error covariance matrix. Depending on the size of the state controlled by the number of variables and grid points comprised in the model, both tend to have very large dimension. This section presents the Ensemble Kalman Filters (EnKF) addressing those problems.

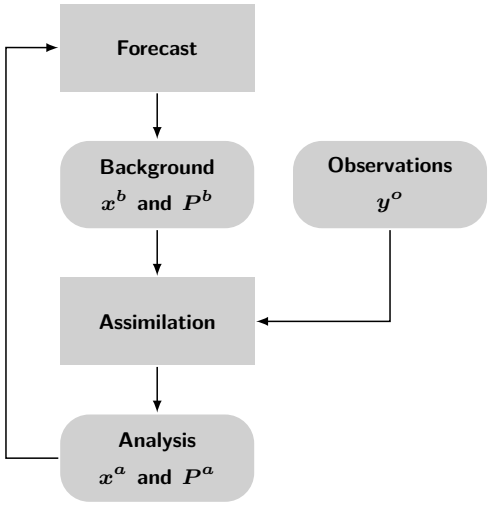

Figure 3.1: Schematic visualisation of the steps in a KF cycle.

The EnKF scheme was proposed by Evensen (1994). Comprehensive formulation and implementation can be found in, e.g. Burgers et al. (1998) and Evensen (2003). Its purpose is to avoid computation and storage of the time evolution of the state error covariance matrices $\boldsymbol{P}_k^{\boldsymbol{b}}$ and $\boldsymbol{P}_k^{\boldsymbol{a}}$ as shown in (3.12). Instead, an ensemble representation of the forecast error covariance of the model state is used to approximate $\boldsymbol{P}_k^{\boldsymbol{b}}$ and $\boldsymbol{P}_k^{\boldsymbol{a}}$ with the sample background and analysis error covariance matrices $\tilde{\boldsymbol{P}}_k^{\boldsymbol{b}}$ and $\tilde{\boldsymbol{P}}_k^{\boldsymbol{a}}$. Stochastic EnKF schemes compute an analysis for each ensemble member using (3.12) and randomly perturbed observations to guarantee a correct estimate of $\tilde{\boldsymbol{P}}_k^{\boldsymbol{a}}$ (Burgers et al., 1998). Deterministic schemes, like the one used here, avoid introducing additional sampling error in the analysis step. Instead, an expression for the analysis ensemble perturbations around the analysis ensemble mean, based on the square root of $\tilde{\boldsymbol{P}}_k^{\boldsymbol{a}}$, is derived in consistency with KF theory. These schemes are called Ensemble Square Root Filters (SRF). A detailed derivation of Ensemble SRF equations and a review on different forms can be found in Tippett et al. (2003).

Ensemble SRF introduce background and analysis state ensembles $\{\boldsymbol{x}_{k,i}^{\boldsymbol{b}} : i = 1, \ldots, l\}$ and $\{\boldsymbol{x}_{k,i}^{\boldsymbol{a}} : i = 1, \ldots, l\}$, holding l members, and corresponding ensemble means $\hat{\boldsymbol{x}}_k^{\boldsymbol{b}}$ and $\hat{\boldsymbol{x}}_k^{\boldsymbol{a}}$. Scaled ensemble perturbation matrices, with dimension $n \times l$, describe the deviation from the ensemble mean:

$$\boldsymbol{Z}_k^{\boldsymbol{b}} = \frac{1}{\sqrt{l-1}}\Big(\boldsymbol{x}_{k,1}^{\boldsymbol{b}} - \hat{\boldsymbol{x}}_k^{\boldsymbol{b}} \quad \boldsymbol{x}_{k,2}^{\boldsymbol{b}} - \hat{\boldsymbol{x}}_k^{\boldsymbol{b}} \quad \ldots \quad \boldsymbol{x}_{k,l}^{\boldsymbol{b}} - \hat{\boldsymbol{x}}_k^{\boldsymbol{b}}\Big),$$
$$\boldsymbol{Z}_k^{\boldsymbol{a}} = \frac{1}{\sqrt{l-1}}\Big(\boldsymbol{x}_{k,1}^{\boldsymbol{a}} - \hat{\boldsymbol{x}}_k^{\boldsymbol{a}} \quad \boldsymbol{x}_{k,2}^{\boldsymbol{a}} - \hat{\boldsymbol{x}}_k^{\boldsymbol{a}} \quad \ldots \quad \boldsymbol{x}_{k,l}^{\boldsymbol{a}} - \hat{\boldsymbol{x}}_k^{\boldsymbol{a}}\Big).$$

During the analysis step of Ensemble SRF, only the analysis of the ensemble mean is computed using the state analysis expression of (3.12). Then, the analysis perturbation matrix $\boldsymbol{Z}_k^{\boldsymbol{a}}$ is determined. With that, the new analysis ensemble can simply

be constructed by computing its members

$$\boldsymbol{x}_{k,i}^{\boldsymbol{a}} = \hat{\boldsymbol{x}}_k^{\boldsymbol{a}} + \sqrt{l-1}\boldsymbol{Z}_{k,i}^{\boldsymbol{a}}, \tag{3.13}$$

where $\boldsymbol{Z}_{k,i}^{\boldsymbol{a}}$ represents the column of $\boldsymbol{Z}_k^{\boldsymbol{a}}$ corresponding to member i. Therefore, the essential part of Ensemble SRF is an expression yielding the ensemble perturbation matrix of the analysis ensemble. Using properties of covariance matrices, which are per definition positive-definite, $\tilde{\boldsymbol{P}}_k^{\boldsymbol{a}}$ can be decomposed into

$$\tilde{\boldsymbol{P}}_k^{\boldsymbol{a}} = \boldsymbol{Z}_k^{\boldsymbol{a}} \boldsymbol{Z}_k^{\boldsymbol{a}T}. \tag{3.14}$$

Therefore, the analysis covariance matrix presented in (3.12) must be further transformed in order to get an expression that can be decomposed into square roots, yielding $\boldsymbol{Z}_k^{\boldsymbol{a}}$. Applying $\tilde{\boldsymbol{P}}_k^{\boldsymbol{b}} = \boldsymbol{Z}_k^{\boldsymbol{b}} \boldsymbol{Z}_k^{\boldsymbol{b}T}$, the analysis error covariance becomes

$$\begin{aligned}
\tilde{\boldsymbol{P}}_k^{\boldsymbol{a}} &= \tilde{\boldsymbol{P}}_k^{\boldsymbol{b}} - \tilde{\boldsymbol{P}}_k^{\boldsymbol{b}} \boldsymbol{H}_k^T \left[\boldsymbol{H}_k \tilde{\boldsymbol{P}}_k^{\boldsymbol{b}} \boldsymbol{H}_k^T + \boldsymbol{R}_k\right]^{-1} \boldsymbol{H}_k \tilde{\boldsymbol{P}}_k^{\boldsymbol{b}} \\
&= \boldsymbol{Z}_k^{\boldsymbol{b}} \boldsymbol{Z}_k^{\boldsymbol{b}T} - \boldsymbol{Z}_k^{\boldsymbol{b}} \boldsymbol{Z}_k^{\boldsymbol{b}T} \boldsymbol{H}_k^T \left[\boldsymbol{H}_k \boldsymbol{P}_k^{\boldsymbol{b}} \boldsymbol{H}_k^T + \boldsymbol{R}_k\right]^{-1} \boldsymbol{H}_k \boldsymbol{Z}_k^{\boldsymbol{b}} \boldsymbol{Z}_k^{\boldsymbol{b}T} \\
&= \boldsymbol{Z}_k^{\boldsymbol{b}} \Big[\boldsymbol{I}_n - \boldsymbol{Z}_k^{\boldsymbol{b}T} \boldsymbol{H}_k^T \left[\boldsymbol{H}_k \boldsymbol{Z}_k^{\boldsymbol{b}} \boldsymbol{Z}_k^{\boldsymbol{b}T} \boldsymbol{H}_k^T + \boldsymbol{R}_k\right]^{-1} \boldsymbol{H}_k \boldsymbol{Z}_k^{\boldsymbol{b}}\Big] \boldsymbol{Z}_k^{\boldsymbol{b}T}.
\end{aligned}$$

Introducing $\boldsymbol{V}_k = \left[\boldsymbol{H}_k \boldsymbol{Z}_k^{\boldsymbol{b}}\right]^T$ one can write

$$\begin{aligned}
\tilde{\boldsymbol{P}}_k^{\boldsymbol{a}} &= \boldsymbol{Z}_k^{\boldsymbol{b}} \Big[\boldsymbol{I}_n - \boldsymbol{V}_k \left[\boldsymbol{V}_k^T \boldsymbol{V}_k + \boldsymbol{R}_k\right]^{-1} \boldsymbol{V}_k^T\Big] \boldsymbol{Z}_k^{\boldsymbol{b}T} \\
&= \boldsymbol{Z}_k^{\boldsymbol{b}} \boldsymbol{T}_k \boldsymbol{T}_k^T \boldsymbol{Z}_k^{\boldsymbol{b}T}.
\end{aligned}$$

Consequently, the analysis perturbation matrix is given as

$$\boldsymbol{Z}_k^{\boldsymbol{a}} = \boldsymbol{Z}_k^{\boldsymbol{b}} \boldsymbol{T}_k.$$

The choice of the matrix square root $\boldsymbol{T}_k$ is not unique and different Ensemble SRF methods exists that differ in the choice of the matrix $\boldsymbol{T}_k$.

The Ensemble Transform Kalman Filter (ETKF) was first suggested by Bishop et al. (2001). Later, a suggestion and correction for an unbiased version of the ETKF was published in Hunt et al. (2007) and Livings et al. (2008). In order to obtain the square root $\boldsymbol{T}_k$, eigenvalue decomposition of $\boldsymbol{I}_n - \boldsymbol{V}_k \left[\boldsymbol{V}_k^T \boldsymbol{V}_k + \boldsymbol{R}_k\right]^{-1} \boldsymbol{V}_k^T$, which can be reformulated to $\left[\boldsymbol{I}_n + \boldsymbol{V}_k \boldsymbol{R}_k^{-1} \boldsymbol{V}_k^T\right]^{-1}$ using the Sherman–Morrison formula, is computed. The eigenvalue decomposition of $\boldsymbol{V}_k \boldsymbol{R}_k^{-1} \boldsymbol{V}_k^T$ is

$$\boldsymbol{V}_k \boldsymbol{R}_k^{-1} \boldsymbol{V}_k^T = \boldsymbol{C}_k \boldsymbol{D}_k \boldsymbol{C}_k^T,$$

where matrices $\boldsymbol{C}_k$ and $\boldsymbol{D}_k$ hold eigenvectors and eigenvalues (on the diagonal), respectively. Then, computation rules for eigenvalues and eigenvectors allow for

building the eigenvalue decomposition

$$\boldsymbol{I}_n - \boldsymbol{V}_k\big[\boldsymbol{V}_k^T\boldsymbol{V}_k + \boldsymbol{R}_k\big]^{-1}\boldsymbol{V}_k^T = \boldsymbol{C}_k\big[\boldsymbol{I}_n + \boldsymbol{D}_k\big]^{-1}\boldsymbol{C}_k^T.$$

With that, the ETKF defines

$$\boldsymbol{T}_k^{\mathrm{ETKF}} = \boldsymbol{C}_k\big[\boldsymbol{I}_n + \boldsymbol{D}_k\big]^{-1/2}\boldsymbol{C}_k^T.$$

Now that $\boldsymbol{T}_k^{\mathrm{ETKF}}$ is defined, it is straight forward to compute the analysis ensemble matrix

$$\boldsymbol{Z}_k^{\boldsymbol{a}} = \boldsymbol{Z}_k^{\boldsymbol{b}}\boldsymbol{T}_k^{\mathrm{ETKF}}, \tag{3.15}$$

and compose the analysis ensemble according to (3.13). The main steps of Ensemble SRF are shown in Figure 3.2. The form of (3.15) shows that the new ensemble perturbations $\boldsymbol{Z}_k^{\boldsymbol{a}}$ are a linear combination of background ensemble perturbations $\boldsymbol{Z}_k^{\boldsymbol{b}}$ before analysis. This ensemble transformation gave its name to the ETKF. Through $\boldsymbol{T}_k^{\mathrm{ETKF}}$, perturbations are weighted according to the members agreement with observations and in consideration of specified observation uncertainties.

Square root decomposition of $\tilde{\boldsymbol{P}}_k^{\boldsymbol{a}}$ allows for reducing computational costs of building $\boldsymbol{K}_k$. Multiplying $\boldsymbol{K}_k$ with $\tilde{\boldsymbol{P}}_k^{\boldsymbol{a}}(\tilde{\boldsymbol{P}}_k^{\boldsymbol{a}})^{-1} = \tilde{\boldsymbol{P}}_k^{\boldsymbol{a}}\big[(\tilde{\boldsymbol{P}}^{\boldsymbol{b}})^{-1} + \boldsymbol{H}^T\boldsymbol{R}^{-1}\boldsymbol{H}\big]$ (see first line of (3.11)) results in

$$\begin{aligned}\boldsymbol{K}_k &= \tilde{\boldsymbol{P}}_k^{\boldsymbol{a}}\boldsymbol{H}_k^T\boldsymbol{R}^{-1}\\ &= \boldsymbol{Z}_k^{\boldsymbol{b}}\boldsymbol{T}_k^{\mathrm{ETKF}}\boldsymbol{Z}_k^{\boldsymbol{b}T}\boldsymbol{T}_k^{\mathrm{ETKF}T}\boldsymbol{H}_k^T\boldsymbol{R}^{-1}.\end{aligned} \tag{3.16}$$

Using $\boldsymbol{Z}_k^{\boldsymbol{b}}$ and $\boldsymbol{Z}_k^{\boldsymbol{a}}$ instead of $\boldsymbol{P}_k^{\boldsymbol{b}}$ and $\boldsymbol{P}_k^{\boldsymbol{a}}$ avoids handling of $n\times n$ matrices in favor of smaller $n\times l$ matrices. Furthermore, it does not require the evolution of $\boldsymbol{P}_k^{\boldsymbol{a}}$ implying $2n$ model integrations, but only l integrations for ensemble members. The number of ensemble members l is in most cases much smaller than the total dimension n of the model state. Additionally, the evolution of ensemble members can be done using a non-linear model $\boldsymbol{\mathcal{M}}$, since sample statistics do not need to be evolved explicitly. In summary, the complete set of ETKF equations is

$$\begin{aligned}
\textbf{Analysis:}\quad \hat{\boldsymbol{x}}_{k+1}^{\boldsymbol{a}} &= \hat{\boldsymbol{x}}_{k+1}^{\boldsymbol{b}} + \boldsymbol{K}_k\big[\boldsymbol{y}_{k+1}^{\boldsymbol{o}} - \boldsymbol{H}_{k+1}\hat{\boldsymbol{x}}_{k+1}^{\boldsymbol{b}}\big]\\
\boldsymbol{Z}_{k+1}^{\boldsymbol{a}} &= \boldsymbol{Z}_k^{\boldsymbol{b}}\boldsymbol{T}_k^{\mathrm{ETKF}}\\
\boldsymbol{T}_k^{\mathrm{ETKF}} &= \boldsymbol{C}_k\big[\boldsymbol{I}_n + \boldsymbol{D}_k\big]^{-1/2}\boldsymbol{C}_k^T\\
\boldsymbol{x}_{k+1,i}^{\boldsymbol{a}} &= \hat{\boldsymbol{x}}_{k+1}^{\boldsymbol{a}} + \sqrt{l-1}\boldsymbol{Z}_{k+1,i}^{\boldsymbol{a}}\\
\textbf{Forecast:}\quad \boldsymbol{x}_{k+1,i}^{\boldsymbol{b}} &= \boldsymbol{\mathcal{M}}(\boldsymbol{x}_{k,i}^{\boldsymbol{a}})\\
\text{with}\qquad \boldsymbol{K}_k &= \tilde{\boldsymbol{P}}_k^{\boldsymbol{b}}\boldsymbol{H}_k^T\big[\boldsymbol{H}_k\tilde{\boldsymbol{P}}_k^{\boldsymbol{b}}\boldsymbol{H}_k^T + \boldsymbol{R}_k\big]^{-1}.
\end{aligned} \tag{3.17}$$

($\boldsymbol{C}_k$ and $\boldsymbol{D}_k$ are eigenvectors and eigenvalues of $\boldsymbol{Z}_k^{\boldsymbol{b}T}\boldsymbol{H}_k^T\boldsymbol{R}_k^{-1}\boldsymbol{H}_k\boldsymbol{Z}_k^{\boldsymbol{b}}$).

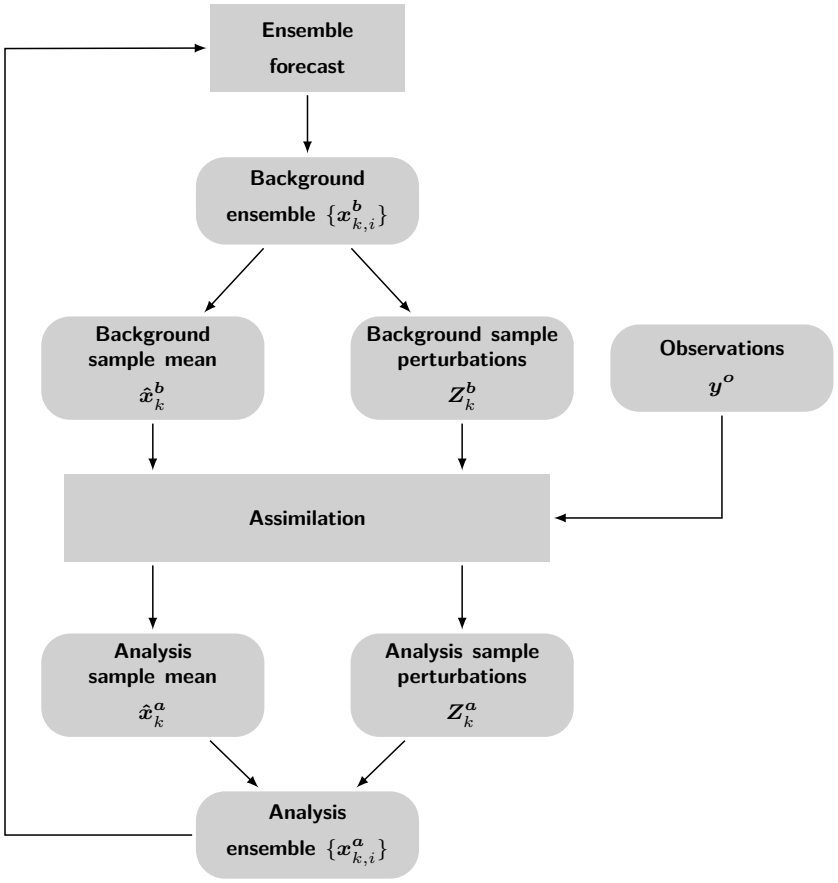

Figure 3.2: Schematic visualisation of the steps in an ensemble SRF cycle.

Despite the great advantages mentioned above, one issue of ensemble SRF is rank deficiency in the estimated sample background and analysis covariance matrices $\tilde{\boldsymbol{P}}^{\boldsymbol{b}}_k$ and $\tilde{\boldsymbol{P}}^{\boldsymbol{a}}_k$. The analysis ensemble perturbations are limited to the subspace spanned by $\boldsymbol{Z}^{\boldsymbol{b}}_k$ which only has rank $l-1$ and cannot describe all degrees of freedom contained in the system. Therefore, it is important that the ensemble members represent all sources of uncertainty relevant to the system. Otherwise, the analysis computed by (3.15) does not allow a good fit to all provided observations. Another issue resulting from the low rank approximation of $\boldsymbol{P}^{\boldsymbol{b}}_k$ is the formation of spurious correlations between model state vector elements at distant grid points. These correlations cause observations to have influence on the analysis at remote locations where there should be no correlation between observation and model variable. The limited ensemble size yields system undersampling that impacts the analysis and can produce nonphysical results. A solution to mitigate these low-rank issues is localisation. Localisation can either be applied by truncating the background covariance matrix $\tilde{\boldsymbol{P}}^{\boldsymbol{b}}_k$ to suppress spurious correlations (e.g. Houtekamer and Mitchell, 1998, 2001), or by performing the analysis on small domains to limit the impact of remote observations. The latter method is used here and a localised version of the ETKF is presented in the next section.

3.1.3 Localisation of the Ensemble Transform Kalman Filter

The ETKF described above calculates the state analysis for all grid points at once. Due to the limited number of ensemble members describing the system, undersampling can produce spurious correlations between locations large distances apart. Localisation of Ensemble SRF emerged to prevent those erroneous correlations from altering the analysis. Hunt et al. (2007) introduced the Local Ensemble Transform Kalman Filter (LETKF), based on previous work from Bishop et al. (2001) and Ott et al. (2004). Its idea is to reduce the size of the domain considered for simultaneous analysis computation. By computing the analysis for different model subregions, i.e. local domains, separately, each can be updated with a different combination of ensemble perturbations according to (3.15). This procedure largely increases the degrees of freedom available in the system. Furthermore, a radius of influence can be assigned to observations to hamper their impact on analysis of remote local domains. Observations considered for a local analysis are called local observations. Figure 3.3 demonstrates the localisation process for local domains comprising one grid point only and observations with limited influence radius. Before performing the analysis, background state ensemble $\{\boldsymbol{x}^{\boldsymbol{b}}_{k,i} : i = 1, \ldots, l\}$ and error covariance matrix $\tilde{\boldsymbol{P}}^{\boldsymbol{b}}_k$ are reduced to the size of the local domain. Once observations are assigned to that domain, observation vector $\boldsymbol{y}^{\boldsymbol{o}}_k$, error covariance matrix $\boldsymbol{R}_k$, and operator $\boldsymbol{H}_k$ must be adjusted to fit new dimensions. Truncating $\boldsymbol{R}_k$ automatically implies that observation errors between different local observation sets are independent, as it is the case in serial data assimilation. After localisation of all required variables, analysis is computed according to ETKF equations derived in Section 3.1.2, for each local domain separately. In order to guarantee a smooth analysis, observations should be used in several neighboring local domains for a continuous impact.

This thesis follows the common approach of domain localisation considering all model grid points separately, as independent local domains. The equation set (3.17) is solved for each grid point of the model domain, which is defined by the radar data composite (Section 2.1.1). The model state is a reflectivity field describing precipitation. The forecast model $\boldsymbol{\mathcal{M}}$ used to evolve the state is the precipitation nowcasting scheme introduced hereafter in Section 3.2. Observations used for data assimilation are radar reflectivity measurements.

3.2 Probabilistic Precipitation Nowcasting

Precipitation nowcasting describes short-term forecasting of precipitation based on the extrapolation of current observations. It is frequently used operationally for real-time forecasting of severe weather to provide information for early warning systems, e.g. flood warnings. The expression 'short-term' is not clearly defined and can refer to anything from minutes to a few hours. Mostly, nowcasting schemes use

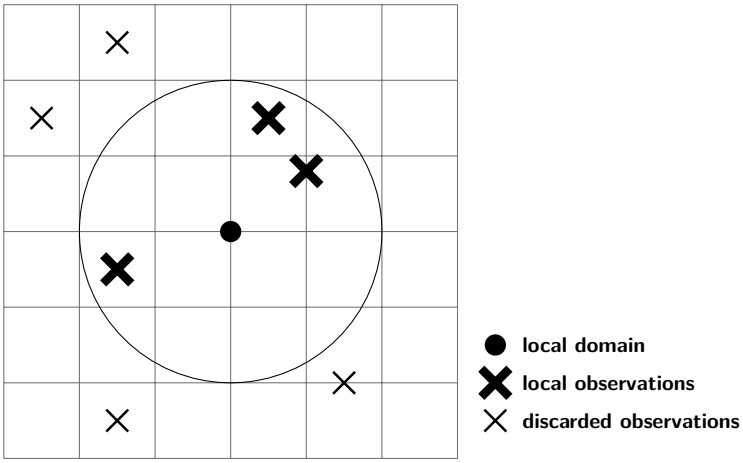

Figure 3.3: Exemplary domain localisation on a regular model grid (solid lines) with local domain (dot) and available observations (crosses). The observation influence radius of two grid boxes length defines considered (thick) and discarded (thin) observations for local analysis.

measurements from weather radars or satellites, some also integrate information from numerical weather prediction. Different nowcasting methods and numerous individual schemes exist. They can be broadly classified in four main nowcasting types: cell tracking methods identifying the displacement of coherent structures (e.g. Rad-TRAM: Kober and Tafferner (2009), TITAN: Dixon and Wiener (1993)), template-matching methods estimating a motion vector field using correlation analysis (TREC: Rinehart and Garvey (1978); Tuttle and Foote (1990), COTREC: Li et al. (1995), GDST: Wolfson et al. (2000)), stochastic methods using statistical models to represent precipitation evolution (S-PROG: Seed (2003), PRAISE: Sirangelo et al. (2007)) and combinations of those methods with numerical weather prediction models (STEPS: Bowler et al. (2006), GANDOLF: Pierce et al. (2000)). A short summary on the history of nowcasting and current progress can be found in Mass (2012).

The nowcasting scheme used for this study is started from composite radar data images (Section 2.1.1). It is a simple, template-matching method based on image correlation analysis to produce short-term precipitation forecasts with up to 30 minutes lead time. The following sections describe the underlying nowcasting scheme from van Horne (2003), which is adapted to fit the requirements of the study. In particular, the nowcasting scheme is extended to generate an ensemble forecast and provide probabilistic nowcasting results. The presented nowcasting scheme only takes into account advection of the precipitation field and is not able to reproduce internal variability and evolution. In return, it is easily implemented and has low computational costs allowing for ensemble computation.

3.2.1 Extrapolation-Based Nowcasting

The nowcasting scheme used in this thesis is a simple approach based on template-matching between precipitation images. The original algorithm, the Automated Precipitation Extrapolator (APEX), was developed by Matthias van Horne (van Horne, 2003) and is adopted here with some modifications. Performance of the original APEX algorithm, with a slightly different implementation than the one used in this work and without the ensemble generation introduced in Section 3.2.2, is analysed in van Horne (2003). It is found to perform at least as good as uniform advection schemes and as the Growth and Decay Storm Tracker (GDST) short-term rainfall forecasting scheme developed at the Massachusetts Institute of Technology (Wolfson et al., 2000) to provide forecast for aviation management.

The algorithm considers two consecutive radar images (image 1 and image 2) and computes an estimate of the precipitation displacement from the first to the second image. A correlation is calculated between image 2 and spatially shifted versions of image 1. The spatial shift is performed in every direction and with different amplitudes and the shift yielding the best correlation allows for estimating the displacement of the precipitation structure between both images. The resulting displacement vector field indicates the precipitation motion direction and speed (an example is given in Figure 3.4). The computed displacement between both images is then used to extrapolate the precipitation structure to its position at future time steps. The APEX algorithm computes a hierarchical correlation analysis considering first the whole domain of the images and then smaller subregions. By this means, it generates spatially variable displacement vectors which allow for small distortions of the precipitation field during the forecast. Therefore, the nowcasting scheme features a component partially representing the uncertainty arising from internal evolution of the field, even though such processes are not specifically implemented.

The nowcasting scheme consists of different steps, describing a forecast cycle from displacement computation at initialisation time to forecast for a defined period and forecast time step (Figure 3.5). These steps are outlined in the following:

Step 1: The initialisation of the nowcasting scheme is performed using two consecutive radar composite images times t_{init} and $t_{\text{init}} - \Delta t_{\text{init}}$, referred to as image 2 and 1, respectively (Figure 3.4). The time interval Δt_{init} between both images must be chosen large enough to allow for detecting the precipitation shift. Since the spatial correlation analysis is performed on a Cartesian grid, original polar radar data is not suitable. Therefore, gridded composite reflectivity data is used. The radar composite images consist of 297×213 pixels with a resolution of $250\,\text{m} \times 250\,\text{m}$ (Section 2.1.1). Both radar composite images are smoothed by convolution with a 5×5 pixels kernel with constant weights to eliminate very small features before proceeding with correlation analysis.

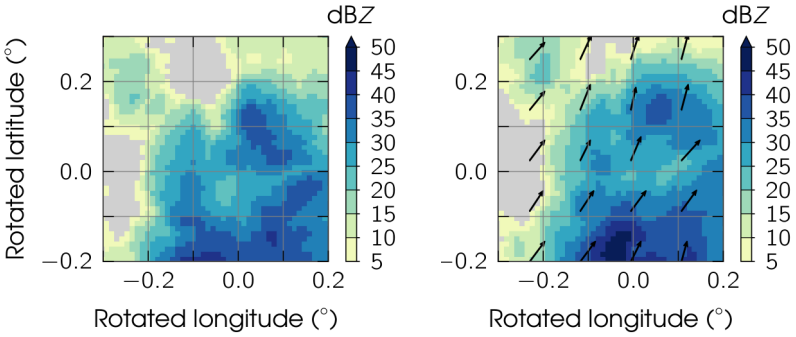

(a) 3rd July 2013, 15:23:00 UTC **(b)** 3rd July 2013, 15:26:00 UTC

Figure 3.4: Example of radar reflectivity composite images 1 **(a)** and 2 **(b)** and computed displacement vectors, zoomed into the inner part of the whole composite domain (Section 2.1.1). Displacement vector field is thinned out to every tenth pixel in each direction in this representation.

Step 2: The computation of the precipitation displacement vector field is performed in two steps. First, a global displacement vector for the whole field is estimated. For that, correlation is calculated between image 2 and spatially shifted versions of image 1 to compute a first estimate of the shift resulting from the precipitation displacement between both images. The displacement vector describes the large scale direction and speed of the precipitation field. In this work, only the inner part of the radar composite images is considered for correlation analysis in order to avoid artefacts from the radar network edge. Precipitation is inevitably truncated beyond radar maximum range, causing a fixed structure in the fields that can falsify obtained correlations. Therefore, the considered part of image 1 that is shifted and matched to precipitation structures of image 2 is limited to a region of 160×140 pixels in the middle of the full 297×213 pixels domain (Section 2.1.1). Then, a normalised cross-correlation is performed between the truncated version of image 1 and whole image 2, testing every possible position of image 1 in image 2. For details on the computation of normalised cross-correlations, refer to Lewis (1995). The global precipitation displacement vector arises from the position of image 1 in image 2 yielding the highest correlation. This global displacement vector is first computed as a shift of pixels per time step, but can easily be converted into velocity in $\mathrm{m\,s^{-1}}$ and adapted to different forecast time steps with knowledge of the image resolution ($250\,\mathrm{m} \times 250\,\mathrm{m}$) and the time interval between the two input images (Δt_{init}).

Step 3: The second step of the computation of the displacement vector field is the refinement of the global displacement vector to a variable vector field with pixelwise adjustment. The global motion vector, which only indicates overall displacement of precipitation, is refined by computing local displacement vectors

on smaller regions of the radar composite images. For this, image 1 is shifted according to the global displacement vector to account for the dominant motion of the precipitation field. The local component of the displacement vector in computed in Step 4.

Step 4: The correlation analysis described in Step 2 is performed again on smaller subregions of the radar composite images. Only pixels with precipitation intensity above the no-precipitation threshold of 5 dBZ (established in Section 2.1.1) are considered. An area of 21×21 pixels around each of these pixels in the shifted version of image 1 is compared to image 2. The maximum allowed shift for this local adjustment is 10 pixels in each direction. The computed local adjustments are added to the global displacement vector in order to obtain a vector for every pixel. The global displacement vector is assigned to pixels without precipitation. The effect of the refinement of the displacement vector field is visible in Figure 3.4, where the depicted vectors show small, individual deviations from a global displacement towards north east.

Step 5: The complete displacement vector field is used to compute the precipitation forecast. For this, displacement vector lengths are scaled to the wanted forecast time step and the future position of the precipitation field in image 2 is predicted accordingly. In order to get a smooth, continuous reflectivity field after the advection, a 3×3 window of pixels around each pixel is shifted to its new position. If more than one reflectivity value is attributed to a pixel of the forecasted reflectivity field, values are averaged, as illustrated in Figure 3.6. Pixels in the forecasted field to which no value is attributed are filled with the default no-precipitation value (5 dBZ). The displacement vector field is advected together with the precipitation field to provide consistent forecast. Default value for the displacement vector is the computed global vector (Step 2). If more than one forecast step is required, above advection procedure (Step 5) is repeated with the newly obtained reflectivity and displacement vector fields.

Domain size and resolution as well as relevant settings for the nowcasting scheme implementation are gathered in Table 3.1. Especially, some threshold applied to the computed displacement vector fields to filter erroneous values are given. The table also includes settings related to the ensemble generation introduced in Section 3.2.2.

Due to the computation of local displacement vectors at each pixel covered with precipitation, some divergence and rotation is allowed in the vector field. The original precipitation can therefore be distorted during the forecasting process, accounting for some internal variability in the structure of the precipitation field. Precipitation intensity can change compared to the initial field due to the averaging in the forecasting step, but no cell decay or growth model is integrated in the nowcasting

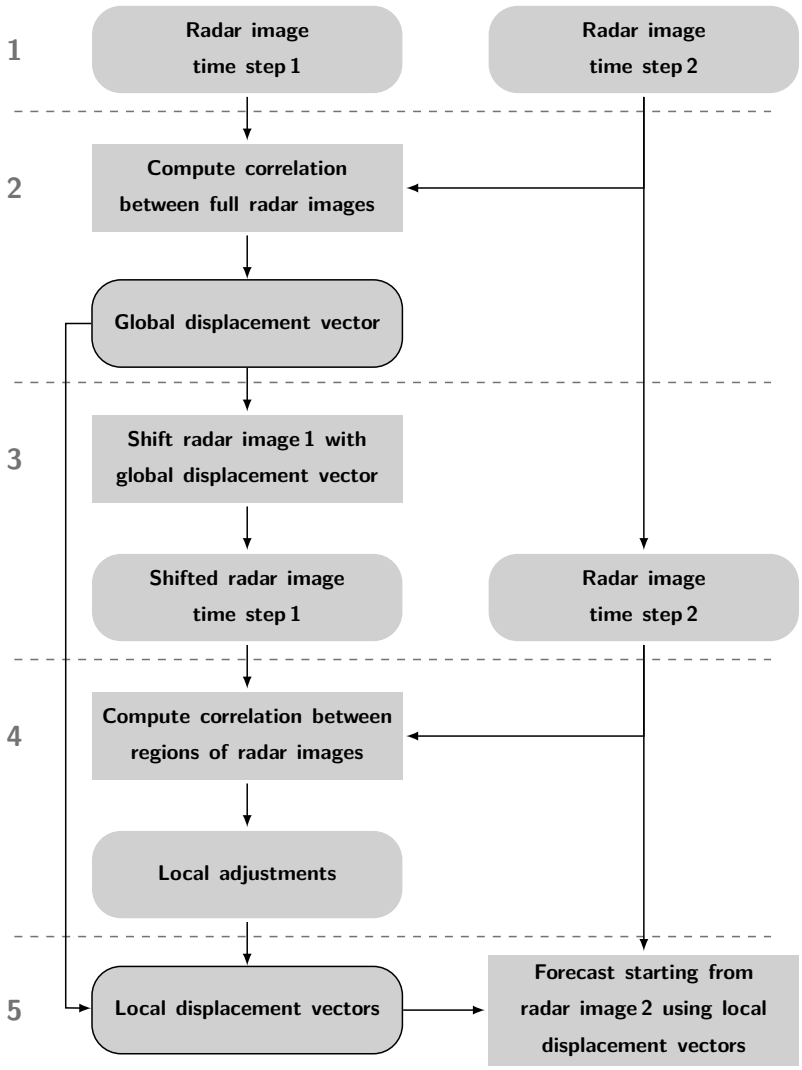

Figure 3.5: Flowchart of the main components of the nowcasting process, comprising displacement vector computation and forecasting. The steps describe a single forecast with initialisation using radar images 1 and 2.

scheme. Nevertheless, the distortion and intensity changes in the field provide a tool to represent some variability in the precipitation field. The steps presented above describe the initialisation of the forecast and the computation of one forecast. To run the nowcasting scheme in a cycle, the initialisation time is updated and the process repeated from Step 1.

This nowcasting model is deterministic and produces a forecast without information on forecast uncertainty and on other possible precipitation evolution scenarios. To introduce a probabilistic component to the forecast and to allow for coupling the model with the LETKF presented in Section 3.1.3, the nowcasting scheme is extended to provide ensemble forecasts in the following section.

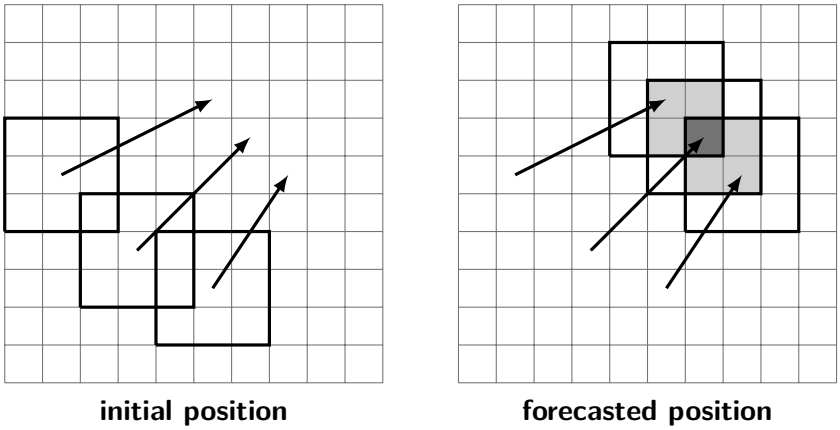

Figure 3.6: Schematic representation of the forecasting step for three pixels, exemplary. 3×3 windows of pixels (initial position left) are shifted according to the local motion vectors calculated for the center pixel. If these pixel windows overlap in the forecast (new position right), pixel values (reflectivity or motion velocity) are averaged to get the forecasted field. In this example light grey pixels are averages over two values, dark grey over three values.

Table 3.1: Settings of the probabilistic nowcasting scheme. For more details on the definition and tuning of single settings refer to van Horne (2003) or Eckmann (2016).

Nowcasting data and domain	
Input data	composite radar data
Full domain size	297×213 pixels
Resolution	$250\,\mathrm{m} \times 250\,\mathrm{m}$
Global displacement computation	
Data smoothing window	5×5 pixels
Inner domain for corr. analysis	160×140 pixels
Max. allowed glob. speed	$22\,\mathrm{m\,s^{-1}}$
Min. required correlation	0.5
Local displacement computation	
Domain for corr. analysis	21×21 pixels
Max. allowed loc. adjustment	10×10 pixels
Max. deviation from glob. speed	25 %
Max. allowed angle to glob. vector	30°

3.2.2 Ensemble Forecast Generation

The nowcasting scheme described above in Section 3.2.1 is deterministic. One displacement vector field is computed from two radar images and the forecast is computed using this field. Since this one realisation of the forecast is not necessarily correct, other possible realisations and their probability to occur are a valuable addition to the forecast. A probabilistic forecast can be obtained by construct-

ing an ensemble of forecasts that represents different possible realisations of the future. The ensemble then allows to estimate probabilities of certain scenarios to occur, provided that the ensemble spread and distribution match the statistics of the considered system. Given that, it is possible to estimate the forecast uncertainty through the spread of the model ensemble, often described by the ensemble standard deviation.

A simple approach is chosen to create an ensemble forecast from the deterministic forecast: an ensemble of displacement vector fields is generated from the deterministic displacement vector field by randomly perturbing its x- and y-components. The aim of the ensemble generation process is to produce a smooth perturbation of the displacement vector field. Therefore, the random noise from which the perturbations are built must be spatially correlated to avoid fuzzy and inconsistent displacement vectors. To create the pattern of the spatial correlation, areas with high wind speeds are assumed to behave similarly, i.e. vectors with large displacement magnitude are strongly correlated. By this means, information from the precipitation field is incorporated into the correlation pattern, which is probably more accurate than assuming a Gaussian correlation structure or a purely mathematical correlation description without any relation to the field values. Following method is applied to implement such a spatially correlated noise generation.

Correlated random noise $\boldsymbol{u}_{\text{corr}}$ is generated from uncorrelated random numbers $\boldsymbol{u}$ drawn from the standard normal distribution by multiplying it by the lower triangle matrix $\boldsymbol{L}$, obtained from the Cholesky decomposition $\boldsymbol{S} = \boldsymbol{L}\boldsymbol{L}^T$ of the desired covariance matrix $\boldsymbol{S}$:

$$\boldsymbol{u}_{\text{corr}} = \boldsymbol{L}\boldsymbol{u} + \boldsymbol{1}. \tag{3.18}$$

Here, $\boldsymbol{1}$ is an all-ones vector defining the mean of the correlated random noise $\boldsymbol{u}_{\text{corr}}$. The covariance matrix $\boldsymbol{S}$, which defines the structure of the noise correlation, has to be prescribed. As mentioned above, $\boldsymbol{S}$ is built here based on the spatial distribution of the displacement vector magnitude in the field. Per definition, the covariance matrix $\boldsymbol{S}$ has to be symmetric and positive definite. It is computed by multiplying the displacement vector magnitude $\boldsymbol{f}$ by its transpose:

$$\boldsymbol{S} = \boldsymbol{f} \otimes \boldsymbol{f}^T + \boldsymbol{I},$$

where $\boldsymbol{f}$ is previously reformed from a two-dimensional field to a vector. Adding the identity matrix $\boldsymbol{I}$ ensures that $\boldsymbol{S}$ is actually positive definite. Next, the covariance matrix is scaled such that its diagonal maximum value fits a desired maximum noise variance σ^2_{noise}, determining the maximum amplitude of the perturbations in the field. Perturbation variance decreases with decreasing displacement vector magnitude, reducing the amplitude of the perturbations for shorter displacement vectors. This behaviour has the advantage of reducing the amplitude of perturbations at smaller displacement vector magnitudes, where perturbations are weakly correlated

and more prone to inconsistency in the field than in the case of large magnitudes. The decreased variance dampens the fuzziness of the perturbations at low displacement vector magnitudes. After the construction of $\boldsymbol{S}$, the lower triangle matrix $\boldsymbol{L}$ of the covariance matrix $\boldsymbol{S}$ can be computed using Cholesky decomposition and allows for the ensemble nowcasting generation.

For each ensemble member, $\boldsymbol{u}$ is drawn independently for the x- and y-components of the displacement vector field, and an ensemble of random correlated noise fields $\boldsymbol{u}_{\text{corr}}$ is computed with (3.18). The noise $\boldsymbol{u}_{\text{corr}}$ has same mean 1 and variance σ^2_{noise} for both components of the displacement vectors. The deterministic displacement vector field is then multiplied by the obtained ensemble of correlated random noise fields to build an ensemble of different initial displacement vector fields. For the probabilistic forecast, the precipitation field is advected with each member of the displacement vector field ensemble according to the advection technique described in Step 5 in Section 3.2.1. In this thesis, $\sigma^2_{\text{noise}} = 0.4$ is chosen. A short sensitivity study with different values of σ^2_{noise} and a summary of the important settings of the nowcasting scheme are given in Section 3.2.3.

3.2.3 Nowcasting Settings

The probabilistic version of the nowcasting scheme used in this thesis is introduced in Section 3.2.2. An ensemble of forecasts is generated by perturbing the deterministically computed displacement vector field using correlated random noise following (3.18). The variance of this noise, i.e. the amplitude of the perturbations, is determined by σ^2_{noise}. The choice of σ^2_{noise} determines the initial spread of the ensemble of displacement vector fields and therefore also controls the spread of the resulting ensemble precipitation forecast.

In this study, $\sigma^2_{\text{noise}} = 0.4$ is chosen. Results from a short sensitivity study analysing the behaviour of the ensemble forecast with different σ^2_{noise} is presented in Figure 3.7. Using radar composite images (Section 2.1.1), an ensemble forecast with 50 members is started every two minutes in the time interval from 13:15:00 UTC to 15:15:00 UTC, yielding 60 forecasts. Each forecast has a maximum lead time of 20 minutes, with time steps of two minutes. Forecast ensemble mean is compared to actual composite radar observations at the corresponding time. Since nowcasting and composite radar data are on the same grid, pixels can be directly compared. The root mean square error (RMSE) between forecast ensemble mean and observation for all forecasts with the same lead time is computed, as well as the average ensemble spread for these forecasts, i.e. ensemble standard deviation. Results are computed over all pixels of the nowcasting domain. This analysis is performed with $\sigma^2_{\text{noise}} =$ 0.1, 0.2, 0.4, and 0.6. As expected, the forecast error (RMSE) and the ensemble spread (ensemble standard deviation) increase with increasing lead time. The fore-

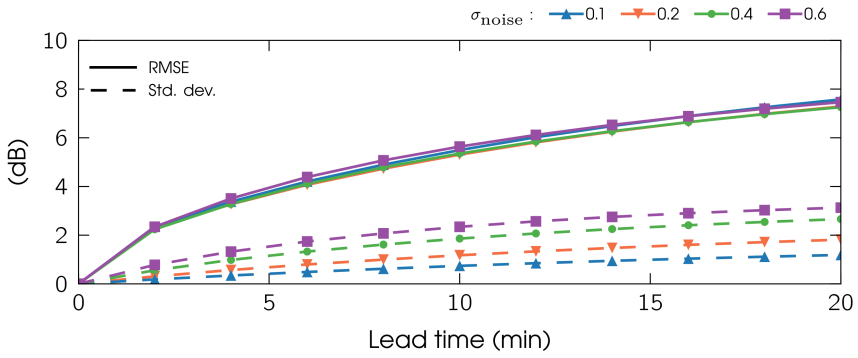

Figure 3.7: RMSE and ensemble standard deviation of the reflectivity ensemble forecasts as a function of lead time and for different values of σ^2_{noise}.

cast is underdispersive in all four cases, since the error of the forecast (RMSE) is higher than the uncertainty indicated by the ensemble standard deviation.

One reason for the low spread of the system is the missing representation of the uncertainty arising from internal cell development, e.g. growth and decay processes or splitting and merging of cells. As already mentioned (Section 3.2.1), the variable displacement vector field allows for some inner distortion of the precipitation field. Through the generation of the ensemble of displacement vector fields for the probabilistic forecast, uncertainty due to inner processes of the cell is partly represented. But this effect is too small to account for the high temporal variability of precipitation evolution. The uncertainty of the presented probabilistic nowcasting scheme is underestimated by the ensemble. Also, the spread of the system only increases slowly with lead time and appears to saturate. Due to the ensemble generation process perturbing only the displacement vector field, the precipitation cell is advected to different locations in each ensemble member during the forecast. After a number of time steps, precipitation predicted by the different ensemble members is dispersed over a large area and the ensemble spread does not noticeably increase with further spreading of the cell.

The spread of the ensemble forecast increases with larger σ^2_{noise} whereas the forecast error stays nearly the same. $\sigma^2_{\text{noise}} = 0.4$ is chosen here as the setting yielding the smallest discrepancy between ensemble spread and forecast error ($\sigma^2_{\text{noise}} = 0.6$ show a similar deviation between RMSE and standard deviation, but with higher forecasting error). Relevant settings related to the implementation of the introduced probabilistic nowcasting scheme in this thesis are summarised in Table 3.1.

3.3 Framework Design and Implementation

This thesis has the objective of combining precipitation nowcasting and observations in a statistically meaningful way, by considering the respective uncertainty.

The combination method used is the LETKF presented in Section 3.1.3. A framework that allows to couple nowcasting and observations using the LETKF was implemented during the work of this thesis. The framework is implemented in Python and makes use of object-oriented programming. It consists of a collection of modules and abstract classes, designed to be easily extendable and to be coupled to different forecasting models and multiple observation types. The design and implementation was done in collaboration with Dr. Gernot Geppert. In the following, main parts of the framework used for the analysis of this thesis are described to provide an overview of its structure. The description refers to data assimilation terminology introduced in Section 3.1.3.

The overall functioning of the data assimilation framework is shown in Figure 3.8. It allows for performing a data assimilation cycle with a data assimilation method coupled to a forecast model. The model must be initialised to run an ensemble forecast. Different observations types and configurations, gathered in observation sets here, can be considered to perform the analysis. Observations of different variables, from different instruments, at different locations, and available at different time steps can be used in one experiment. Following the typical data assimilation cycling procedure, an ensemble forecast is performed until an observation is available. Then, an observation equivalent ensemble is computed from the ensemble forecast in order to perform the analysis. From this analysis, a new forecast is started until the time of the next observation is reached, and the assimilation process starts again. After the last observation available in the forecast interval, a free forecast is run until forecast end.

The data assimilation framework in Figure 3.8 is module-based and consists of a number of single components. The most important components and associated classes are presented in Figure 3.9 to Figure 3.13 and described in the following, focusing only on parts used in this study. Also, methods and attributes related to the data assimilation process are shown, but everything related to the underlying computational process (e.g. handling dimensions, matching locations, input and output) is excluded. A few technical details on data assimilation analysis computation are also given.

Data assimilation method: The core of the data assimilation framework is the filter method performing the analysis. This framework is designed for ensemble filters. It includes the LETKF as a class derived from a class implementing the ETKF (Figure 3.9). Each assimilation method is implemented as a class with an `analysis()` method that performs the analysis by solving the data assimilation equations based on the background ensemble and provided observations. The background ensemble stored in the Ensemble class (Figure 3.10) is then replaced by newly computed analysis ensemble by the `update()` method. The analysis is performed according to (3.17) with some adjustments needed for

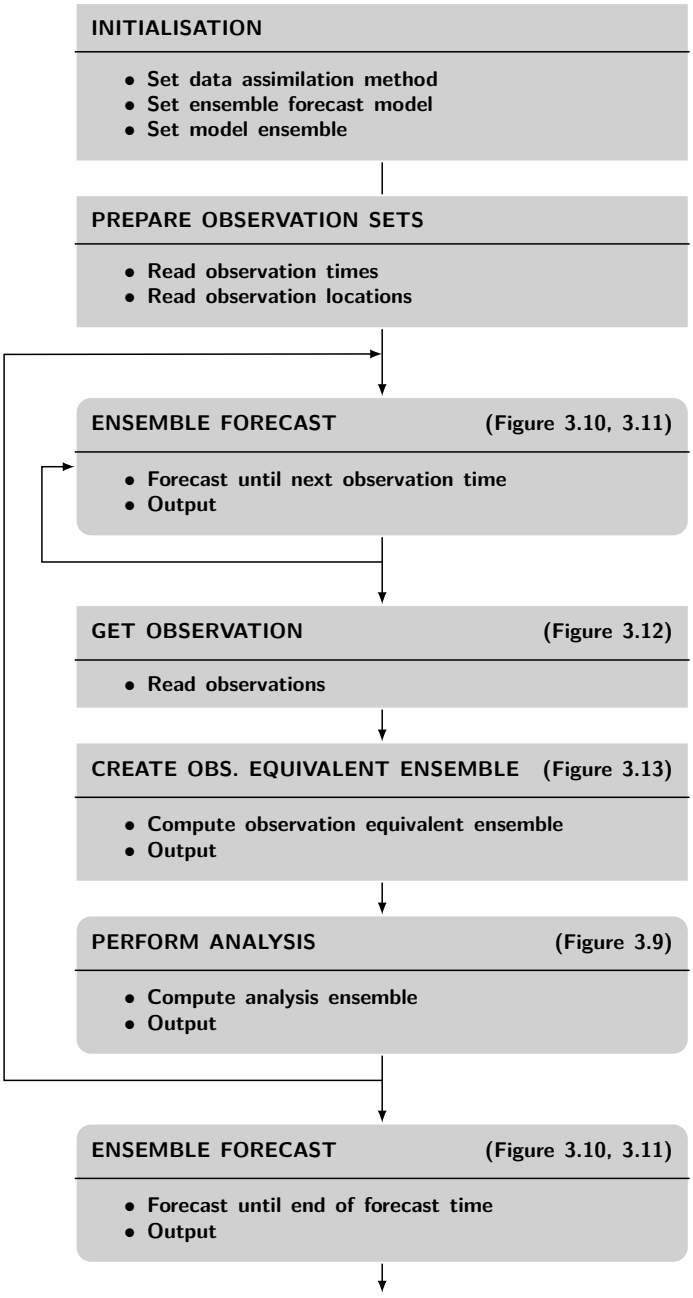

Figure 3.8: Main steps of the data assimilation cycle performed with the developed framework. Figure references indicate diagrams of the classes used to compute the respective steps.

computational reasons, to avoid large matrices and soften assumptions on the observation operator.

The observation equivalent ensemble $\left\{\boldsymbol{H}_k \boldsymbol{x}^{\boldsymbol{b}}_{k,i} : i = 1, \ldots, l\right\}$ is calculated beforehand by applying the observation operator on each model member. $\boldsymbol{H}_k \hat{\boldsymbol{x}}^{\boldsymbol{b}}_k$, $\boldsymbol{H}_k \boldsymbol{Z}^{\boldsymbol{b}}_k$ and $\boldsymbol{Z}^{\boldsymbol{b}T}_k \boldsymbol{H}^T_k = \left[\boldsymbol{H}_k \boldsymbol{Z}^{\boldsymbol{b}}_k\right]^T$ are then computed directly from the observation equivalent ensemble by splitting it into mean and perturbations. On

the one hand, this implementation avoids to apply the observation operator multiple times. On the other hand, it also resolves the restriction of a linear observation operator. In the case of a non-linear observation operator $\boldsymbol{\mathcal{H}}_k$, its application on background perturbations $\boldsymbol{Z}_k^{\boldsymbol{b}}$ is not appropriate because it does not preserve additivity. By computing the perturbations of the observation ensemble from $\{\boldsymbol{\mathcal{H}}_k(\boldsymbol{x}_{k,i}^{\boldsymbol{b}}) : i = 1, \ldots, l\}$, it is possible to give a good estimation of $\boldsymbol{H}_k\boldsymbol{Z}_k^{\boldsymbol{b}}$ and $\boldsymbol{Z}_k^{\boldsymbol{b}T}\boldsymbol{H}_k^T$, where $\boldsymbol{H}_k$, in this case, is the linearisation of $\boldsymbol{\mathcal{H}}_k$ about $\hat{\boldsymbol{x}}_k^{\boldsymbol{b}}$ (Hunt et al., 2007). In the case of a linear observation operator, this yields exactly $\boldsymbol{H}_k\boldsymbol{Z}_k^{\boldsymbol{b}}$ and $\boldsymbol{Z}_k^{\boldsymbol{b}T}\boldsymbol{H}_k^T$. Also, first generating the observation equivalent ensemble makes the computation of local analysis for all considered local domains in the LETKF completely independent. The analysis can therefore easily be parallelised. Another optimisation is the computation of the gain matrix $\boldsymbol{K}_k$ according to (3.16) rather then using the form presented in (3.17). Computational advantages, i.e. smaller resulting matrices and avoiding the evolution of error covariance matrices, are described in Section 3.1.2.

Forecast model: Generally, any ensemble forecast model can be coupled to the framework by deriving a new class. The nowcasting scheme presented in Section 3.2 is implemented in a class derived from the abstract Forecast Model class (Figure 3.11). It can be initialised as an ensemble (`init_ensemble()`) or as just one member (`init_model()`). The Forecast Model class holds all model variables needed for its description and during the forecasting process performed by `forecast()`: `dimensions`, `time`, `variables`, `filter_locations`. If the complete state of the system is not considered during the assimilation step, the method `get_filter_state()` selects just the relevant parts out of the complete state. These parts will generally be specific variables, but could also be certain regions of the modelled system. Location information of the selected elements is also contained in the Forecast Model class for correct collocation with observations. The method `update_state()` sorts the state analysis computed by the data assimilation method into the complete system state. Basically, it is the inverse process to `get_filter_state()`. The localisation process in the LETKF requires to split the complete model region into local domains, which have to be specified in `domains`. By default, each grid point of the model domain is defined as one local domain (Hunt et al., 2007). The nowcasting scheme used here has areal reflectivity as system state (`reflectivity_field`). It also needs global and local motion vectors (`global_motion_vector`, `local_motion_vectors`), as described in Section 3.2. `get_displacement()` computes these motion vectors.

Observations: Information about different observations types is stored in instances of the Observation Set class (Figure 3.12). One observation set holds all metadata needed to read the observations values requested for the current assimilation step (`filename`, `locations`, `obs_times`). The actual observation val-

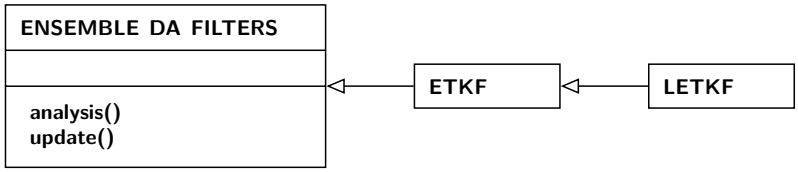

Figure 3.9: Diagram of the abstract Ensemble Data Assimilation Filter class with derived classes for the ETKF and the LETKF.

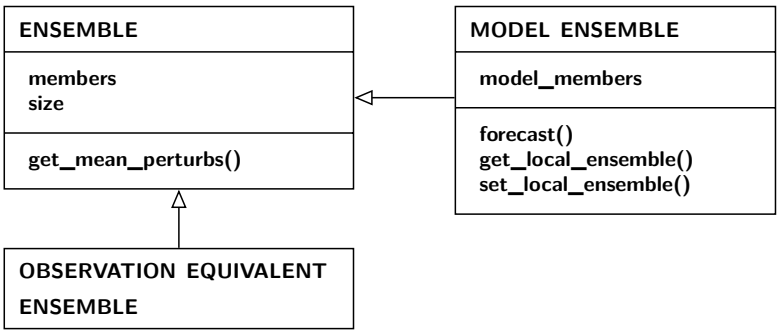

Figure 3.10: Diagram of the abstract Ensemble class and derived classes for model ensembles and observation equivalent ensembles (Model Ensemble class and Observation Equivalent Ensemble class).

ues are successively stored in instances of the Observation class. In order to minimise the required memory space they are stored only during the time step they are used for assimilation. Observation sets also specify which observation operator (`obs_operator`) fits the observation types and where to find the observation error covariance matrix (`covariance_filename`). Furthermore, observation sets must provide the information needed for the localisation process of the LETKF: the length of the observation influence radius (`obs_influence_radius`) and the method `get_obs_domains()` which assigns the observation to the correct model domains considering the influence radius. `obs_domains` then stores the indices of the observation array relevant for each model domain. The Observation class as such provides the method to read the current observation values (`read_obs_from_file()`) and stores `time`, `locations` and the variables (`value`). It also provides the observation error covariance, which can either be a diagonal variance or a full covariance matrix.

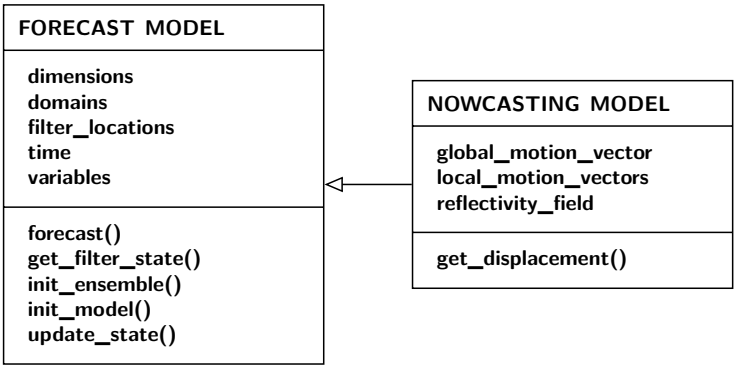

Figure 3.11: Diagram of the abstract Forecast Model class and derived class for the nowcasting method implemented for this study (Nowcasting Model class).

Observation operator: Each observation type needs a specific observation operator computing corresponding observation equivalents from the model state. The LETKF requires an observation equivalent ensemble holding observations computed based on the background state ensemble. The observation equivalent ensemble is stored in the Observation Equivalent Ensemble class (Figure 3.10). An operator has to be implemented for each observation type to return an observation given the filter state vector and the locations of both filter state elements and observations. The Observation Operator class (Figure 3.13) holds the observation variable types (`variables`) and must provides the method `calc_obs_ensemble()` that generates the observation equivalent ensemble. The method `get_filter_state_indices()` allows for selecting all elements of the filter state vector needed to generate the observation equivalent. Since the precipitation nowcasting scheme used in this work provides a forecast of reflectivity fields and observations are radar reflectivity, the implemented observation operator in the XBand Radar Operator class represents the identity.

Ensemble: Since the data assimilation framework is designed for ensemble data assimilation filters, forecast and observation equivalent ensemble members are gathered in order to be able to compute ensemble mean and perturbations, i.e. deviations from the mean. Ensemble members are handled by the abstract Ensemble class (Figure 3.10) that computes ensemble mean and perturbations (`get_mean_perturbs()`) and holds all ensemble members (`members`) and ensemble size (`size`). Two specific classes are derived from there for both ensemble types occurring in the data assimilation framework: a Model Ensemble class and an Observation Equivalent Ensemble class. The Model Ensemble class must perform the ensemble forecast (`forecast()`). The forecast is performed independently for each ensemble member and can therefore easily be computed in parallel. An important feature of the Model Ensemble class is

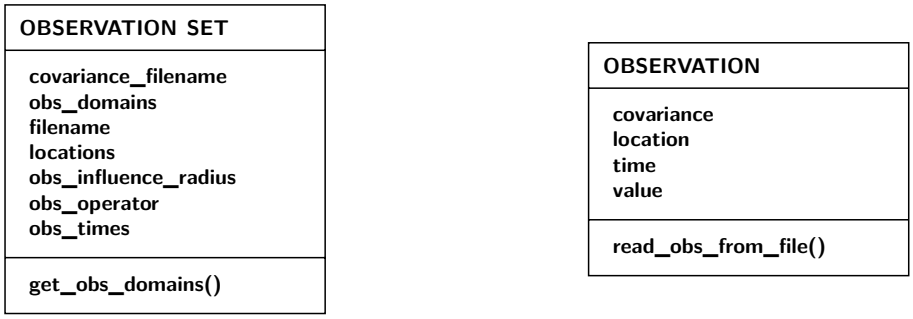

Figure 3.12: Diagram of the abstract Observation Set and Observation classes.

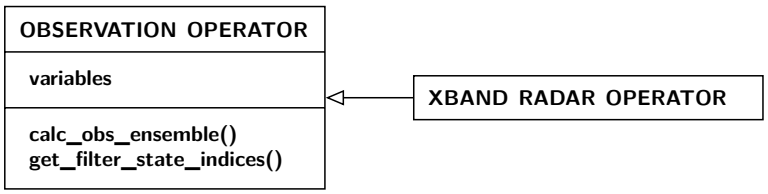

Figure 3.13: Diagram of the abstract Observation Operator class and derived class for the observation operator implemented for X-band radar data in this study (Xband Radar Operator class).

the method assembling the filter state ensemble for local domains. For this, state vector elements matching local domain locations are gathered through all members by the method `get_local_ensemble()`. After the analysis step, members of the local domain analysis ensemble are allocated to the correct part of the state vector and to the adequate variables within the Forecast Model class by the method `set_local_ensemble()`.

4 Method and Data Assimilation Experiment

After the implementation of the framework described in Chapter 3, a proof of concept study is performed to assess the functioning of the framework and the potential of the presented uncertainty estimation method. The method combines precipitation information from different sources in order to obtain a combined, areal product and additionally estimates its uncertainty. Every available precipitation measurement can be assigned a specific uncertainty information. This information can have different degrees of accuracy, from constant to spatially and temporally variable. By combination of both data and uncertainty information through a data assimilation method and the use of a nowcasting method, flow dependency is introduced to the areal uncertainty estimate, as known uncertainty propagates with the precipitation displacement. This method yields a situation dependent uncertainty whose structure follows the physics of the system.

This chapter addresses the description of the performed data assimilation experiment and demonstrates the proper functioning of the implemented data assimilation framework. The performed data assimilation cycle is outlined and the system settings are described, together with an assessment of the experiment validating the data assimilation system. The assessment of the experiment is important to establish a reliable foundation for the proof of concept of the presented method. The potential of the resulting spatially and temporally variable uncertainty information associated with the combined precipitation product is analysed and demonstrated in Chapter 5.

4.1 Experiment Setup and Description

The network radar data and the ensemble nowcasting data assimilation framework presented in Chapter 2 and Chapter 3, respectively, are used to run a data assimilation experiment allowing for the assessment of the uncertainty estimating method. The purpose of the experiment is to prove the functioning of the implement frame-

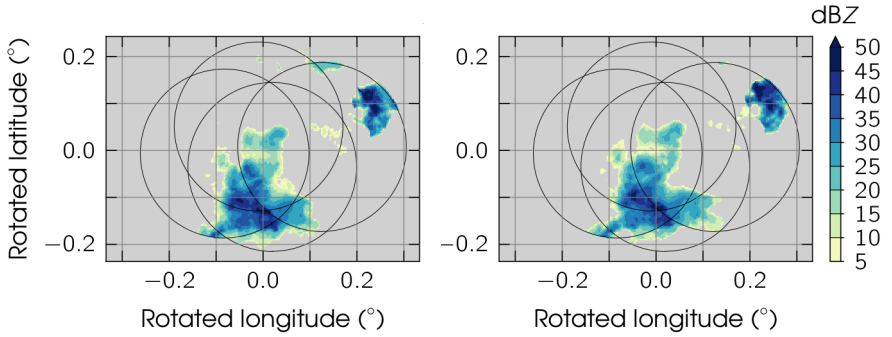

(a) 15:23:00 UTC **(b)** 15:26:00 UTC

Figure 4.1: LAWR composite reflectivity data for 15:23:00 UTC **(a)** and 15:26:00 UTC **(b)** on the 3rd July 2013 used to initialise the ensemble nowcast.

work and to show the method's potential (Chapter 5). For this, a precipitation event monitored by the radar network on the 3rd July 2013 is chosen as a basis for the data assimilation cycle. The event exhibits a cell moving through the network area and is selected because of its non-stratiform structure (Figure 4.1). The cell does not cover the whole network domain and therefore allows for testing the method in areas with and without precipitation. Furthermore, reflectivity values are not uniform within the precipitation cell, which makes forecast and data assimilation more interesting.

The forecast for the data assimilation experiment is an ensemble nowcast initialised with radar composite data (Section 3.2). The nowcasting domain is 297×213 pixels large with a resolution of $250\,\mathrm{m} \times 250\,\mathrm{m}$, as defined by the input radar data. Forecast start is 15:26:00 UTC. The displacement vector field for the forecast is computed between composite radar images at 15:23:00 UTC and 15:26:00 UTC (Figure 4.1). The determined global displacement is three pixels towards the east and four pixels towards the north, i.e. $u = 4.2\,\mathrm{m\,s^{-1}}$ and $v = 5.6\,\mathrm{m\,s^{-1}}$ respectively. The speed of the precipitation cell is thus estimated to $7\,\mathrm{m\,s^{-1}}$. A more detailed view of Figure 4.1 can be found in Figure 3.4 together with the computed displacement vector field. The forecast is performed for 50 ensemble members until 16:00:00 UTC in time steps of two minutes.

Observations considered for assimilation in this experiment are synthetic observations created from single radar measurements. Polar data from X-band radar MOD is used for this purpose because it covers the analysed precipitation cell best. Observations are created on a $5000\,\mathrm{m} \times 5000\,\mathrm{m}$ grid (20×20 grid boxes in the nowcasting domain) within the reach of X-band radar MOD, resulting in 52 observation locations (Figure 4.2). For these, corresponding reflectivity data from the polar X-band radar data are selected by using the nearest neighbour method. The synthetic observations represent any additional measurements. They could be considered as data from a rain gauge network, for example. They could also represent radar data, which

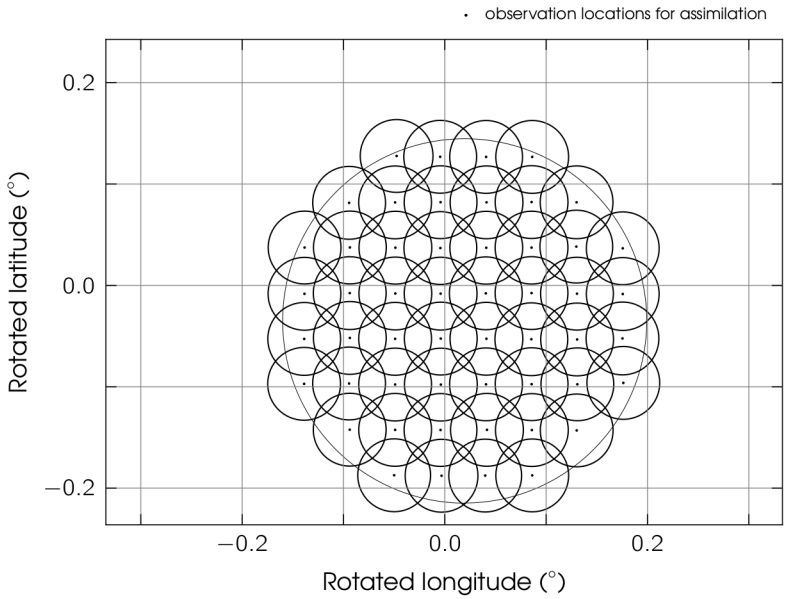

Figure 4.2: Locations of synthetic observations created for assimilation from data of the X-band radar at MOD site on a 5000 m × 5000 m grid. Circles around locations indicate the observation influence radius of 4000 m used in the data assimilation experiment.

is most commonly thinned and/or superobbed on a spaced, regular grid for direct radar data assimilation. This is done to reduce computational costs and representativity disparity and especially avoid correlation of observation errors (e.g. Alpert and Kumar, 2007; Simonin et al., 2014; Bick et al., 2016; Waller et al., 2016). The chosen spacing between observations mentioned above allows for an analysis ensemble that is not completely determined by observed values, i.e. an ensemble that does not collapse. Observation errors are assumed to be uncorrelated and an error variance of 11.32 dB^2 estimated based on network data is used (Section 2.2). Assimilation is performed every four minutes, i.e. every two time steps, from 15:30:00 UTC to 16:00:00 UTC. This assimilation frequency is similar to the temporal resolution of five minutes of the C-band radar data made available operationally by the German Meteorological Service (DWD) and assimilation frequency used in, e.g. Bick et al. (2016). In order to close the data assimilation cycling, a new ensemble nowcast is started after every analysis step. For this new forecast, displacement vector fields are computed deterministically between the last two analysis ensembles, separately for each member (Section 3.2.1).

The use of the LETKF further requires the specification of an observation influence radius, i.e. a radius indicating the area in which an observation has influence on the model ensemble during the analysis step. It is set to 4000 m in this experiment, all relevant data assimilation experiment settings are summarised in Table 4.1. This radius allows for complete coverage of grid points within X-band radar MOD

Table 4.1: Data assimilation experiment settings. More details on the probabilistic nowcasting schemes are given in Section 3.2.

Model specific settings	
Input data	Radar reflectivity composite
Domain size	297×213 grid points
Grid resolution	$250\,\mathrm{m} \times 250\,\mathrm{m}$
Ensemble members	50
Input time step	3 minutes
Forecast time step	2 minutes
Data assimilation settings	
Observation type	Single X-band reflectivity data
Observation grid	$5000\,\mathrm{m} \times 5000\,\mathrm{m}$
Observation frequency	Every 2 minutes
Observation variance (std)	$11.32\,\mathrm{dB}^2$ ($3.36\,\mathrm{dB}$)
Observation influence radius	$4000\,\mathrm{m}$

reach. Therefore, every grid point in this area is affected by the update step during data assimilation (Figure 4.2) which favours a smooth analysis. A sensitivity study confirming the choice of the chosen observation influence radius is presented in Section 4.2.

The multitude of dimensions, i.e. space, time and ensemble members, complicates the evaluation of any data assimilation experiment. As an illustrative starting point, the behaviour of the performed experiment is first shown at one arbitrary grid point of the model domain (0.041 °E, −0.053 °N in rotated coordinates). The chosen grid point corresponds to an observation location within the precipitation cell and allows for the demonstration of the reflectivity ensemble evolution (Figure 4.3). The uncertainty of the ensemble mean is indicated by the ensemble spread, which is defined here as the range given by the ensemble standard deviation. This standard deviation is zero at the beginning of the forecast because all ensemble members are initialised with the same reflectivity field (Section 3.2). Therefore, only displacement vector fields from the ensemble generation differ between ensemble members at 15:26:00 UTC, however reflectivity values are identical. After one time step ensemble members start to diverge and the standard deviation of reflectivity at the considered location increases. At time steps where observations are available, data assimilation is performed, pulling the ensemble mean towards the observation. At the same time ensemble spread decreases due to the information gain. After the assimilation, the ensemble evolves freely again during forecasting steps until the next assimilation is performed. The ensemble mean shows a good agreement with the observations during the considered period. A large deviation between model and observation only appears at the second assimilation time step, where the ensemble mean almost reaches $20\,\mathrm{dB}Z$ whereas the corresponding observation indicates no rain ($5\,\mathrm{dB}Z$, Section 2.1.1). This is caused by slightly too large motion vectors and a resulting

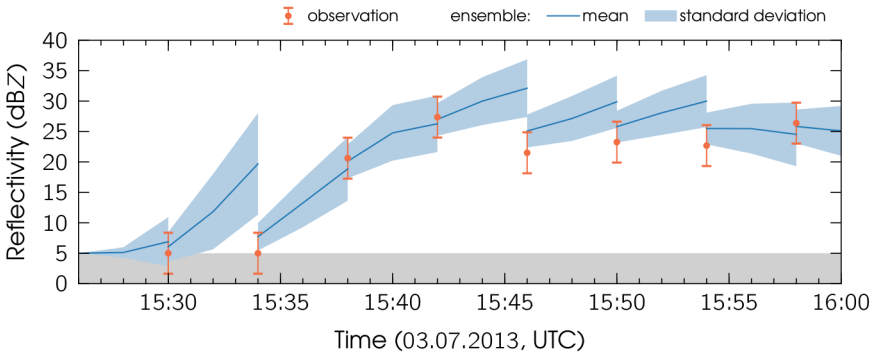

Figure 4.3: Reflectivity ensemble mean evolution (dark blue line) and uncertainty range (light blue envelope, ± one ensemble standard deviation) throughout the data assimilation cycle at observation grid point 0.041 °E, −0.053 °N and observations (orange whiskers, ± observation error standard deviation).

too fast advection of the precipitation field. Precipitation in the forecast reaches the considered model grid point before the precipitation onset in the observations. After that time, when precipitation also appears in the observations, observations and model are in better agreement.

The reduction of ensemble spread caused by the update step of the LETKF is not only present at grid points corresponding to observation locations. Observations impact ensemble values at all grid points within their influence radius (Figure 4.4). Depending on the relation between ensemble mean and observations, the increment caused by the update in the analysis step can be positive or negative. The spatial structure of the increments is determined by the covariance matrix of the background ensemble. It indicates the relation between the ensemble at an observation grid point and the ensemble at the grid point currently considered in the data assimilation analysis. The influence of observations is smooth in space, indicating that the ensemble adequately represents the covariance within observation influence radius. Otherwise, the spatial structure of the increments would show random, speckled patterns. At 15:46:00 UTC and 15:58:00 UTC data assimilation induces a decrease in the ensemble mean at most grid point affected by the observations. This is due to the divergent displacement of the precipitation cell between the different ensemble members, spreading predicted precipitation over a large area of the domain. Forecasted precipitation is then reduced by the assimilation in areas where the actual observations do not record precipitation. As expected from theory, ensemble spread decreases at every grid point affected by the data assimilation (Figure 4.5).

The divergence between ensemble members with advancing forecast is apparent in the temporal evolution of the ensemble mean (Figure 4.6). At the beginning of the forecast interval, members do not differ much and the ensemble mean shows values above 5 dBZ in a delimited and concentrated region. At later time steps reflectivity

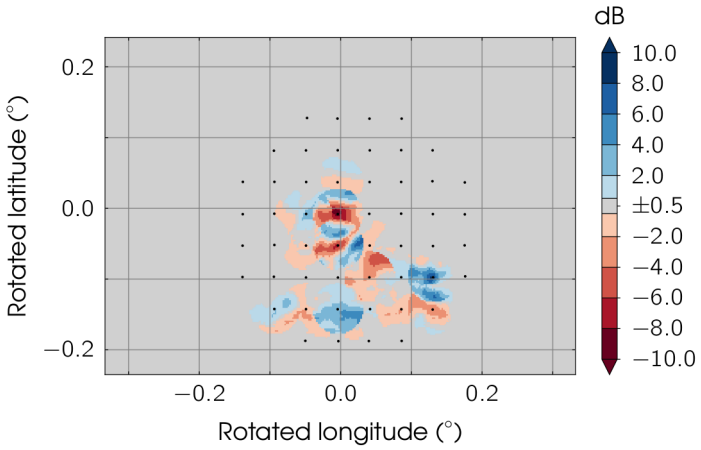

(a) 15:30:00 UTC

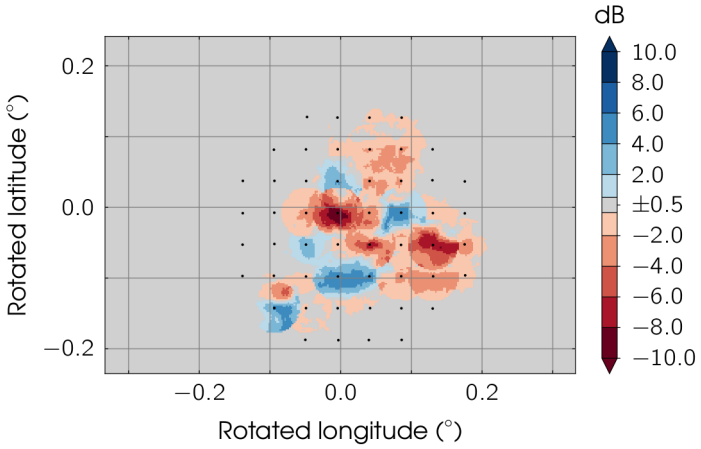

(b) 15:46:00 UTC

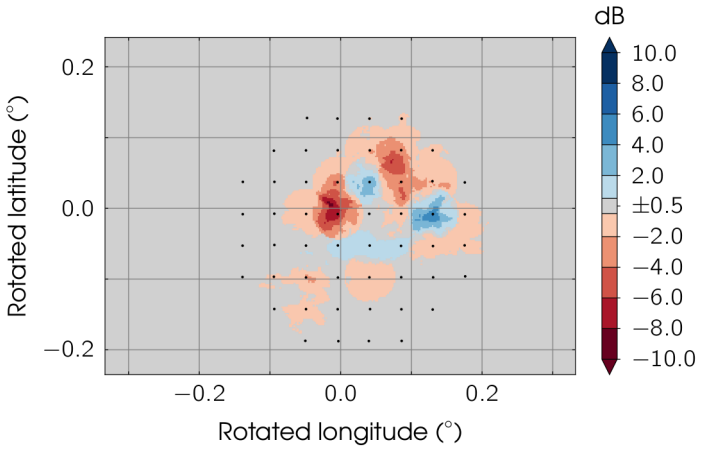

(c) 15:58:00 UTC

Figure 4.4: Data assimilation reflectivity increments (analysis minus background) for the analysis time steps at 15:30:00 UTC **(a)**, 15:46:00 UTC **(b)** and 15:58:00 UTC **(c)**.

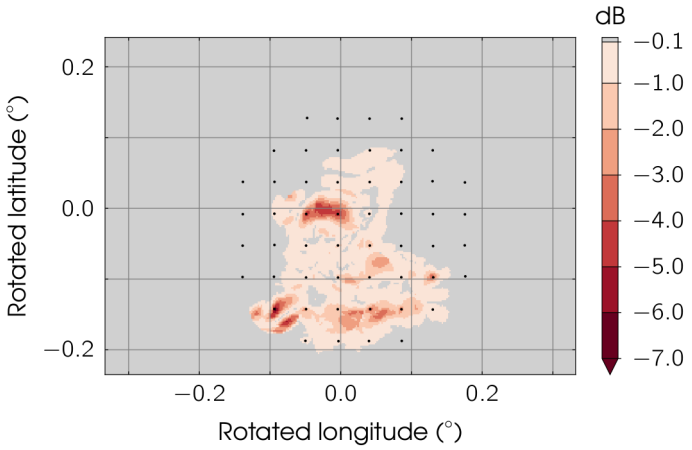

(a) 15:30:00 UTC

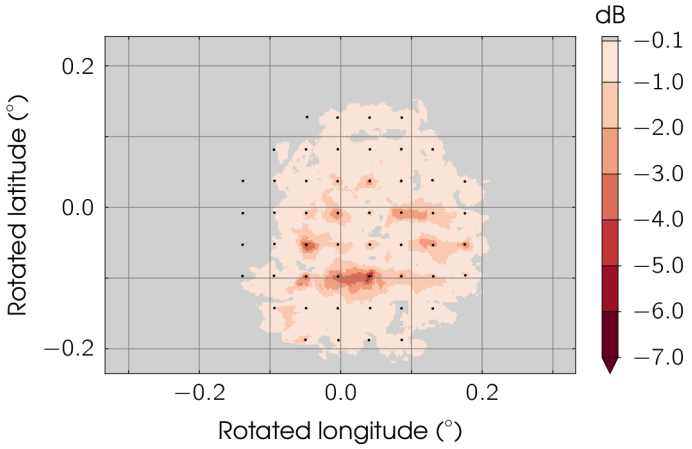

(b) 15:46:00 UTC

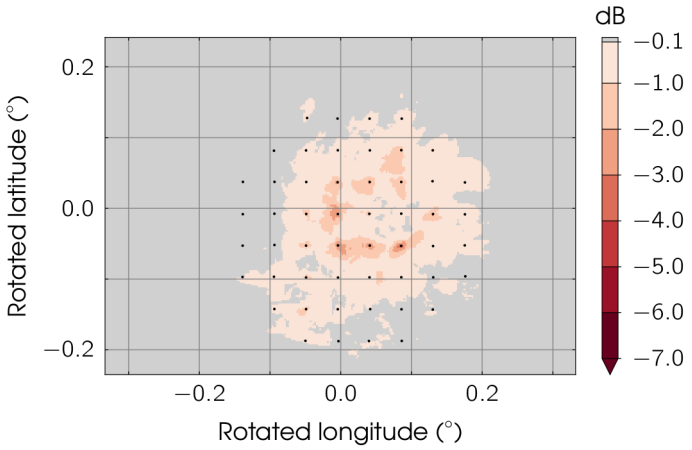

(c) 15:58:00 UTC

Figure 4.5: Reflectivity ensemble spread, i.e. ensemble standard deviation, reduction (analysis minus background) for the analysis time steps at 15:30:00 UTC **(a)**, 15:46:00 UTC **(b)** and 15:58:00 UTC **(c)**.

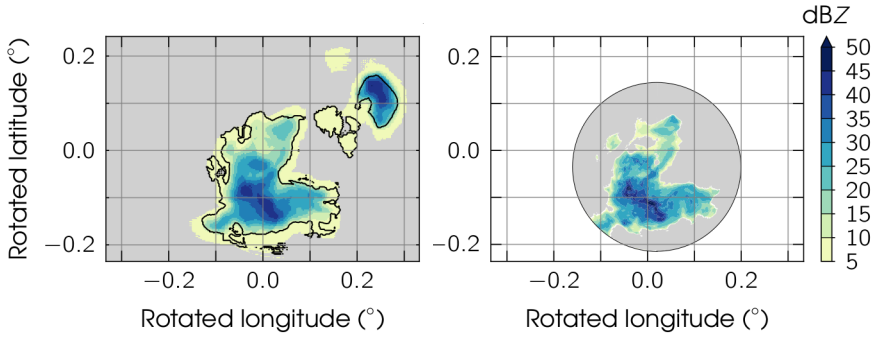

(a) Ensemble mean, 15:30:00 UTC **(b)** MOD radar, 15:30:00 UTC

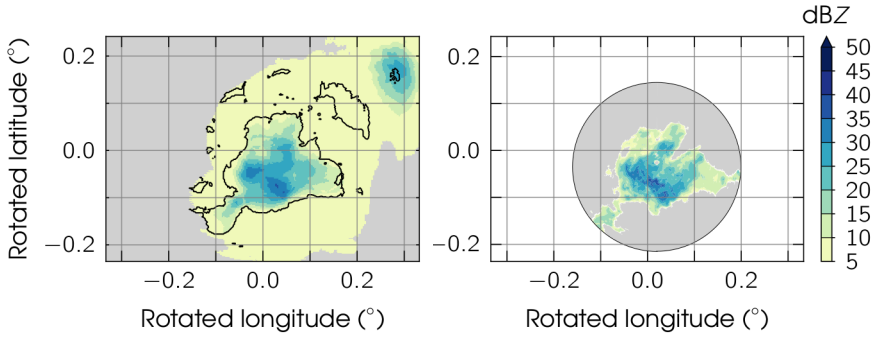

(c) Ensemble mean, 15:46:00 UTC **(d)** MOD radar, 15:46:00 UTC

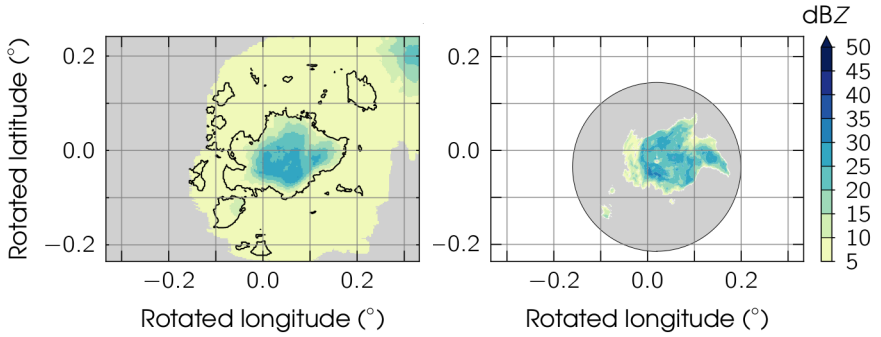

(e) Ensemble mean, 15:58:00 UTC **(f)** MOD radar, 15:58:00 UTC

Figure 4.6: Left side: Forecasted ensemble mean reflectivity (analysis) for 15:30:00 UTC **(a)**, 15:46:00 UTC **(c)** and 15:58:00 UTC **(e)**. The black contour indicates the region with precipitation probability above 80 %. Right side: Corresponding single X-band radar MOD reflectivity measurements (circle is maximum radar range).

values in the ensemble members spread over a larger region due to the different directions and speeds of the displacement vector fields. Therefore, the ensemble mean appears to be blurred and shows a large area with low reflectivity values around a core with higher reflectivity values. The probabilistic information provided by the ensemble nowcast allows for delimiting grid points at which more than 80 % of the ensemble members predict precipitation. This additional information indicates the most probable location of the precipitation cell in the forecast. This location corre-

sponds well with simultaneous radar observations of the X-band radar at MOD site. As mentioned above, X-band radar MOD best captures the studied precipitation cell and is used to compare forecast to reference observations.

Model predicted reflectivity and single X-band radar MOD observations are compared at grid points chosen for verification. Those locations are selected on a 5000 m × 5000 m grid, similar to assimilation locations. The verification grid is shifted by 2500 m in each direction with respect to the assimilation grid in order to select independent observation for assimilation and verification (Figure 4.7). The verification grid consists of 47 grid points within X-band radar MOD range. Reflectivity forecast and observations are compared at verification grid points at each of the eight assimilation time steps, after the update. Thus, the comparison comprises 376 data points in total. At first sight forecast mean corresponds well to observations, except for an accumulation of data points where the forecast predicts precipitation but observations have no precipitation, i.e. 5 dBZ (Figure 4.8). These points describe cases in which no rain is observed by the measurements but the model ensemble predicts some. The model ensemble mean mostly remains below 15 dBZ in these cases. These relatively low reflectivity values indicate that theses discrepancies mostly occur at the edge of the precipitation cell, where the cell predicted by the model mean is not correctly restricted in space.

The overall root mean square error (RMSE) amounts to 4.49 dB and the bias to 1.54 dB. Data points where the forecast predicts precipitation but observations have no precipitation do not affect the bias much. The bias is reduced to 1.04 dB but the RMSE increased to 5.95 dB when removing those data points. This is due to the fact that in almost 10 % of the cases, the ensemble mean matches with observations showing no precipitation, those data points improve scores. For forecast verification these data points are not removed since forecast includes regions without rain. But results from the forecast can be improved slightly by applying the 80 % precipitation probability threshold introduced in Figure 4.6, i.e. setting the ensemble mean for grid points with precipitation probability lower than 80 % to no rain (5 dBZ). Then the bias is 1.14 dB and the RMSE 4.44 dB, showing a slight improvement over using model ensemble mean without integrating probabilistic information.

The bias indicates an overestimation of precipitation by the forecast model. This is probably due to the fact that cell maxima are spread over different locations through the different ensemble members. Therefore, more model grid points are influenced by high reflectivity values than corresponding observations. Depending on the reflectivity value range, 1 dB has a different impact on the forecast error in terms of precipitation. Because of the logarithmic scale, a bias of 1.14 dB in the forecast is equivalent to an overestimation of 30 %. The RMSE of 4.44 dB is approximately 1 dB larger than the estimated accuracy of the original radar data of 3.36 dB (Section 2.2). A bias correction of the data in Figure 4.8 does not effectively

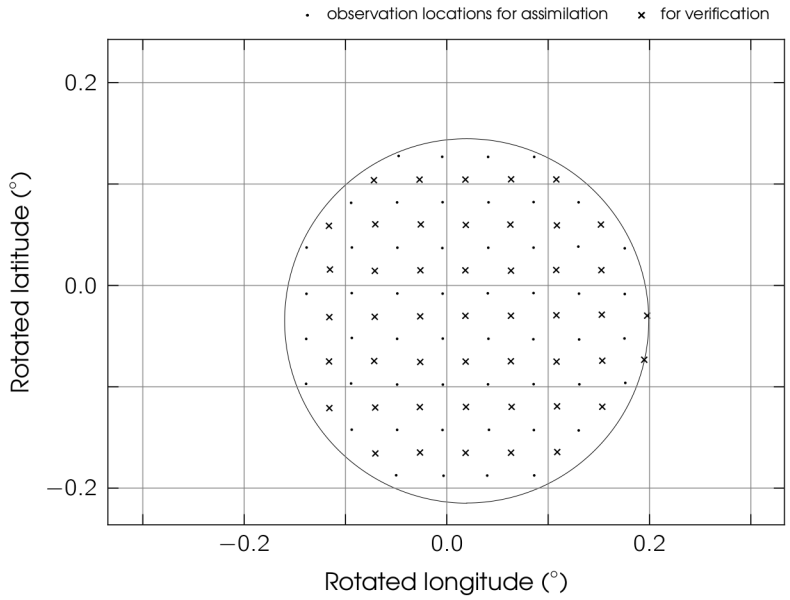

Figure 4.7: Locations of synthetic observations as in Figure 4.2 (dots) and locations for verification on a 5000 m × 5000 m grid shifted by 2500 m north and east (crosses).

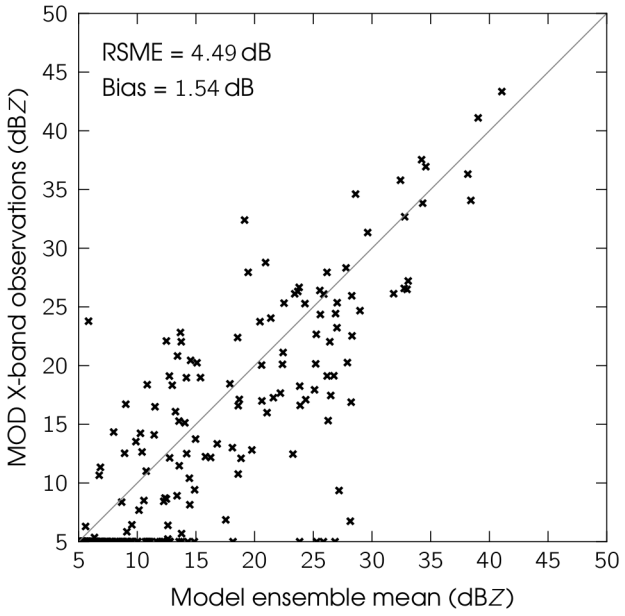

Figure 4.8: Comparison of ensemble mean reflectivity (analysis) and X-band radar MOD reflectivity measurements at the available 47 verification grid points and eight analysis time steps.

reduce the RMSE, which then drops to 4.29 dB. Therefore, the variance of the product provided by the data assimilation framework is slightly larger than the one of the original data but remains in the same range.

Data assimilation within the presented framework performs as required, as demonstrated for example by the typical behaviour of ensemble members in Figure 4.3. The results of the forecast, verified against independent observations, are reasonable, especially since the only information used for the forecast is motion extracted from the comparison of two images. No additional information on the dynamics of the precipitation cell is used. The ensemble forecast allows for a probabilistic assessment of the precipitation nowcast, which enables the narrowing of the region where precipitation is most probable. The wide spread of locations affected by precipitation in the forecast ensemble mean is due to the simple advection approach and the ensemble member generation by perturbing the displacement vector.

4.2 Sensitivity to Observation Influence Radius

The above section confirms the correct functioning of the implemented data assimilation framework. An observation influence radius of 4000 m is used for the localisation in the LETKF, to cover a large number of grid points and obtain a smooth analysis (Figure 4.2). The impact of using different observation influence radii is discussed in the following in a brief sensitivity study. The data assimilation experiment in Section 4.1 is performed again, with observation influence radii of 1000 m, 2000 m, 3000 m, 5000 m, 6000 m and 7000 m. The initialisation of the ensemble members for each experiment is identical, the random noise generation is controlled using a fixed seed value. This analysis supports the above choice of observation influence radius of 4000 m for further studies in Chapter 5.

The main impact of changing the observation influence radius per definition is the changed area impacted by each observation. This effect becomes apparent in the increments obtained at the analysis time step at 15:46:00 UTC for the six different observation influence radii (Figure 4.9). Model grid points outside the observation influence radius remain unchanged by the data assimilation procedure. Therefore, the impact of data assimilation on the forecast decreases with the radius. Changes induced by observations can be smoothed out quickly during the next forecast steps if the impacted region is small. On the other hand, large observation influence radii lead to overlapping information at grid points affected by more then one observation. The LETKF can potentially be subject to undersampling, even if the effect is strongly reduced by the domain localisation (Section 3.1.3). Information from observations can have a negative impact on the analysis because of erroneous background covariance matrices relating the increment at observation location to the change in the ensemble at considered grid point. This effect increases with increasing distance between considered grid point and observation grid point and can have a negative impact on the product.

The experiment results in this section are verified against observations using the

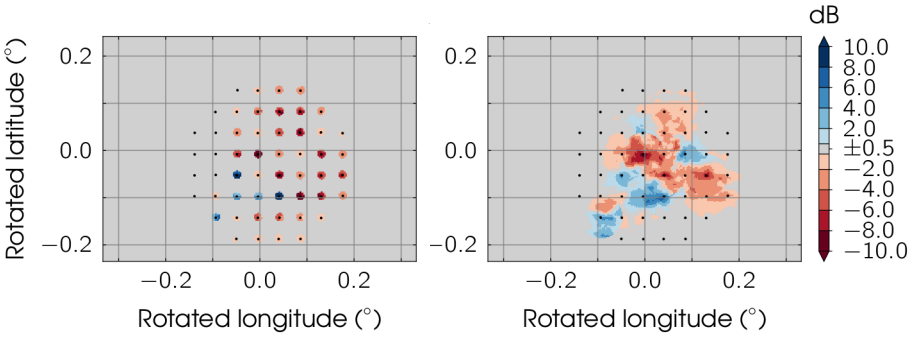

(a) Radius: 1000 m **(b)** Radius: 5000 m

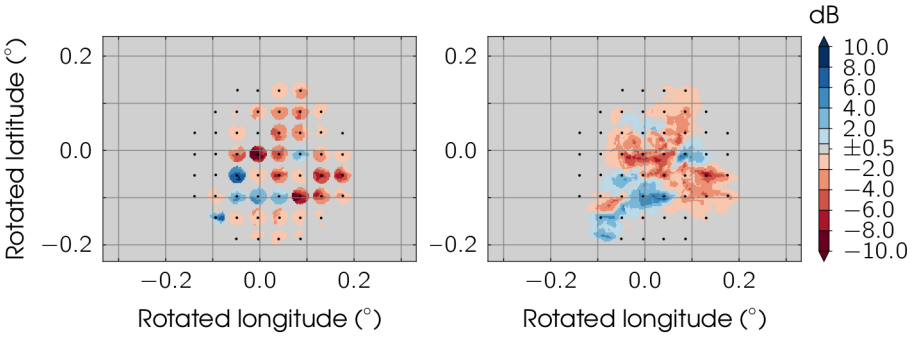

(c) Radius: 2000 m **(d)** Radius: 6000 m

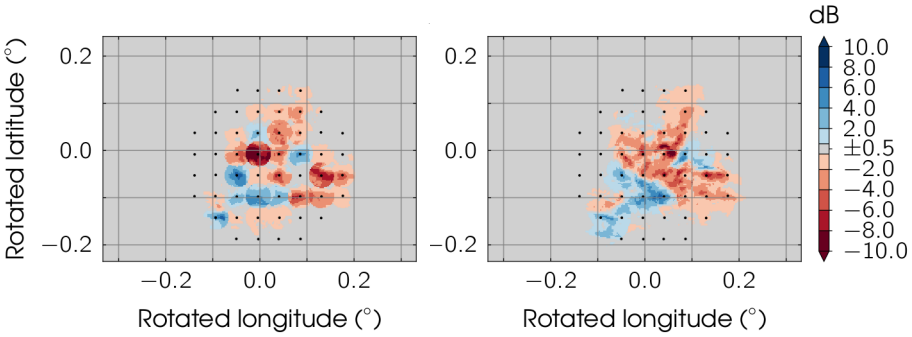

(e) Radius: 3000 m **(f)** Radius: 7000 m

Figure 4.9: Data assimilation reflectivity increments (analysis minus background) for the analysis time step at 15:46:00 UTC for data assimilation experiments with varying observation influence radius: 1000 m, 2000 m, 3000 m, 5000 m, 6000 m and 7000 m. Experiment setup as in Section 4.1. Results with an observation influence radius of 4000 m in Figure 4.4b.

same procedure as in Section 4.1, calculating bias and RMSE (Table 4.2, Figure 4.10). As the observation influence radius increases, bias and RMSE first decrease. The minimum value is reached for 5000 m and 4000 m radius, respectively. This is due to the larger area impacted by observations with larger observation influence radius. Larger observation radii cause a larger area of the predicted reflectivity to be pulled towards the observed reflectivity values. But as the observation influence radius increases further, no further improvement can be found. Bias and

Table 4.2: Bias and RMSE between forecast ensemble mean reflectivity (analysis) and single X-band radar MOD measurements at verification grid points and analysis time steps for data assimilation experiments with varying observation influence radius. The selected observation influence radius is highlighted.

Obs. influence radius	Bias (dB)	RMSE (dB)
1000 m	2.70	5.30
2000 m	2.34	4.79
3000 m	2.01	4.68
4000 m	1.54	4.49
5000 m	1.52	4.58
6000 m	1.56	4.48
7000 m	1.65	4.52

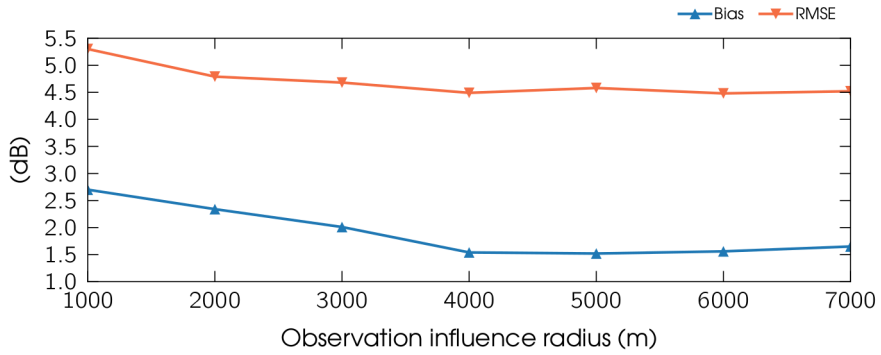

Figure 4.10: Bias and RMSE for different observation influence radii as shown in Table 4.2.

RMSE even show a tendency to increase again. This indicates that overlapping observation information does not add value to the system. They can even deteriorate the forecast, probably because of contradicting effects on the ensemble at considered grid point.

An observation radius of 4000 m guarantees impact of observations on all grid points within X-band radar MOD reach and at the same time causes only slight overlapping of observation information. It seems to be an adequate choice for the presented system based on verification results discussed above. Therefore, the experiment described in Section 4.1 will be further used in the next chapter, with settings gathered in Table 4.1.

5 Areal Uncertainty Estimate for a Combined Precipitation Product

Chapter 4 validates the data assimilation framework (Chapter 3) and confirms the performed data assimilation experiment (Section 4.1) as valid foundation for further analysis. This chapter addresses the analysis and assessment of the variable, areal uncertainty information provided by the implemented method together with the combined precipitation product. The focus is on the spatial and temporal structure of the uncertainty estimate. The new estimate is shown to be more accurate than benchmarks values, which describe the uncertainty with a constant number representative for the precipitation system. The study is based on the data assimilation experiment presented in Section 4.1 and demonstrates the added value of the presented method providing an accurate areal uncertainty estimate for combined precipitation products.

5.1 Spatial Structure of the Uncertainty Estimate

The quantity describing the uncertainty of the combined precipitation product is the ensemble spread. Here, the ensemble spread is defined as the ensemble standard deviation after a performed analysis. During the data assimilation cycle, the ensemble spread depends on the forecast uncertainty, described by the background error covariance matrix, and on the observation uncertainty, described by the observation covariance matrix. The forecast uncertainty results from the errors associated with the extrapolation scheme used for the precipitation forecast (Section 3.2). The main sources of error are a wrong displacement of the precipitation cell and the neglected representation of the internal evolution of the cell. This forecast uncertainty is reduced at grid points influenced by new observations adding information to the system during data assimilation. The background error covariance matrix $\boldsymbol{P^b}$ and the observation error covariance matrix $\boldsymbol{R}$ determine the effect of new information

on the ensemble at affected grid points. The observation error used for assimilation is constant in this study and derived from statistical data analysis (Section 2.2). The uncertainty described by the model ensemble spread continuously evolves within the considered system through the data assimilation cycle. The model ensemble, and thus the ensemble spread containing the uncertainty information, is subject to the forecast and therefore develops a flow dependency. By this means, the presented method allows for a physically consistent propagation of uncertainty in time.

The potential of the presented areal uncertainty estimate for the combined precipitation product is its temporal and spatial variability and its statistical consistency. In order to prove the added value of the method, the uncertainty estimate, i.e. the ensemble spread, is analysed with focus on its correct spatial distribution. Non-zero ensemble spread only exists at grid points where at least one ensemble member shows precipitation values above the no-precipitation threshold of 5 dBZ, defined in Section 2.1.1. This region expands with time as ensemble members diverge because precipitation is advected with different displacement vectors in each member (Figure 5.1). Ensemble spread reaches maximum values at the first analysis time step in the north-east corner of the domain. Ensemble spread maximum values stay nearly constant for the rest of the forecast period, varying between 17.8 dB and 18.9 dB. With increasing forecast lead time, the region of maximum spread moves further north-east with the direction of the precipitation cell displacement (see cell displacement direction in Figure 3.4). These high ensemble spread values throughout the forecasting period are due to the fact that no observations are available for data assimilation in this area. Therefore, the ensemble evolves freely and its spread is not restricted by additional information on the cell.

In other parts of the domain, the position of the precipitation cell is mostly within reach of the X-band radar MOD. Therefore, the ensemble at these grid points benefits from further information through the assimilation of observations from this radar. Within the area covered by observations from the X-band radar MOD, the ensemble spread at the beginning of the forecasting period is largest at the edges of the precipitation cells. In these regions, ensemble members diverge quickly due to their different displacement directions and speeds. Further into the forecast, this pattern changes. The area of grid points with non-zero ensemble spread widens and ensemble spread is smallest at the edges of this area because only few ensemble members predict precipitation at these outer grid points. In the center of the area, the spatial distribution of the ensemble spread evolves in time. As mentioned above, the structure of this ensemble spread is of importance because it represents the structure of the uncertainty of the obtained combined precipitation product.

The spatial structure and temporal evolution of this uncertainty information is the main asset of the method presented in this thesis. Its potential is demonstrated in the following sections.

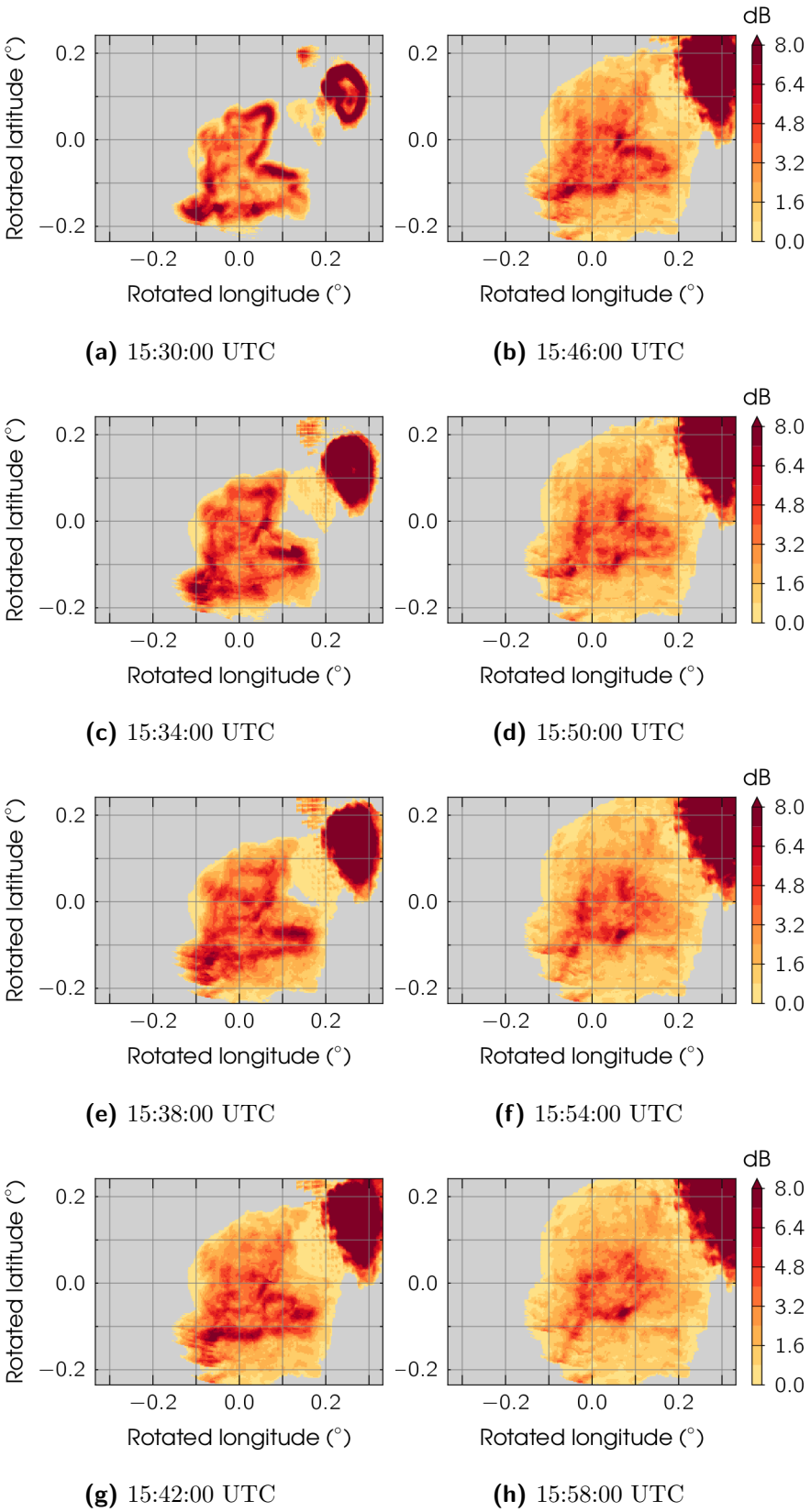

(a) 15:30:00 UTC **(b)** 15:46:00 UTC

(c) 15:34:00 UTC **(d)** 15:50:00 UTC

(e) 15:38:00 UTC **(f)** 15:54:00 UTC

(g) 15:42:00 UTC **(h)** 15:58:00 UTC

Figure 5.1: Spatial distribution of the reflectivity ensemble spread (analysis), i.e. ensemble standard deviation, for all available analysis time steps.

5.2 Uncertainty Verification Scores and Benchmarks

Uncertainty specified for a certain quantity cannot be verified on the basis of single values because it is a statistical concept. Therefore, verification of uncertainty information must be done statistically. To characterise the quality of the areal uncertainty estimate of the combined precipitation product provided here, the statistical relation between forecasted uncertainty, i.e. the ensemble standard deviation, and the actual error, i.e. the deviation between forecasted and observed reflectivity, is analysed. In a so-called spread-skill diagram, the perfect relation between forecast uncertainty and forecast error is a one-to-one relation (Figure 5.2). The uncertainty forecast perfectly describes the uncertainty of the system if, statistically, the actual forecast error equals its forecasted uncertainty. The term ”skill” is counterintuitive and must rather be understood as absolute error. The higher the ”skill” quantity, the larger the error of the forecast.

For all available verification grid points and analysis time steps introduced in Section 4.1, i.e. 376 data points, absolute forecast error and corresponding ensemble spread are compared in a spread-skill diagram (Figure 5.3). Ensemble spread is divided in classes of 0.5 dB, from 0 dB to 8 dB. Statistics of the absolute forecast error within these classes are described by the median and the first and third quartiles. Most data points show ensemble spread and absolute product error below 0.5 dB. This category is dominated by grid points without precipitation, both in the forecast and the observations. There is a clear correlation between ensemble spread and absolute product error, hinting at a good uncertainty representation by the ensemble spread. In the range between 0 dB to 3 dB ensemble spread, the forecast model ensemble is overdispersive because ensemble spread is substantially larger than the median of the absolute product error distributions (median below the one-to-one line). This is due to non-zero model forecast values at grid points outside the observed (true) precipitation cell. Most of the ensemble members correctly predict no precipitation for those grid points, but some have higher reflectivity values because of the different precipitation displacements. The ensemble standard deviation is more strongly impacted by these few high reflectivity values than the ensemble mean. Therefore, the ensemble standard deviation is larger than the deviation between ensemble mean and observation. To diminish this effect data can be filtered using the probabilistic information provided by the ensemble forecast, as described in Section 4.1. By removing data from grid points with a precipitation probability below a threshold of 80 %, a number of affected grid points outside the true cell location can be removed. Using this filter reduces the data sample from 376 to 177 data points but strongly improves the spread-skill relation for ensemble spread below 3 dB (Figure 5.4).

Two scores are defined to quantify the potential of the ensemble spread to correctly represent the uncertainty of the precipitation product. The aim is to prove that

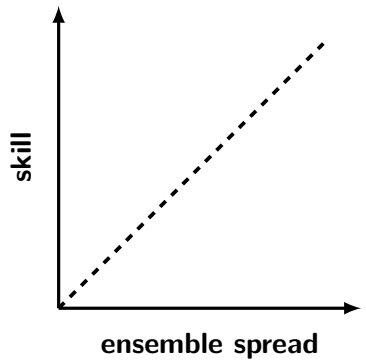

Figure 5.2: Schematic illustration of a perfect statistical spread-skill relation. Here, spread is model ensemble standard deviation and skill is absolute error between model ensemble mean and observations.

the spatial and temporal structure of the uncertainty estimate is not random, but actually provide valuable additional information.

Reliability (*REL*): The first score indicates the amount of data points for which the absolute product error falls within the uncertainty range predicted by the ensemble spread – the percentage of "hits". The ensemble spread is interpreted as the tolerated margin of error. The score represents the reliability of the product uncertainty estimate

$$REL = \frac{100}{N} \sum_{i=1}^{N} [\epsilon_i \leq \sigma_i], \tag{5.1}$$

where ϵ_i and σ_i are the absolute forecast error and the uncertainty estimate for each available verification data point i, respectively. The brackets here are Iverson brackets, which take the value 1 if the enclosed condition applies and 0 otherwise. The higher the value of REL, the better the uncertainty estimate.

Spread-skill deviation (*DEV*): The second score measures the deviation from the perfect spread-skill relation, i.e. from a one-to-one relationship. It is calculated as a root mean square deviation (RMSD) between ensemble spread and absolute model error at the verification grid points:

$$DEV = \sqrt{\frac{1}{N} \sum_{i=1}^{N} (\epsilon_i - \sigma_i)^2}. \tag{5.2}$$

The lower the value of DEV, the better the uncertainty estimate.

The above (5.1) and (5.2) introduce the REL and DEV scores in their generic form. In the following, they will be adapted to the areal uncertainty estimate provided by the method and the used benchmarks.

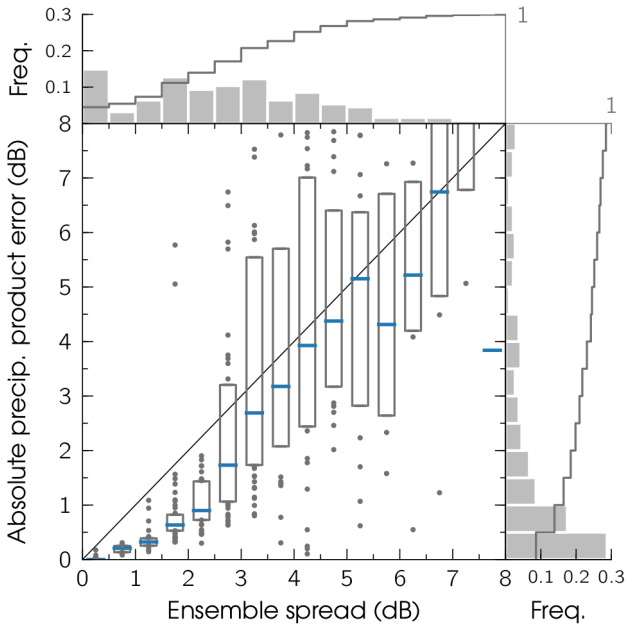

Figure 5.3: Comparison of absolute precipitation product (model ensemble mean) error and ensemble spread (model ensemble standard deviation) at the available 47 verification grid points and eight analysis time steps. Ensemble spread values are divided into bins of 0.5 dB width, boxes indicate the median (blue line) and the first and third quartiles. Data distribution is shown in frequency histograms, the solid grey lines show the cumulative distribution function.

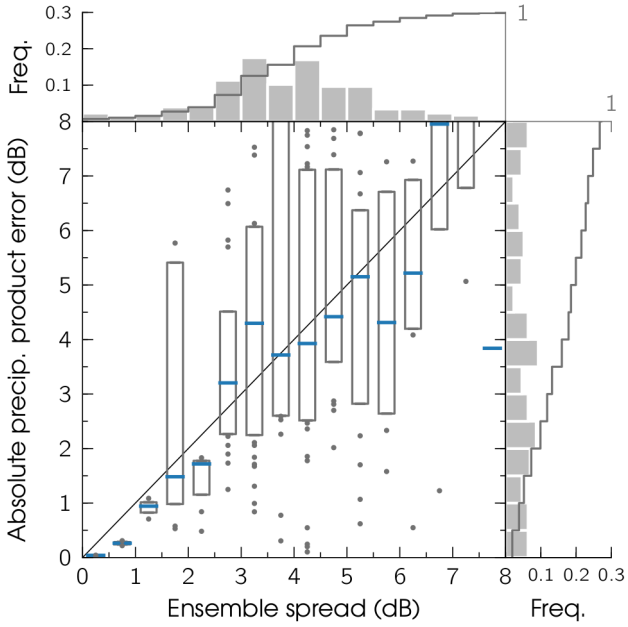

Figure 5.4: Comparison of absolute precipitation product error and ensemble spread as in Figure 5.3, but with data points with a precipitation probability below the threshold of 80 % removed.

To assess the areal uncertainty estimate for the combined precipitation product, above scores are computed with the spatially and temporally variable product uncertainty described by the ensemble spread after the update at all available verification grid points. The reliability REL_{var} is computed with $\sigma_i = \sigma_{\mathrm{var},i}$, where $\sigma_{\mathrm{var},i}$ is the product ensemble spread, and ϵ_i, the corresponding absolute difference between forecast ensemble mean and observations from X-band radar MOD at the same grid points and time. For the spread-skill deviation DEV_{var}, it is taken into account that the relation between ensemble spread and forecast skill is a statistical one. Therefore, median of the model error distributions $\epsilon_{\mathrm{bin},j}$ and corresponding centre of the ensemble spread classes $\sigma_{\mathrm{bin},j}$ (as defined in Figure 5.3) are used. This also reduces the effect of outliers on the RMSD. With this, (5.1) and (5.2) become

$$\begin{aligned} REL_{\mathrm{var}} &= \frac{100}{N}\sum_{i=1}^{N}[\epsilon_i \leq \sigma_{\mathrm{var},i}], \\ DEV_{\mathrm{var}} &= \sqrt{\frac{1}{M}\sum_{j=1}^{M}(\epsilon_{\mathrm{bin},j} - \sigma_{\mathrm{bin},j})^2}. \end{aligned} \tag{5.3}$$

In order to prove the added value of the spatially and temporally variable uncertainty estimate gained by the flow-dependent ensemble spread, the above scores must be compared to a reference. This reference is a benchmark that must be outperformed.

The benchmark used here is a constant uncertainty estimate valid for all grid points at all time steps. Constant uncertainty information is most common for precipitation data from radar or other sources (e.g. Tong and Xue, 2005; Bick et al., 2016). This constant value must be defined. The idea here is to conserve the same total amount of uncertainty among the considered data points with both the variable and the constant uncertainty estimate. By this means, the focus of the analysis is on the ability of the presented method to correctly distribute the available amount of uncertainty information in space and time. Therefore, the chosen reference uncertainty estimate is a mean ensemble spread of the system, $\bar{\sigma}$. The first approach to obtain the mean ensemble spread is to calculate an average over the ensemble standard deviation at verification grid points, including all analysis time steps: $\bar{\sigma}_{\mathrm{sample}} = 2.71\,\mathrm{dB}$. In order to confirm that results do not crucially depend on the value of this mean ensemble spread and that the validation of the method is reliable, a second mean ensemble spread is computed using all grid points of the nowcasting domain: $\bar{\sigma}_{\mathrm{domain}} = 1.63\,\mathrm{dB}$. Due to the fact that a large number of grid points at the edges of the domain have ensemble spread zero because they are outside the area affected by precipitation, $\bar{\sigma}_{\mathrm{domain}}$ is smaller than $\bar{\sigma}_{\mathrm{sample}}$ and is influenced by the size of the precipitating area. A smaller value of $\bar{\sigma}$ implies that the range of uncertainty predicted for the precipitation product is smaller.

The spatially and temporally variable uncertainty estimate of the combined precip-

itation product $\sigma_{\mathrm{var},i}$ is now compared to both $\bar{\sigma}_{\mathrm{sample}}$ and $\bar{\sigma}_{\mathrm{domain}}$ using the *REL* and *DEV* scores. For this purpose, the areal uncertainty is replaced by the constant values, yielding the benchmark values for both scores, *REL* and *DEV*:

$$\begin{aligned} REL_{\mathrm{sample}} &= \frac{100}{N}\sum_{i=1}^{N}[\epsilon_i \leq \bar{\sigma}_{\mathrm{sample}}], \\ DEV_{\mathrm{sample}} &= \sqrt{\frac{1}{M}\sum_{j=1}^{M}(\epsilon_{\mathrm{bin},j} - \bar{\sigma}_{\mathrm{sample}})^2} \end{aligned} \tag{5.4}$$

and

$$\begin{aligned} REL_{\mathrm{domain}} &= \frac{100}{N}\sum_{i=1}^{N}[\epsilon_i \leq \bar{\sigma}_{\mathrm{domain}}], \\ DEV_{\mathrm{domain}} &= \sqrt{\frac{1}{M}\sum_{j=1}^{M}(\epsilon_{\mathrm{bin},j} - \bar{\sigma}_{\mathrm{domain}})^2}. \end{aligned} \tag{5.5}$$

5.3 Assessment of the Precipitation Product Uncertainty Estimate

The potential of the uncertainty estimate provided by the presented method is analysed in comparison to constant uncertainty benchmarks representative for the system (Section 5.2). The aim of the study is to assess the potential of $\sigma_{\mathrm{var},i}$ to better describe the uncertainty of the system and the ability of the data assimilation cycling to better distribute the uncertainty both in time and space. Scores for the reliability of the uncertainty estimate and its deviation from a perfect spread-skill relation, *REL* and *DEV*, introduced in (5.3), (5.5) and (5.4) are computed for $\sigma_{\mathrm{var},i}$ and both benchmarks $\bar{\sigma}_{\mathrm{sample}}$ and $\bar{\sigma}_{\mathrm{domain}}$. Because Figure 5.2 indicates an overdispersive ensemble when using all available verification data points, scores are also computed for data filtered with the probabilistic information gained through the ensemble (Figure 5.4). For verification data points below the 80 % precipitation probability threshold, ensemble mean is set to 5.0 dBZ and ensemble spread to 0.0 dB beforehand. This data set is referred to as filtered data in the following, unchanged data as original.

Both scores show an improvement when using the areal uncertainty estimate provided by the data assimilation cycling method compared to using constant benchmark uncertainty estimates (Table 5.1). This statement is valid using both original data and filtered data. Furthermore, the choice of the constant reference uncertainty only changes the magnitude of the improvement. For original (filtered) data, reliability of the uncertainty estimate REL_{var} improves by 9.58 percentage points (13.56 percentage points) compared to REL_{sample} and by 20.75 percentage points (20.47 percentage points) compared to REL_{domain}. DEV_{var} is reduced by 1.43 dB (2.04 dB) compared to DEL_{sample} and 1.92 dB (2.96 dB) compared to DEL_{domain}.

Table 5.1: Results for *REL* and *DEV* scores for variable uncertainty estimate σ_{var} (highlighted) and both benchmark values σ_{sample} and σ_{domain}.

Scores	Original data	Filtered data
REL_{var} (%)	77.13	76.06
REL_{sample} (%)	67.55	62.50
REL_{domain} (%)	56.38	55.59
DEV_{var} (dB)	1.25	1.19
DEV_{sample} (dB)	2.68	3.23
DEV_{domain} (dB)	3.17	4.15
$DEV(\bar{\sigma}_{\text{optima,REL}})$ (dB)	2.57	2.47

Especially the reliability improvement depends significantly on the chosen constant reference uncertainty. The larger the tolerated margin of error defined by the uncertainty estimate, the higher the probability for the actual precipitation product error to lie within the predicted range. *REL* can take any desired value if σ_i is tuned accordingly. For this reason, $REL_{\text{sample}} > REL_{\text{domain}}$ as expected. Consequently, the improvement of *REL* using the variable uncertainty estimate $\sigma_{\text{var},i}$ becomes less and less apparent for increasing values of constant uncertainty $\bar{\sigma}$ because only the magnitude of the margin of error matters, and not the spatial or temporal distribution. Values of $\bar{\sigma}$ can easily be tested in (5.1) and increased until a theoretical, optimal $\bar{\sigma}_{\text{optimal},REL}$ that yields better *REL* than REL_{var} is found. Using the original data set, $\bar{\sigma}_{\text{optimal},REL} \geq 4.2\,\text{dB}$ yield a higher reliability than REL_{var}. But this improvement of the *REL* score cannot be transferred to *DEV*, as this score takes into account the correct distribution of the uncertainty, i.e. low (high) predicted uncertainty where absolute product error is small (large). Therefore, using the above computed optimal constant uncertainty value yields $DEV(\bar{\sigma}_{\text{optimal},REL}) \geq 2.66\,\text{dB}$, which is always higher than DEV_{var}.

Similarly to the optimisation of *REL* above, *DEV* can be minimised for an optimal constant $\bar{\sigma}_{\text{optimal},DEV}$. The minimisation yields $DEV(\bar{\sigma}_{\text{optimal},DEV} = 3.49\,\text{dB}) = 2.57\,\text{dB}$ for the original data set and $DEV(\bar{\sigma}_{\text{optimal},DEV} = 3.92\,\text{dB}) = 2.47\,\text{dB}$ for the filtered data set. This value of the spread-skill deviation is the smallest value achievable with a constant $\bar{\sigma}$ and is still higher than DEV_{var}. Therefore, even if *REL* can yield better results than REL_{var} with a constant spread value, *DEV* still shows best results with $\sigma_{\text{var},i}$. This supports the statement that the uncertainty distribution in $\sigma_{\text{var},i}$ provide a better representation of the actual precipitation product uncertainty than the one obtained with a constant $\bar{\sigma}$. The variable uncertainty $\sigma_{\text{var},i}$ is able to predict low uncertainty where actual product error is small, and high uncertainty where product error is larger.

As stated above, the reliability of the uncertainty estimate *REL* directly depends on the tolerated margin of error. The larger the tolerated margin of error is, the larger the actual precipitation product error ϵ_i can be. In (5.1), the margin of error is

one standard deviation. The tolerated margin of error can be scaled by introducing the scaling factor α into (5.1) controlling the margin of error as a multiple of the ensemble spread:

$$REL = \frac{100}{N} \sum_{i=1}^{N} [\epsilon_i \leq \alpha \cdot \sigma_i]. \tag{5.6}$$

Above results for REL_{var}, REL_{sample} and REL_{domain} are computed with $\alpha = 1$, as apparent in (5.3), (5.5) and (5.4). Now, the reliability is computed for $0 \leq \alpha \leq 10$ (Figure 5.5). As expected, values for REL_{var}, REL_{sample} and REL_{domain} increase with increasing α, and eventually approach 100 % reliability. All three scores take the same value at $\alpha = 0$ because the number of data points with perfectly predicted reflectivity values ($\epsilon = 0$) still fulfilling the condition in (5.6) is the same for all. Except for $\alpha = 0.25$, REL_{var} always yield better reliability than both benchmark values. This means that for a fixed required reliability, the presented areal uncertainty estimate $\sigma_{\text{var},i}$ allows for a smaller tolerated margin of error for the combined precipitation product. For example, a reliability of $REL = 80\,\%$ is reached with a tolerated margin of error just above one standard deviation for REL_{var}, whereas it must be increased to approximately 1.75 and 2.75 for both benchmarks REL_{sample} and REL_{domain}, respectively.

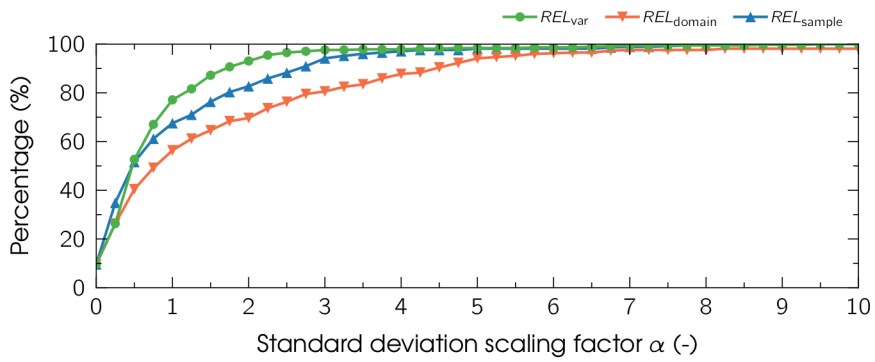

Figure 5.5: Reliability score REL according to (5.6) for spatially and temporally variable uncertainty estimate $\sigma_{\text{var},i}$ and both benchmark values σ_{domain} and σ_{sample}, for different values of α scaling the tolerated margin of error.

6 Summary, Conclusions, and Outlook

This thesis presents a method to estimate spatially and temporally variable uncertainty of an areal precipitation product. The method makes use of data assimilation to merge precipitation measurements from different sources. Data assimilation is performed with an ensemble nowcasting model which provides information about the precipitation displacement over time. An ensemble data assimilation framework was developed and implemented during the course of this thesis. Additionally, an extrapolation-based nowcasting scheme was implemented and coupled to the data assimilation framework, together with X-band radar observations. The implemented framework allows for testing the presented method. The potential of the areal uncertainty estimate provided by the method is demonstrated in a proof of concept study.

The aim of the presented method is to merge measurements from different sources into a combined precipitation product and to provide an associated spatially and temporally variable uncertainty estimate. Requirements for this uncertainty estimate are an accurate representation of the actual error of the product, an adjustment to additional observations merged into the product through data assimilation, and flow dependency. Such detailed uncertainty description is important in order to assess the reliability of the precipitation product. This information is especially important for areal precipitation information as it is needed, for example, to generate precipitation ensembles for probabilistic hydrological modelling, or to specify accurate error covariance when using precipitation observation for data assimilation into numerical weather prediction models. In this study, radar reflectivity is used to described precipitation. Reflectivity can be converted to rain rate using empirical relations that are not part of the analysis.

The developed data assimilation framework is implemented using object-oriented programming to achieve a high level of flexibility (Chapter 3). It is designed for ensemble data assimilation methods and currently works with the Local Ensemble Transform Kalman Filter (LETKF). The framework can easily be coupled to other

models and extended with further observation types. It is used in combination with precipitation nowcasting in this thesis, but is not restricted to this purpose. The implemented nowcasting scheme computes the cross-correlation between subsequent radar composite images and extrapolates the evolution of the precipitation field using the deduced displacement. The nowcast is started from composite data of a network of four X-band radars and a probabilistic forecast is generated using an ensemble technique. The ensemble is generated by stochastic perturbation of the computed precipitation displacement vector.

The implemented framework allows the coupling of the nowcast with additional precipitation information. Observations used for data assimilation in the proof of concept study presented in this thesis are generated on a regular grid from single X-band radar data (Section 2.1.1). The required X-band radar measurement uncertainty is computed statistically by comparison with reference micro rain radars (MRR), using five months of high-resolution data from a radar research network. The standard deviation of the X-band radar measurement error is found to be 3.36 dB (Section 2.2).

A data assimilation experiment is performed to test the presented method with emphasis on its potential to provide an improved spatial and temporal uncertainty estimation. For the experiment, an ensemble precipitation nowcast is performed and additional observations are merged into it continuously using the LETKF, generating a combined precipitation product. The behaviour of the data assimilation cycle results confirms the functioning of the framework. A comparison of the forecast results with observations establishes the experiment as valid foundation for the analysis of the method (Chapter 4).

The uncertainty of the precipitation product is estimated by the ensemble spread of the nowcast after each performed data assimilation step. Two scores are introduced for the assessment of the method. Both are based on the definition of a perfect uncertainty estimate, for which the actual observed error must statistically correspond to the predicted uncertainty. The first score describes the reliability *REL* of the uncertainty estimate. It indicates the percentage of cases in which the actual error of the precipitation product lies within the estimated uncertainty range, which defines a tolerated margin of error. The second score measures the deviation *DEV* of the uncertainty estimate from a perfect spread-skill relation as a root mean square deviation between actual error and uncertainty estimate (Section 5.2).

The scores are computed at verification grid points selected on a regular grid and for all available analysis time steps. The assessment of the potential of the obtained areal uncertainty estimate $\sigma_{\mathrm{var},i}$ requires a benchmark which must be outperformed. The benchmark for this study is defined as the mean spread of the system. By this means, the ability of the method to correctly distribute the available mean uncertainty of the system over time and space can be studied. The mean uncertainty

of the system is computed using only verification grid points ($\bar{\sigma}_{\text{sample}} = 2.71\,\text{dB}$) and all grid points of the domain ($\bar{\sigma}_{\text{domain}} = 1.63\,\text{dB}$).

Both scores demonstrate an improvement of the uncertainty estimate by the presented method. The reliability, *REL*, increases by 9.58 percentage points (from 67.55 % to 77.13 %) when using $\sigma_{\text{var},i}$ instead the constant uncertainty $\bar{\sigma}_{\text{sample}}$ and by 20.75 percentage points (from 56.38 % to 77.13 %) compared to using $\bar{\sigma}_{\text{domain}}$. The spread-skill deviation, *DEV*, is reduced by 1.43 dB (from 2.68 dB to 1.25 dB) when using $\sigma_{\text{var},i}$ compared to using $\bar{\sigma}_{\text{sample}}$ and by 1.92 dB (from 3.17 dB to 1.25 dB) compared to using σ_{domain}. These results show that the presented areal uncertainty estimate allows for a more accurate distribution of the uncertainty of the combined precipitation product (Section 5.3) than a constant uncertainty information. Calculating optimal theoretical values for both scores also prove that no constant uncertainty information can outperform the uncertainty estimate by $\sigma_{\text{var},i}$.

Additionally, an analysis of the influence of the tolerated margin of error on the results of the reliability score *REL* is conducted. This analysis demonstrates that for the same level of reliability, the uncertainty estimate provided by the presented method allows for a smaller tolerated margin of error than the benchmark values. For example, a reliability of 80 % is reached with a margin of error of approximately one standard deviation using $\sigma_{\text{var},i}$ compared to 1.75 and 2.75, approximately, for σ_{sample} and σ_{domain}.

The proof of concept shows the potential of the developed method and establishes the groundwork for further studies and possible applications. The evaluation of both considered scores demonstrates that the provided areal uncertainty estimate outperforms constant benchmark uncertainty values. It enables a more accurate distribution of uncertainty in space and time, increasing the uncertainty estimate for regions where the precipitation product exhibits large errors, and decreasing it where the product has smaller errors. To the best knowledge of the author, this is the first study of this kind, focusing on the assessment of flow-dependent uncertainty for a combined precipitation product using data assimilation. The proof of concept study elaborated in this thesis shows good results and encourages further study.

The next step of study and development of this method should address its applicability in a real network setting. The proof of concept is performed in a rather conceptual environment. The method was analysed based on an individual case study, performing a data assimilation cycle for a 30 minute time period of a precipitation event. Observations used for data assimilation are taken from one source and represent a dense, regularly spaced measurement network. Furthermore, the nowcasting scheme used to perform the forecast and include the flow dependency is kept simple, relying on displacement extrapolation. The analysis performed in this thesis can be extended to more precipitation events or other observation configurations for data assimilation. Especially the case of contradicting observations, e.g.

by implementing biases in the generated synthetic data, could yield valuable information on how the method performs in a real setting. But in order to truly assess the performance of the method in a realistic environment, it would be interesting to exchange some of the framework parts used here with others, closer to operational applications.

A first step could be the improvement of the forecasting system. The forecasting system is important because it incorporates the temporal evolution of the system into the uncertainty estimate and allows for its flow dependency. Furthermore, the nowcasting ensemble and its spread influence the data assimilation results and the resulting uncertainty estimate. The nowcasting scheme used for the proof of concept study in this thesis does not take into account internal variability of the cells caused for example by growth and decay. Furthermore, it relies on the persistence of the displacement direction and velocity and cannot represent rotation movements. These effects are important for time scales up to 30 minutes forecast and more. A more elaborated nowcasting scheme, e.g. including cell tracking or even a merging with numerical weather prediction, is likely to be beneficial to the method.

The data used in this study is from a high-resolution weather radar network. Due to the high spatial and temporal variability of the data, the network offers great options to study the accuracy of the method in further precipitation cases, and, e.g. study its performance in different situation like stratiform or convective ones. The most interesting aspect of the network data with respect to the method is the possibility to further improve the estimation of the measurement errors specific to the data set. In this thesis, X-band radar data is used for assimilation with a constant observation uncertainty. This observation uncertainty is computed by comparison with reference MRRs, as described in Section 2.2, which is already an accurate estimation of the actual measurement error of the X-band radars. Using the multiple available combination of different X-band radars and MRRs within the network, it is possible to substantially refine this description of the measurement error. The computed measurement error can be analysed with respect to different parameters in order to find dependencies that can be used as predictors for the X-band radar measurement error. A preview of such a study is shown in Figure 6.1. The data set presented in Section 2.2 is used to analyse X-band radar measurement error as a function of distance from the radar. There is a notable dependency between X-band radar measurement error and distance from the radar that can be used to further specify the uncertainty of X-band radar observations used for data assimilation.

Furthermore, an improvement towards a more complete X-band radar measurement error covariance matrix could be achieved by analysing time series of the X-band radar measurement errors. This allows for a reduction of the thinning of radar observations for data assimilation, where covariance of errors of the observations have to be either specified or observations thinned to a distance at which errors

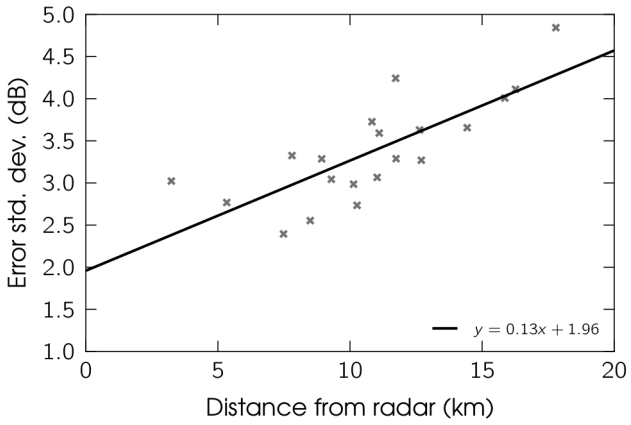

Figure 6.1: X-band radar measurement error standard deviation for different distances from the radar computed from five months high-resolution network data (Section 2.2) and linear regression function.

can be assumed uncorrelated. A study on the structure of the error covariance matrix could also be realised by operationally implementing the presented method in a network environment and analysing the resulting uncertainty estimate over a longer, statistically representative, period of time.

The operational implementation within a large radar network, e.g. the C-band radar network of the German Meteorological Service (DWD) covering Germany, is a possible prospective application of the discussed method. The method would be convenient for the generation of a composite precipitation product statistically merging radar, rain gauge and potentially MRR data under consideration of respective measurement errors. The coupling of data from different sources with a precipitation nowcasting tool through ensemble data assimilation would yield a continuously evolving precipitation product along with a corresponding detailed uncertainty field available for further applications like the generation of precipitation ensemble or the use for data assimilation into numerical weather prediction.

References

Aksoy, A., D. C. Dowell and C. Snyder, A Multicase Comparative Assessment of the Ensemble Kalman Filter for Assimilation of Radar Observations. Part I: Storm-Scale Analyses, *Mon. Weather Rev.*, 137(6):1805–1824, 2009.

Alpert, J. C. and V. K. Kumar, Radial Wind Super-Obs from the WSR-88D Radars in the NCEP Operational Assimilation System, *Mon. Weather Rev.*, 135(3):1090–1109, 2007.

Arulampalam, M. S., S. Maskell, N. Gordon and T. Clapp, A tutorial on particle filters for online nonlinear/non-Gaussian Bayesian tracking, *IEEE Trans. Signal Process.*, 50(2):174–188, 2002.

Atencia, A. and I. Zawadzki, A Comparison of Two Techniques for Generating Nowcasting Ensembles. Part II: Analogs Selection and Comparison of Techniques, *Mon. Weather Rev.*, 143(7):2890–2908, 2015.

Berndt, C., E. Rabiei and U. Haberlandt, Geostatistical merging of rain gauge and radar data for high temporal resolutions and various station density scenarios, *J. Hydrol.*, 508:88 – 101, 2014.

Bianchi, B., P. J. van Leeuwen, R. J. Hogan and A. Berne, A Variational Approach to Retrieve Rain Rate by Combining Information from Rain Gauges, Radars, and Microwave Links, *J. Hydrol.*, 14(6):1897–1909, 2013.

Bick, T., C. Simmer, S. Trömel, K. Wapler, H.-J. Hendricks Franssen, K. Stephan, U. Blahak, C. Schraff, H. Reich, Y. Zeng and R. Potthast, Assimilation of 3D radar reflectivities with an ensemble Kalman filter on the convective scale, *Q. J. R. Meteorol. Soc.*, 142(696):1490–1504, 2016.

Bishop, C. H., B. J. Etherton and S. J. Majumdar, Adaptive Sampling with the Ensemble Transform Kalman filter. Part I: Theoretical Aspects, *Mon. Weather Rev.*, 129(3):420–436, 2001.

Bowler, N. E., C. E. Pierce and A. W. Seed, STEPS: A probabilistic precipitation forecasting scheme which merges an extrapolation nowcast with downscaled NWP, *Q. J. R. Meteorol. Soc.*, 132(620):2127–2155, 2006.

Burgers, G., P. J. van Leeuwen and G. Evensen, Analysis scheme in the ensemble Kalman filter, *Mon. Weather Rev.*, 126(6):1719–1724, 1998.

Chang, W., K.-S. Chung, L. Fillion and S.-J. Baek, Radar Data Assimilation in the Canadian High-Resolution Ensemble Kalman Filter System: Performance and Verification with Real Summer Cases, *Mon. Weather Rev.*, 142(6):2118–2138, 2014.

Chumchean, S., A. Seed and A. Sharma, Correcting of real-time radar rainfall bias using a Kalman filtering approach, *J. Hydrol.*, 317(1):123 – 137, 2006.

Ciach, G. J., W. F. Krajewski and G. Villarini, Product-Error-Driven Uncertainty Model for Probabilistic Quantitative Precipitation Estimation with NEXRAD Data, *Journal of Hydrometeorology*, 8(6):1325–1347, 2007.

Cohn, S. E., An Introduction to Estimation Theory, *J. Meteorol. Soc. Jpn.*, 75(1B):257–288, 1997.

Creutin, J. D., G. Delrieu and T. Lebel, Rain Measurement by Raingage-Radar Combination: A Geostatistical Approach, *J. Atmos. Ocean. Technol.*, 5(1):102–115, 1988.

Dai, Q., D. Han, M. Rico-Ramirez and P. K. Srivastava, Multivariate distributed ensemble generator: A new scheme for ensemble radar precipitation estimation over temperate maritime climate, *J. Hydrol.*, 511:17 – 27, 2014.

Dai, Q., M. A. Rico-Ramirez, D. Han, T. Islam and S. Liguori, Probabilistic radar rainfall nowcasts using empirical and theoretical uncertainty models, *Hydrol. Processes*, 29(1):66–79, 2015.

Dixon, M. and G. Wiener, TITAN - Thunderstorm Identification, Tracking, Analysis, and Nowcasting - A Radar-Based Methodology, *J. Atmos. Ocean. Technol.*, 10(6):785–797, 1993.

Doviak, R. J. and D. S. Zrnić, *Doppler Radar and Weather Observations*, Dover Publications, Inc., 2 edition, 2014.

Dowell, D. C., L. J. Wicker and C. Snyder, Ensemble Kalman Filter Assimilation of Radar Observations of the 8 May 2003 Oklahoma City Supercell: Influences of Reflectivity Observations on Storm-Scale Analyses, *Mon. Weather Rev.*, 139(1):272–294, 2011.

Eckmann, T., *Niederschlags-Nowcasting für ein hochaufgelöstes X-Band Regenradar*, Master's thesis, Universität Hamburg, 2016.

Evensen, G., Sequential Data Assimilation with a Nonlinear Quasi-Geostrophic Model using Monte-Carlo Methods to Forecast Error Statistics, *J. Geophys. Res.: Oceans*, 99(C5):10143–10162, 1994.

Evensen, G., The Ensemble Kalman Filter: theoretical formulation and practical implementation, *Ocean Dyn.*, 53(4):343–367, 2003.

Fielding, M. D., J. C. Chiu, R. J. Hogan and G. Feingold, A novel ensemble method for retrieving properties of warm cloud in 3-D using ground-based scanning radar and zenith radiances, *J. Geophys. Res.: Atmos.*, 119(18):10,912–10,930, 2014.

Germann, U., M. Berenguer, D. Sempere-Torres and M. Zappa, REAL—Ensemble radar precipitation estimation for hydrology in a mountainous region, *Q. J. R. Meteorol. Soc.*, 135(639):445–456, 2009.

Grum, M., S. Kraemer, H.-R. Verworn and A. Redder, Combined use of point rain gauges, radar, microwave link and level measurements in urban hydrological modelling, *Atmos. Res.*, 77(1):313 – 321, 2005.

Haberlandt, U., Geostatistical interpolation of hourly precipitation from rain gauges and radar for a large-scale extreme rainfall event, *J. Hydrol.*, 332(1):144 – 157, 2007.

Hitschfeld, W. and J. Bordan, Errors Inherent in the Radar Measurement of Rainfall at Attenuating Wavelengths, *J. Meteorol.*, 11(1):58–67, 1954.

Houtekamer, P. L. and H. L. Mitchell, Data Assimilation Using an Ensemble Kalman Filter Technique, *Mon. Weather Rev.*, 126(3):796–811, 1998.

Houtekamer, P. L. and H. L. Mitchell, A Sequential Ensemble Kalman Filter for Atmospheric Data Assimilation, *Mon. Weather Rev.*, 129(1):123–137, 2001.

Houtekamer, P.L. and F.Q. Zhang, Review of the Ensemble Kalman Filter for Atmospheric Data Assimilation, *Mon. Weather Rev.*, 144(12):4489–4532, 2016.

Hubbert, J. C., M. Dixon and S. M. Ellis, Weather Radar Ground Clutter. Part II: Real-Time Identification and Filtering, *J. Atmos. Ocean. Technol.*, 26(7):1181–1197, 2009.

Hunt, B. R., E. J. Kostelich and I. Szunyogh, Efficient data assimilation for spatiotemporal chaos: A local ensemble transform Kalman filter, *Phys. D*, 230(1-2):112–126, 2007.

Kalman, R. E., A New Approach to Linear Filtering and Prediction Problems, *J. Basic Eng.*, 82(1):35–45, 1960.

Kalman, R. E. and R. S. Bucy, New Results in Linear Filtering and Prediction Theory, *J. Basic Eng.*, 83(1):95–108, 1961.

Kalnay, E., H. Li, T. Miyoshi, S.-C. Yang and J. Ballabrera-Poy, 4-D-Var or ensemble Kalman filter?, *Tellus A*, 59(5):758–773, 2007.

Kober, K. and A. Tafferner, Tracking and nowcasting of convective cells using remote sensing data from radar and satellite, *Meteorol. Z.*, 18(1):75–84, 2009.

Krajewski, W. F., Cokriging radar-rainfall and rain gage data, *J. Geophys. Res.: Atmos.*, 92(D8):9571–9580, 1987.

Krajewski, W. F. and G. J. Ciach, Towards Probabilistic Quantitative Precipitation WSR-88D Algorithms: Data Analysis and Development of Ensemble Generator Model: Phase 4, Technical report, NOAA, 2006.

Lengfeld, K., M. Clemens, H. Münster and F. Ament, Performance of high-resolution X-band weather radar networks - the PATTERN example, *Atmos. Meas. Tech.*, 7(12):4151–4166, 2014.

Lewis, J. P., Fast Template Matching, in *Vision Interface 1995: Proc.*, pp. 120–123, Canadian Image Processing and Pattern Recognition Society, 1995.

Li, L., Schmid W. and Joss J., Nowcasting of Motion and Growth of Precipitation with Radar over a Complex Orography, *J. Appl. Meteorol.*, 34(6):1286–1300, 1995.

Livings, D. M., S. L. Dance and N. K. Nichols, Unbiased ensemble square root filters, *Phys. D*, 237(8):1021–1028, 2008.

Lorenc, A. C., Analysis methods for numerical weather prediction, *Q. J. R. Meteorol. Soc.*, 112(474):1177–1194, 1986.

Mass, C., Nowcasting: The Promise of New Technologies of Communication, Modeling, and Observation, *Bull. Am. Meteorol. Soc.*, 93(6):797–809, 2012.

Mercier, F., L. Barthès and C. Mallet, Estimation of Finescale Rainfall Fields Using Broadcast TV Satellite Links and a 4DVAR Assimilation Method, *J. Atmos. Ocean. Technol.*, 32(10):1709–1728, 2015.

METEK GmbH, *MRR Physical Basics*, 2009.

Ott, E., B. R. Hunt, I. Szunyogh, A. V. Zimin, E. J. Kostelich, M. Corazza, E. Kalnay, D. J. Patil and J. A. Yorke, A local ensemble Kalman filter for atmospheric data assimilation, *Tellus A*, 56(5):415–428, 2004.

Park, T., T. Lee, S. Ahn and D. Lee, Error influence of radar rainfall estimate on rainfall-runoff simulation, *Stoch. Environ. Res. Risk Ass.*, 30(1):283–292, 2016.

Pierce, C. E., P. J. Hardaker, C. G. Collier and C. M. Haggett, Gandolf: a system for generating automated nowcasts of convective precipitation, *Meteorol. Appl.*, 7(4):341–360, 2000.

Probert-Jones, J. R., The radar equation in meteorology, *Q. J. R. Meteorol. Soc.*, 88(378):485–495, 1962.

Pulkkinen, S., J. Koistinen, T. Kuitunen and A.-M. Harri, Probabilistic radar-gauge merging by multivariate spatiotemporal techniques, *J. Hydrol.*, 542:662 – 678, 2016.

Raghavan, S., *Radar Meteorology*, volume 26 of *Atmospheric and Oceanographic Sciences Library*, Springer Netherlands, 2003.

Rico-Ramirez, M. A., S. Liguori and Schellart A. N. A., Quantifying radar-rainfall uncertainties in urban drainage flow modelling, *J. Hydrol.*, 528:17 – 28, 2015.

Rinehart, R. E., *Radar for Meteorologists*, Rinehart Publications, 2010.

Rinehart, R. E. and E. T. Garvey, Three-dimensional storm motion detection by conventional weather radar, *Nature*, 273:287–289, 1978.

Rubel, F. and M. Hantel, Correction of daily rain gauge measurements in the Baltic Sea drainage basin, *Nord. Hydrol.*, 30(3):191–208, 1999.

Seed, A. W., A Dynamic and Spatial Scaling Approach to Advection Forecasting, *J. Appl. Meteorol.*, 42(3):381–388, 2003.

Sideris, I. V., M. Gabella, R. Erdin and U. Germann, Real-time radar–rain-gauge merging using spatio-temporal co-kriging with external drift in the alpine terrain of Switzerland, *Q. J. R. Meteorol. Soc.*, 140(680):1097–1111, 2014.

Simonin, D., S. P. Ballard and Z. Li, Doppler radar radial wind assimilation using an hourly cycling 3D-Var with a 1.5 km resolution version of the Met Office Unified Model for nowcasting, *Q. J. R. Meteorol. Soc.*, 140(684):2298–2314, 2014.

Sirangelo, B., P. Versace and D. L. De Luca, Rainfall nowcasting by at site stochastic model P.R.A.I.S.E., *Hydrol. Earth Syst. Sci.*, 11(4):1341–1351, 2007.

Smith, J. A. and W. F. Krajewski, Estimation of the Mean Field Bias of Radar Rainfall Estimates, *Journal of Applied Meteorology*, 30(4):397–412, 1991.

Talagrand, O., Assimilation of Observations, an Introduction, *J. Meteorol. Soc. Jpn.*, 75(1B):191–209, 1997.

Tippett, M. K., J. L. Anderson, C. H. Bishop, T. M. Hamill and J. S. Whitaker, Ensemble Square Root Filters, *Mon. Weather Rev.*, 131(7):1485–1490, 2003.

Tong, M. and M. Xue, Ensemble Kalman Filter Assimilation of Doppler Radar Data with a Compressible Nonhydrostatic Model: OSS Experiments, *Mon. Weather Rev.*, 133(7):1789–1807, 2005.

Tuttle, J. D. and G. B. Foote, Determination of the Boundary-Layer Air-Flow from a Single Doppler Radar, *J. Atmos. Ocean. Technol.*, 7(2):218–232, 1990.

van Horne, M. P., *Short-Term Precipitation Nowcasting for Composite Radar Rain Fields*, Master's thesis, MIT, 2003.

van Leeuwen, P. J. and G. Evensen, Data Assimilation and Inverse Methods in Terms of a Probabilistic Formulation, *Mon. Weather Rev.*, 124(12):2898–2913, 1996.

Vetra-Carvalho, S., P. J. van Leeuwen, L. Nerger, A. Barth, M. U. Altaf, P. Brasseur, Kirchgessner P. and Beckers J.-M., State-of-the-art stochastic data assimilation methods for high-dimensional non-Gaussian problems, *Tellus A*, submitted, 2017.

Villarini, G. and W. F. Krajewski, Empirically based modelling of radar-rainfall uncertainties for a C-band radar at different time-scales, *Q. J. R. Meteorol. Soc.*, 135(643):1424–1438, 2009.

Waller, J. A., S. L. Dance and N. K. Nichols, On diagnosing observation error statistics with local ensemble data assimilation, *Q. J. R. Meteorol. Soc.*, 2017.

Waller, J. A., D. Simonin, S. L. Dance, N. K. Nichols and S. P. Ballard, Diagnosing Observation Error Correlations for Doppler Radar Radial Winds in the Met Office UKV Model Using Observation-Minus-Background and Observation-Minus-Analysis Statistics, *Mon. Weather Rev.*, 144(10):3533–3551, 2016.

Wolfson, M. M., B. E. Forman, R. G. Hallowell and M. P. Moore, The Growth and Decay Storm Tracker, in *79th AMS Annual Meeting Proceedings*, Am. Meteorol. Soc., Dallas, TX, 2000.

Zinevich, A., H. Messer and P. Alpert, Frontal Rainfall Observation by a Commercial Microwave Communication Network, *J. Appl. Meteorol.*, 48(7):1317–1334, 2009.

Acknowledgements

I deeply thank my supervisors Prof. Dr. Felix Ament and Dr. Marco Clemens for making this thesis possible. I am grateful for the idea that initiated this work, the support I could count on during the whole process and the confidence placed in me. I also thank Prof. Dr. Martin Claußen for chairing my advisory panel and accompanying my progress.

I would also like to acknowledge both Prof. Dr. Roland Potthast and Dr. Sarah Dance for providing helpful advice and encouragement.

Many thanks goes to Dr. Gernot Geppert for the collaboration on the Python ensemble data assimilation framework we developed in hours of rumination, planning and programming. `pyenda` became an essential tool to my research.

Many thanks to all members of the Atmospheric Measurements and Process Modeling group (current and former) for the pleasant working ambience. Special gratitude goes to Heike and Katharina for countless coffee and tea breaks, good time on conferences and advice in all smaller and larger matters that I encountered on my professional path so far.

Olga and I formed a long-distance graduation self-help group that became vital to me, especially in the last months of this undertaking. Danke für die schöni Zit, die mir kah händ.

Special thanks to everyone who spent coffee and lunch breaks with me and supplied me with food, coffee, and good times on evenings and weekends (especially Heike, Frank, Laura, Sebastian, Titus, Gernot). Thank you for reminding me of what is truly important.

Ein großer Dank geht an meine Familie für den Halt und die Gewissheit, dass immer jemand da ist. Unendlich dankbar bin ich meiner Maman, ohne Dich wäre ich nicht wo ich bin. Und Dir, Gernot, kann ich eigentlich nicht genug danken, für endlose moralische Unterstützung und Ermutigung.

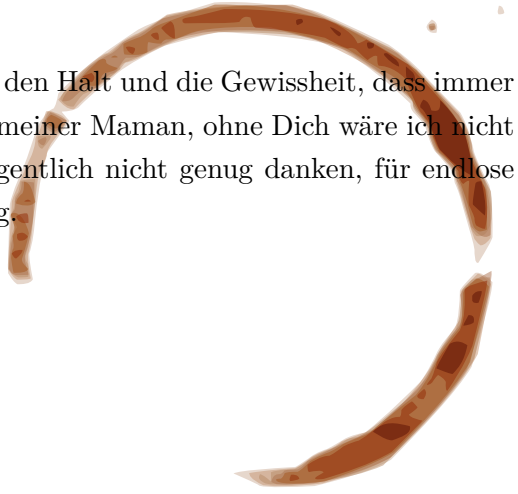

Eidesstattliche Versicherung

Hiermit erkläre ich an Eides statt, dass ich die vorliegende Dissertationsschrift selbst verfasst und keine anderen als die angegebenen Quellen und Hilfsmittel benutzt habe.

Hamburg, den

Claire Merker